Interaction of tungsten films with glassy carbon

by

Innocent Audu Joseph

Submitted in partial fulfilment of the requirements for the degree of

Doctor of Philosophy (PhD) in Physics

In the Faculty of Natural and Agricultural Sciences

University of Pretoria

January, 2020

Supervisor: Prof. JB Malherbe

Co-supervisors: Dr. EG Njoroge

Prof. TT Hlatshwayo

DECLARATION

I, **Innocent Audu Joseph**,

Registration number: **16401027**

declare that the thesis, which I hereby submit for the degree of Doctor of Philosophy in Physics at the University of Pretoria, is a product of my research work and that it has not been submitted in part or in full for a degree at this or any other university, and that all sources used have been acknowledged by means of references.

Signature:.....

Dated: January 2020

ABSTRACT

Interaction of tungsten films with glassy carbon

by

Innocent Audu Joseph

Submitted in partial fulfilment of the requirements for the degree of Doctor of Philosophy (PhD) in Physics in the Faculty of Natural and Agricultural Sciences, University of Pretoria, Hatfield.

Supervisor: Prof. JB Malherbe

Co-supervisors: Dr. EG Njoroge

Prof. Prof. TT Hlatshwayo

The demand for dry casks for extended storage of radioactive nuclear waste is driven by dearth of permanent repositories. Most of the dry cask storage system currently in use are made up of stainless steel which could become vulnerable to corrosion over a period of time. The service lifetime of these steel-based canisters can be improved by electrolytic treatment of its outer

surface with layers of glassy carbon and tungsten. This will ensure sufficient protection against extended long term corrosion and chemical attacks. In this study, the focus has been on the solid state interaction between the W films and glassy carbon substrates. W films were sputtered on the glassy carbon substrates to form diffusion couples. The stability of the diffusion couples under the heat treatment, the interface interaction and carbide phases formed have been studied. To gain more insight on the interface mixing regions due to annealing, quantitative measurements of the solid state reactions between the deposited W films and glassy carbon substrates were carried out. The as-deposited samples were sequentially annealed isothermally under vacuum at temperatures ranging from 400 to 1000 °C in steps of 100 °C. The microstructural changes due to thermal annealing were monitored by Rutherford backscattering spectrometry (RBS) and grazing incidence X-ray diffraction (GIXRD). RUMP software was used to simulate the RBS spectra. The thickness of W thin film deposited, atomic composition of deposited layer and the intermixed layer growth were deduced from the RUMP simulation results. The RBS and GIXRD analysis showed that carbide formation was first observed at an annealing temperature of 900 °C. The kinetics of the solid-state interaction was found to be diffusion controlled at the interface between W and C. The activation energy for the diffusion of C in W was estimated as 2.23 eV. The XRD results showed that the average crystallite size of the glassy carbon was estimated as 2.57 nm, while that of the as-deposited W film was 9.77 nm. This value for W film increased with annealing temperature up to 18.05 nm at 1000 °C. The first carbide phase observed was W_2C in the sample annealed at 900 °C, while WC was the dominant carbide phase at

1000 °C. The surface morphology of the deposited W films was characterized by scanning electron microscopy (SEM). The SEM micro-graphs showed that the as-deposited films were smooth and homogeneous. SEM images of the annealed sample showed complete absence of delamination even at 1000 °C. This showed that the W films were firmly adhered to the glassy carbon substrate, indicating that appropriate sputtering parameters were used.

Furthermore, the microstructural changes of GC under the influence of heat treatments and highly charged ion (HCI) irradiation were monitored by XRD and Raman techniques. Raman results for the heat treated glassy carbon samples showed that the graphitic domains experienced a growth in size upon annealing. On the other hand, under the influence of HCI irradiation, Raman results showed that glassy carbon experienced microstructural disorder. The crystallite size of the glassy carbon irradiated with fluence of 1.0×10^{11} ions/cm^2 at kinetic energy of 60 keV was estimated as 1.61 nm. This value decreased to 1.54 nm in the sample bombarded with the highest kinetic energy 460 keV with intermediate fluence of 5.0×10^{11} ions/cm^2. The atomic force microscopy (AFM) analysis of these irradiated samples showed that the induced surface roughness increased with both fluence and kinetic energy of the HCI.

In conclusion, the XRD study of the microstructure of glassy carbon by method of intensity calculation showed that it is composed of both amorphous and crystalline carbon materials. The evaluated percentage amorphous and crystalline contents are 25% and 75%, respectively.

ACKNOWLEDGMENTS

- I would like to express my profound appreciation to my supervisors, Prof. JB Malherbe, Dr. EG Njoroge and Prof. TT Hlatshwayo, for their guidance and support during the course of this study. A big thanks to Prof. JB Malherbe for taken time out of his busy schedules to read in-between every line, dotting the i's and crossing the t's. He is truly a quintessential professor and a mentor!

- I would like to thank Tshepo Ntshoane for his assistance with the XRD measurements.

- I also thank the University of Pretoria for the financial support through the Postgraduate research bursary.

- I appreciate the financial support of the National Research Foundation South Africa, through the SA-JINR postgraduate research travel grant.

- The Nigerian government and my home institution are hereby acknowledged for the supports.

- I am indebted to Dr Morgan Madhuku of iThemba Laboratory for

Accelerator-Based Sciences (iThemba LABS), Johannesburg, South Africa, for his help with RBS technique and valuable inputs.

- Prof CC Theron is specially recognized and appreciated for all his valuable inputs, advice and the teaching positions in the Physics Department.
- I am most grateful and remain indebted to Dr. EG Njoroge for the teaching positions in the Faculty of Engineering.
- I acknowledge and thank all the students and staff in the physics department.
- Finally, I recognize and appreciate the support and patience of my dear wife Becky, my lovely daughters Grace and Victoria, my one and only son Godwins (Eje!), my parents and brothers. You are my pillars of strength.
- To God alone be all the glory.

TABLE OF CONTENTS

LIST OF TABLES

LIST OF FIGURES

NOMENCLATURE

AFM atomic force microscopy

BCC body centred cubic

BSE backscattered secondary electrons

C carbon

DBTT ductile-to-brittle transition temperature

DC direct current

EHF effective heat of formation

ERD elastic recoil detection

ESIS electron string ion sources

FCC face centered cubic

FWHM full width at half maximum

GC glassy carbon

GIXRD grazing incidence X-ray diffraction

HCI highly charged ion

HCP hexagonal close packed

HLW high level waste

HOPG highly oriented pyrolytic graphite

IAEA International atomic energy agency

IEA International energy agency

ILW intermediate level waste

ITER International thermonuclear experimental reactor

JINR Joint institute for nuclear research

K.E. kinetic energy

LED light emitting diode

LLW low level waste

LTIS long-term interim storage

MCA multi-channel analyzer

NPP nuclear power plant

PIXE particle induced X-ray emission

PVD physical vapour deposition

RBS Rutherford backscattering spectrometry

RT room temperature

RUMP Rutherford universal manipulation program

SCC stress corrosion cracking

SE secondary electrons

SEM scanning electron microscopy

SNF spent nuclear fuel

SSD solid state detector

W tungsten

W_2C ditungsten carbide

WC tungsten monocarbide

XRD X-ray diffraction

XRR X-ray reflectivity

CHAPTER

ONE

GENERAL INTRODUCTION

Currently, fossil fuels, nuclear power and renewable energy are the main stay of the world energy consumption. There is a continuous growth in global energy demand which is driven by increasing prosperity and improvement in standard of living, especially in fast-growing emerging economies. Economic prosperity thus appear to have a direct link with energy consumption. If this be the case, it means energy demand will continue to rise with human population growth. International Energy Agency (IEA) reported in 2015, that the world total energy consumption stood at 158715 TWh [1]. The breakdown of this figure showed that nuclear energy had a share of 5%, renewable sources 10% while the other 85% were shared almost in equal proportion between oil, coal and natural gas.

The first generation nuclear power plants (NPP) were constructed in the 1950s and 1960s [2]. Ever since, the nuclear power had witnessed steady

growth, especially during the 1970s and 1980s. Unfortunately, the growth of nuclear energy was thwarted by the accidents that occurred at Three Mile Island in 1979 and Chernobyl in 1986. There was a revival in the nuclear energy in 2000s until the unfortunate Fukushima incidence in 2011. Notwithstanding all these setbacks, nuclear power is being increasingly recognized, as a technology that if in normal operation, is nonthreatening to the environment. This form of energy is considered as clean energy with almost zero carbon emission.

Nuclear energy is seen by many governments around the world, as an important part of the energy mix. The development of nuclear energy is concentrated in the hands of few group of countries, especially in the Asia continent. China, Korea, India and Russia account for over 60% of nuclear reactors that the IAEA recorded as under construction as at December 2015 [2]. Globally, electricity accounted for about 18% of the total final energy consumption in 2016 [3]. Demand for electricity continues to grow, especially in emerging economy and developing countries. Current nuclear reactors are being designed in such a way that safety and efficiency are the key factors [2]. As at 2016, there were at least 45 modular reactors under development and four reactors under construction [2]. Improvements in the reactor flexibility, safety and efficiency are the target of these new designs. Achieving a breakthrough in this respect will encourage more countries to embrace nuclear technology for electricity generation.

1.1 Nuclear energy

In all currently operating nuclear energy facilities, energy generation is made possible by nuclear fission. The spontaneous splitting of heavy nuclei into lighter ones is termed nuclear fission [4]. When a slow neutron is absorbed by the nucleus of fissile materials, they split into smaller nuclei. This process is accompanied by released of excess energy. Most notable fissile materials are isotopes of uranium and plutonium. When bombarded with neutrons, they under undergo fission which in turn produce neutrons, giving rise to chain reactions.

Fission chain reactions can be controlled and sustained in the nuclear reactors. Nuclear power plants are thermal plants. The heat produced in fission reaction turns water to steam, which is used to spin turbines to generate electric power. The amounts of energy released in these nuclear reactions are enormous. This high energy density involved is one of the technical advantages of this energy type, since it means that much lower volumes of fuel are needed compared fossil fuel. Actual chemical burning is absent in the fission process, hence there is no emission CO or CO_2 gas associated with it. Solid high level nuclear waste generated are confined within the physical fuel itself.

According to International Atomic Energy Agency (IAEA) [5], as at December 2017, the world had 448 operable grid-electric nuclear fission power reactors with total net electrical capacity of 391.72 GW while 59 others are

under construction with an expected net electrical capacity of 60.46 GW.

Since the beginning of 1970s, nuclear energy has been making contribution to the world energy data. Figure 1.1 presents the growth trend of this energy since its inception. The general trend shows an increment in the output from 1971 through 2015, except for a slight decrease observe between 2007 and 2012. This was due to a change in the German nuclear policy and the unfortunate Fukushima accident in March 2011. If all things being equal, a steady uninterrupted growth is projected into the future.

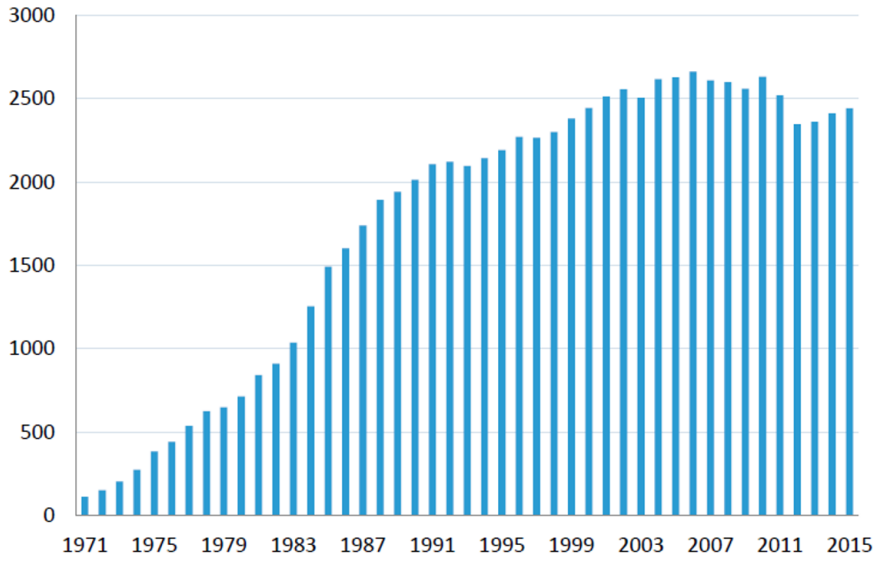

Figure 1.1: The World nuclear electricity production (TWh). Adapted from [2]

In comparison, the contribution of nuclear energy to the world energy data is significant compared to other sources [6]. Figure 1.2 indicates the contribution of all energy sources to the world energy data as at 1973 and 2016. It can be seen that despite the setbacks confronting this form of energy as a result of

isolated incidences of nuclear accidents and concerns over the safe containment of nuclear waste, this energy resource still finds its relevance over the period under review. Its percentage contribution was as little as 1.3% as at 1973 but managed to contribute 9.8% of energy after 43 years! Despite all the challenges, its growth rate is still comparable to all other sources of energy. Although, coal and oil dominate the chart, but one obvious fact is that they

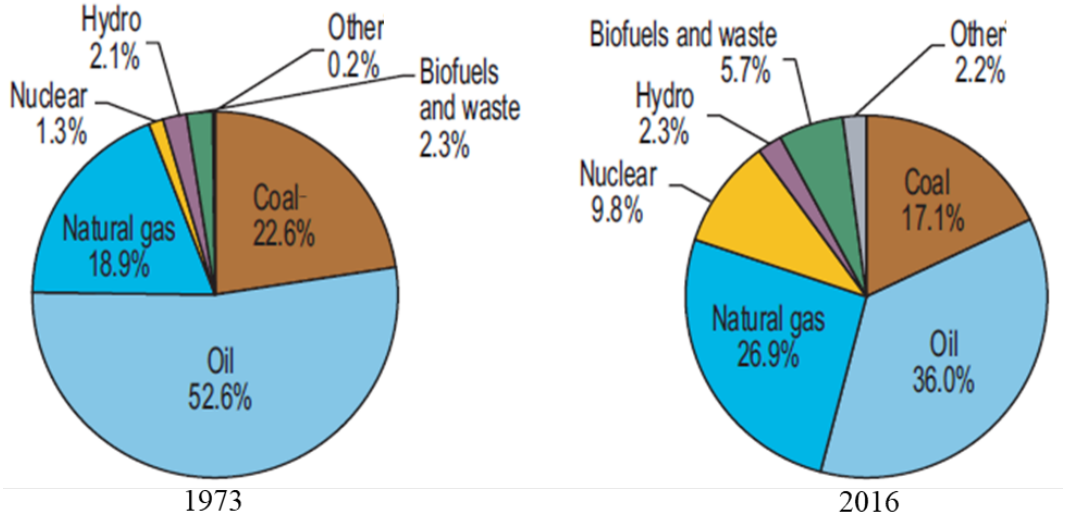

Figure 1.2: The 1973 and 2016 fuel shares of total primary energy sources. Adapted from [2]

all decrease in percentage contribution over the years. Such trend is expected of non-renewable sources of energy over time, because once depleted, they are non replenishing. It is envisaged that with continuous improvement in nuclear technology, this form of energy will in the future, compete favourably with other clean energy sources.

Currently, activities involving the storage and disposal of nuclear waste are still major issues calling for serious concern. This is adds to the drawbacks

of nuclear technology. Radioactive nuclear waste management and storage form an important topic in nuclear technology. The sections that follow are devoted to radioactive nuclear waste, its classification and various methods adopted for its containment.

1.2 Radioactive waste

Just like any other energy technology, nuclear facilities create some environmental impacts. Compared to other sources of energy, the environmental footprint of nuclear energy is small in quantity. This is one of major selling points of this type of energy resource. But in terms of harmful impact associates with various sources of waste, nuclear waste can be very dangerously harmful to both man and the environment.

Nuclear waste is generated in entirely in the fuel cycle, right from raw fuel mining through reactor operation to nuclear waste storage, transportation and disposal. Most harmful nuclear waste emanates from reactor operation. As the nuclear fuel undergoes fission reaction, it produces a number of radioactive specie within the fuel rods [7], and eventually, the fuel becomes exhausted. At this point, the spent nuclear fuel rods are removed from the reactor. The spent nuclear fuel and other leftovers of the fission process are known to be highly radioactive.

Radioactive waste are nuclear materials with radionuclides at activity levels above the threshold set by a regulatory body [8]. Radioactive waste is

generated from the application of nuclear materials for electricity generation, clinical diagnosis and treatment of disease, and other industrial purposes. Nuclear waste decreases in its radioactivity level with time, through a process called radioactive decay. Radioactivity is the spontaneous disintegration of unstable nuclei, accompanied usually by emission of radiation. Radioactive waste are classified primarily based on their half-lives and the risks levels.

1.3 Radioactive waste classification

1.3.1 Low level waste (LLW)

Radioactive waste classified as low-level are items that have become contaminated with radioactive materials. Commonly contaminated items are materials such as the protective shoe covers and clothing, mops, filters, reactor water treatment residues, equipment and tools, medical tubes, injection needles, syringes. The risk of exposure to radiation in the low-level waste varies widely according to the types and concentration of radioactive material in the waste.

Some low level waste from medical research, for example, are not particularly hazardous unless inhaled or consumed. A human can stand near such waste without shielding. On the other hand, processing water at a reactor site can be risky. Generally, low-level waste are characterized by short half-lives [9]. Disposal of this class of waste in a supervised near-surface vaults whilst decay process takes place is effective.

1.3.2 Intermediate level waste (ILW)

These are waste that contains both short lived ($\leq$ 30 years) and long lived (>30 years) [9] radionuclides and careful handling to prevent radiation exposures is necessary. Typically, ILW are by-products obtained from processing of the naturally occurring ores of nuclear materials [10]. Uranium, thorium, radium, polonium and radon are the common tailings which contain radioactive nuclei. Long-term isolation is usually required because ILW contain long-lived radionuclides.

1.3.3 High level waste (HLW)

High level waste are the highly radioactive materials. HLW are the by-products of nuclear power generation. They are mainly the spent nuclear fuel (SNF), which are no longer efficient in sustaining fission reactions. About one-fourth of the total fuel load is spent and is removed from the reactor every 12 to 18 months [10] and replaced with fresh fuel.

SNF is highly radioactive and very harmful. Due to the high level of radiation emission, standing near an unshielded SNF could be fatal. Ten years after removal of SNF from a reactor, the radiation dose at a distance of 1 m away from a typical spent fuel assembly can exceed 20,000 Sv per hour [10]. A dose of 5,000 Sv is high enough to cause immediate incapacitation and death within one week [10]. SNFs contain both short and long-lived radionuclides. For example, iodine-131 has a half-life just 8-days, and hence, their radioactivity

decreases rapidly. However, most of the radioactive elements in SNFs have long half-lives. plutonium-239 for example, has a half-life of 24,000 years while plutonium-240 has a half-life of 6,800 years. SNFs must be isolated and controlled for period a exceeding thousands of years because they contain long-lived radioactive nuclei.

1.4 Nuclear waste storage and disposal

Operation of nuclear energy creates hazardous radioactive waste and spent fuels. The safe storage of such waste is a major concern for many countries that produce nuclear power [11]. The task of radioactive nuclear waste management is a multi-disciplinary activity which encompass the entire fuel cycle, beginning from mining of fissionable minerals (e.g uranium ore), to final disposal of spent nuclear fuel. Nuclear waste management is highly required in diverse activities such as conversion of material to different forms of energy, for example electricity and heat, or the generation of radioactive sources for medical and biological applications, and irradiation sources for diagnostics, therapy and sterilization. Nuclear waste needs to be contained and disposed of in a manner that guarantee its safe isolation from contact with man and the biota, for a period of time sufficiently long enough to have it decayed to a level considered to be radiologically safe. There are several methods available, depending on policies adopted in the different countries to contain nuclear waste; it can range from direct disposal into deep geological repositories,

transmutation through single or multiple recycling of spent fuel in closed fuel cycles [9]. Final geological disposal will always be required; different fuel cycle options are aimed at the overall reduction of amount of nuclear waste to be isolated from the biosphere. Waste management activities have to follow strict licensing procedures, all of which require predictive modelling of the performance of the system to ensure compliance with current regulation.

1.5 Dry storage of nuclear waste

Dry cask is a device for dry storage of spent fuel that has been cooled in the spent fuel pool (wet storage) for at least one year [12]. Candidate materials for canisters are generally metals and their alloys such as copper, iron, stainless steels, titanium alloys and nickel-based alloys [13]. Additional candidate materials are certain ceramic materials. Stainless steel canisters are the most popular ones in use. This is probably because stainless steels have good mechanical properties and are also corrosion resistant. They are relatively available strong materials [14].

A typical steel canisters are steel cylinders that are either welded or bolted closed. The steel cylinder provides a leak-tight confinement of the nuclear waste. Each cylinder is surrounded by additional steel, concrete, or other material to provide radiation shielding to workers and members of the public. Some of the cask designs can be used for both storage and transportation.

There are many types of dry casks bearing different manufacture brands.

A typical cask type is the CASTOR V/21 cask produced by GNS Gesellschaft fur Nuklear-Service mbH, Germany. The cask consists of a thick-walled iron casting Figure 1.3. The overall length is 488.6 cm and the side wall thickness (without fins) is 37.9 cm [15]. The cross-sectional diameter of the cask body, which weighs approximately 92,300 kg, is 240 cm. The cask cavity has a diameter of 152.7 cm and a length of 415.4 cm. It holds a fuel basket and is designed to accommodate 21 fuel assemblies. The loaded weight of the cask is about 106,000 kg. The cask cavity has a diameter of 152.7 cm and a length

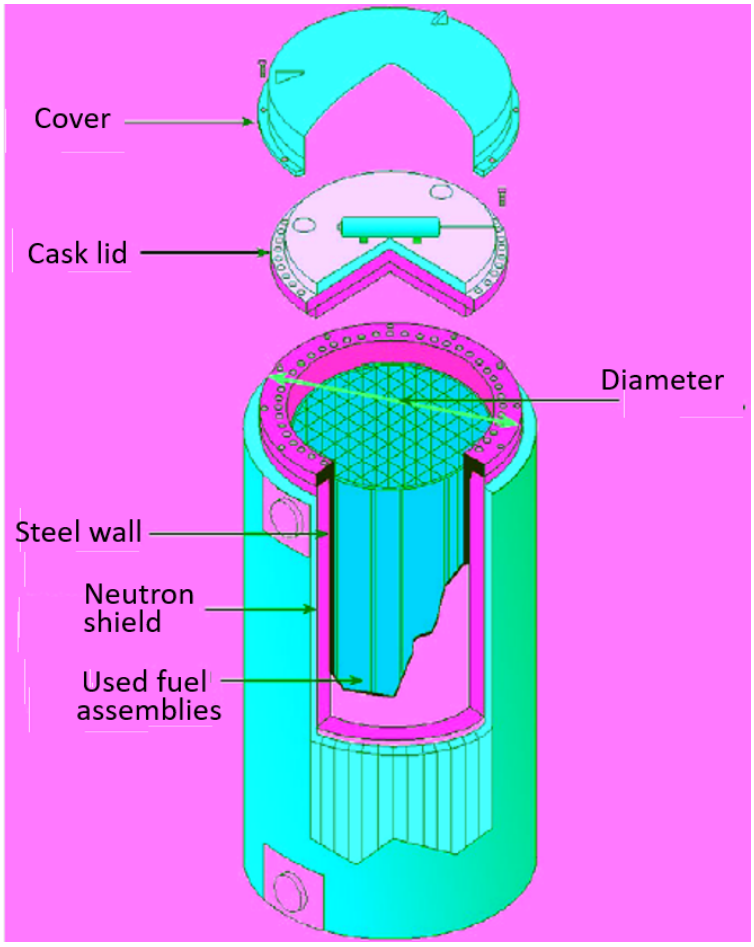

Figure 1.3: A typical dry cask configuration. Adapted from [12]

of 415.4 cm. It holds a fuel basket and is designed to accommodate 21 fuel assemblies. The loaded weight of the cask is about 106,000 kg.

Gamma and neutron radiation is shielded by the cast iron wall of the cask body. The cask is sealed, to maintain a helium atmosphere, with a multiple-cover system consisting of a primary lid and a secondary lid. The use of an inert gas (helium) is to ensure long-term maintenance of fuel clad integrity. It also serves as medium for internal heat-distribution. The primary lid is made up of stainless steel. The overall thickness is 29 cm. It is fastened to the body with 44 bolts. The primary lid has two penetrations, used for flushing and venting of the cask cavity as well as the performance of the leak test. The flushing and venting connections are sealed with separate lids. The secondary lid is also made of stainless steel with thickness of 9 cm. It is bolted to the body. A combination of multiple elastomer and metal seals for each lid provide leak tightness.The maximum surface temperature of a dry casks at loading ranged about 150 - 220 °C [15], [16] and this value decreases with storage time. In canisters made of stainless steels, a potential concern is the susceptibility of these alloys to chloride induced stress corrosion cracking (SCC). In addition to the general and localized corrosion, environmentally assisted cracking and hydrogen-related defect, microbes could also impact the corrosion behavior of the stainless canisters [17]. Although, the stainless steels have good mechanical properties and are corrosion resistant, but catastrophic failures are possible through stress-corrosion cracking or intergranular corrosion.

The other materials being used for fabricating canisters for dry nuclear waste storage, also have their own pros and cons. The shortcomings are issues for concerns especially in terms of extended long term waste storage. Below are the brief descriptions of some of the advantages and disadvantages of these materials.

Copper is known to exhibit very good environmental durability [18]. It has thermodynamic stability in anoxic environments characteristic of underground repositories [14]. However, copper is found to be poor in brine as well as in radiation environment [19]. Iron provides good predictability since much is known about its properties. It is less prone to catastrophic failures, but however, not very corrosion resistant [14]. Titanium alloys are mechanically strong and possess good corrosion resistance. However, they can experience brittle failure with the uptake of hydrogen [14]. Most Nickel-based alloys are similar to titanium in that they are very corrosion resistant. They are easier to weld than titanium, but could be more expensive. Ceramic materials such as silicon carbide, have excellent corrosion resistance and are very much abundant [14], but the problem of mechanical strength is common with these materials.

1.6 Research justification/motivation

Proper management of nuclear waste, especially the SNF and HLW is fundamental to the safety of fuel cycle. When the SNF is removed from the reactor

after irradiation, it is initially stored under water in the nuclear power plant (NPP) pools for about 5 years [20], to allow the radioactivity level and heat to subside. The spent fuel pools are not designed to store the entire SNF produced over the lifetime of operation of the NPP, but are normally transferred to dry casks for further storage periods. Originally, interim dry storage for SNF and HLW were established on the basis of limited periods of 50-60 years [21], after which transfer to permanent repositories can be made. But to date, no permanent repository for SNF or HLW is in operation. This prompted the need to plan for long-term interim storage (LTIS) and today, much longer interim storage periods are being considered. Due to the general delay in the permanent repository site selection in most countries, the temporary storage solutions that were originally envisaged to last for a few decades are faced with the need for an extension of their service life beyond their intended service lifespan, in excess of one hundred years [20], [22]. The demand for LTIS poses a number of scientific challenges including right material selection for dry casks production. It was noted that LTIS is not a deliberate decision in most cases, but the result of a need stemming from unexpected factors such as delays and repository siting difficulties.

Most of the dry storage canisters are made of austenitic stainless steel of different grades [23]. These dry storage systems are normally located in environments near coastal areas for safety purposes. Since the canisters are made of stainless steels, a potential concern is the susceptibility of these alloys to chloride induced stress corrosion cracking (SCC). In addition to

the general and localized corrosion, environmentally assisted cracking and hydrogen-related defect, microbes could also impact the corrosion behavior of the canisters [17]. In the LTIS arrangement, steel-based canisters would become even more vulnerable to effects of SSC and other kind of corrosion. Therefore, there is a need to enhance the service lifetime of these canisters by electrolytic treatment of the outer surface with materials known for their good corrosion resistance. In addition, the ability to withstand chemical attacks and offer of radiation shields are a plus for such materials. This is where glassy carbon and tungsten come in, since they possess such qualities. Covering the outer surface of the steel-based canister with layers of glassy carbon and tungsten will ensure sufficient protection against extended long term corrosion and chemical attacks.

1.7 Research objectives

Glassy carbon is a synthetic form of carbon formed by pyrolysis of organic resins at elevated temperatures [24], [25]. This form of carbon exhibits a combination of glassy and ceramic properties with those of graphitic materials. It has high thermal stability and does not transform into graphite even at high temperatures up to 3000 °C [26]. Glassy carbon possesses physical, chemical and mechanical properties which make it very promising for technological applications [27]. These properties include moderate hardness, resistance to corrosion and wear, high chemical inertness [28], impermeability to gases and

liquids [29]. Other properties are high temperature stability, high thermal conductivity, good resistance to thermal shock and low coefficient of thermal expansion [30]. These properties make glassy carbon potentially useful for many industrial applications, such as vacuum evaporation sources, radiation containment and zone-refinement crucibles.

Tungsten is a heavy metallic element, a member of the third series of transition metals. Tungsten has the highest melting point of all metals, and at temperatures over 1650 °C has the highest tensile strength [31]. It has good chemical, physical and mechanical properties; such as high thermal conductivity, irradiation resistance, exceptional corrosion and abrasion resistance. W also exhibits a low sputter rate and good thermal conductivity [32]. Due to these properties of W, it can serve two main applications in the nuclear waste storage system. First, being an element with high atomic number with massive nucleus, it can act as a shield component due to its ability to block gamma rays which low atomic number elements such as carbon cannot contain. Secondly, it is expected to provide structural enhancement due to its high mechanical strength and corrosion resistant. It is used as important components for X-ray and radiation shielding [33]. Typical examples of such shields are containers for radioactive materials and liquids, shielding construction parts in tomographic scanners, radiation therapy instruments, and containers and shielding for oil prospecting using radioactive sources [33].

The properties of glassy carbon enumerated above have drawn the attention of many researchers to study its performance improvement by ion implantation coupled with annealing. Notable studies on ion species implanted in glassy carbon include Co [34], Cd [35], In [27] and Cs [36]. The results of these studies showed that the diffusion patterns of the implanted fission products are not into the bulk of the glassy carbon, but rather towards the surface damaged by ion implantation. These observations suggested that glassy carbon has promising stability in radiation environment.

Literature search showed that no study on phase formation as well as diffusion between tungsten and glassy carbon has been investigated. Since these two materials are being propose to serve as protective layers for steel-based canisters against corrosion and chemical attacks, it is pertinent to investigate how W and glassy carbon interact under heat treatment. This will help to model these materials behavior under the influence of decay heat of radioactive nuclear waste. The knowledge from this study is important for developing a new technology that will mitigate the challenge of nuclear waste management. The properties of these two materials highlighted above, could be explored in nuclear technology, especially in the dry cask component for extended radiation containment.

The goal of this thesis is to investigate the suitability of glassy carbon and tungsten as protective layers for canisters towards long-term storage of radioactive waste. The focus is specifically on diffusion between glassy carbon

and tungsten, at various annealing temperatures. This involves the study of the temperature at which the glassy carbon and W thin films start to react and identify the products of such reaction. Kinetics data of these materials interactions are important and provide information on the mechanism and extent of interactions at a particular temperature range. With the knowledge of these kinetic data, it is possible to predict the temperature at which degradation can start in the diffusion couple.

In addition, since glassy carbon has been recognized as a structural material, it is microstructural response to heat treatment and highly charged ion (HCI) irradiation are vital knowledge for modelling its potential behaviour in radiation environment, specifically in nuclear waste storage where decay heat and radiation are produced. The paracrystalline nature of glassy carbon which currently forms an important research topics, that has not been exhaustively studied will also be looked into terms of its amorphous fraction, using the X-ray diffraction (XRD) technique.

1.8 Synopsis of the thesis chapters

This thesis is made up of 8 chapters. The synopsis of the chapters are given as follows: Chapter 1 provides general information on the world energy resources and share of contribution made by nuclear energy, nuclear waste and its classification, nuclear waste management and storage, research motivation and scope of investigation. In Chapter 2, discussions on carbon and its

polymorphs were given. These covered it's structure, ability to form hybrid bonds, products of its polymorphism including diamond, graphite, fullerenes and glassy carbon were discussed. The structure, properties and applications of glassy carbon which forms the subject of this study were also discussed. Chapter 3 presents discussions on the structure and properties of tungsten as well as its applications. Diffusion in solids and phase growth kinetics form Chapter 4. Here, theory of diffusion and its mechanisms were discussed and concluded with phase growth kinetics and diffusion parameters. In Chapter 5, the thermodynamics of carbon-tungsten interactions are discussed in terms of solubility of carbon in tungsten, W-C phase diagram, mechanism of tungsten carbide formation and the phase formation sequence. Chapter 6 presents the sample preparation steps and discussion on the experimental techniques and analysis used in this study were provided. In Chapter 7, the experimental results from different analytical techniques were presented and discussed. In conclusion, Chapter 8 presents the summary of these results as well as the future work.

REFERENCES

[1] International Energy Agency (NEA), "Key world energy statistics," Paris, 2017.

[2] World Energy Council, "World energy resources," Paris, 2016.

[3] International Atomic Energy Agency (IAEA), "Energy, electricity and nuclear power estimates for the period up to 2050."

[4] S. Kakani and S. Kakani, *Nuclear and particle physics*. Viva Books, New Delhi, 2008.

[5] International Atomic Energy Agency (IAEA), "Nuclear power reactors in the world," Vienna, 2018.

[6] M. Balat, "The role of nuclear power in global electricity generation," *Energy Sources, Part B*, vol. 2, no. 4, pp. 381–390, 2007.

[7] B. Paul, *Electricity generation and the environment*. Academic Press, London, 2017.

[8] International Atomic Energy Agency (IAEA), "Options for management of spent fuel and radioactive waste for countries," Vienna, 2018.

[9] E. Sartori, "Nuclear data for radioactive waste management," *Annals of Nuclear Energy*, vol. 62, pp. 579–589, 2013.

[10] United States Nuclear Regulatory Commission (USNRC), "Radioactive waste: Production, storage and disposal," Washington, DC, 2002.

[11] R. Dohrmann, S. Kaufhold, and B. Lundqvist, "The role of clays for safe storage of nuclear waste," in *Developments in Clay Science*, vol. 5, Elsevier, 2013, pp. 677–710.

[12] R. Howard and B. Van den Akker, "Considerations for disposition of dry cask storage system materials at end of storage system life," Tech. Rep., 2014.

[13] R. D. McCright, W. G. Halsey, G. E. Gdowski, and W. L. Clarke, "Candidate container materials for Yucca mountain waste package designs," Lawrence Livermore National Lab., Tech. Rep., 1991.

[14] M. Yim and K. L. Murty, "Materials issues in nuclear-waste management," *JOM*, vol. 52, no. 9, pp. 26–29, 2000.

[15] W. C. Bare, M. A. Ebner, and L. D. Torgerson, "Dry cask storage characterization project-phase 1: Castor v/21 cask opening and examination," Idaho National Laboratory (INL), Tech. Rep., 2001.

[16] D. Wolff, H. Völzke, A Bevilacqua, C Alejano, J. Conde, R. Einziger, S.-I. Fukuda, A González Espartero, S Gouzy-Portaix, and R. Haddad Andalaf, "Demonstrating performance of spent fuel and related storage system components during very long term storage-final report of a coordinated research project," 2019.

[17] F. King, "Microbiologically influenced corrosion of nuclear waste containers," *Corrosion*, vol. 65, no. 4, pp. 233–251, 2009.

[18] W. M. Miller, N. Chapman, I. McKinley, R. Alexander, and J. Smellie, *Natural analogue studies in the geological disposal of radioactive wastes*. Elsevier, 2011.

[19] L. Werme, P. Sellin, and N. Kjellbert, "Copper canisters for nuclear high level waste disposal. corrosion aspects," Swedish Nuclear Fuel and Waste Management Co., Tech. Rep., 1992.

[20] United States Nuclear Waste Technical Review Board, "Evaluation of the technical basis for extended dry storage and transportation of used nuclear fuel," Washington, DC, 2010.

[21] International Energy Agency (NEA), "The safety of long-term interim storage facilities in NEA member countries," Australia, 2017.

[22] A. Attar, B. Gencturk, M. Hanifehzadeh, and K. Willam, "Accelerated aging of concrete dry cask storage systems for nuclear waste," *Journal of Advanced Concrete Technology*, vol. 14, no. 6, pp. 299–310, 2016.

[23] L. Caseres and T. S. Mintz, *Atmospheric stress corrosion cracking susceptibility of welded and unwelded 304, 304L, and 316L austenitic stainless steels commonly used for dry cask storage containers exposed to marine environments*. Southwest Research Institute, 2010.

[24] D. McCulloch, S Prawer, and A Hoffman, "Structural investigation of xenon-ion-beam-irradiated glassy carbon," *Physical Review B*, vol. 50, no. 9, pp. 5905–5910, 1994.

[25] A. Craievich, "On the structure of glassy carbon," *Materials Research Bulletin*, vol. 11, no. 10, pp. 1249–1255, 1976.

[26] M. I. Nathan, J. E. Smith Jr, and K. Tu, "Raman spectra of glassy carbon," *Journal of Applied Physics*, vol. 45, no. 5, pp. 2370–2370, 1974.

[27] E. G. Njoroge, L. Sebitla, C. Theron, M. Mlambo, T. T. Hlatshwayo, O. S. Odutemowo, V. Skuratov, E Wendler, and J. B. Malherbe, "Structural modification of indium implanted glassy carbon by thermal annealing and SHI irradiation," *Vacuum*, vol. 144, pp. 63–71, 2017.

[28] P. K. Chu and L. Li, "Characterization of amorphous and nanocrystalline carbon films," *Materials Chemistry and Physics*, vol. 96, no. 2-3, pp. 253–277, 2006.

[29] T. Noda, M. Inagaki, and S. Yamada, "A comment on the structure of glassy carbon," *Bulletin of the Chemical Society of Japan*, vol. 41, no. 12, pp. 3023–3024, 1968.

[30] S. Bukalov, L. Leites, A. Sorokin, and A. Kotosonov, "Structural changes in industrial glassy carbon as a function of heat treatment temperature according to Raman spectroscopy and X-ray diffraction data," *Nanosystems: Physics, Chemistry, Mathematics*, vol. 5, no. 1, pp. 186–191, 2014.

[31] A De Luca, A Portavoce, M Texier, C Grosjean, N Burle, V Oison, and B Pichaud, "Tungsten diffusion in silicon," *Journal of Applied Physics*, vol. 115, no. 1, pp. 135–141, 2014.

[32] V Philipps, "Tungsten as material for plasma-facing components in fusion devices," *Journal of nuclear materials*, vol. 415, no. 1, S2–S9, 2011.

[33] E. Lassner and W. D. Schubert, *Tungsten: Properties, chemistry, technology of the element, alloys, and chemical compounds*. Kluwer Academic / Plenum Publishers, New York, 1999.

[34] V. Lavrentiev, J. Vacik, and H. Naramoto, "Structural phenomena in glassy carbon induced by cobalt ion implantation," *Applied Physics A*, vol. 92, no. 3, pp. 673–680, 2008.

[35] T. T. Hlatshwayo, L. Sebitla, E. G. Njoroge, M. Mlambo, and J. B. Malherbe, "Annealing effects on the migration of ion-implanted cadmium in glassy carbon," *Nuclear Instruments and Methods in Physics Research Section B: Beam Interactions with Materials and Atoms*, vol. 395, pp. 34–38, 2017.

[36] D. Langa, N. Van Der Berg, E Friedland, J. B. Malherbe, A. Botha, P Chakraborty, E Wendler, and W Wesch, "Heat treatment of glassy carbon implanted with cesium at room and high temperatures," *Nuclear Instruments and Methods in Physics Research Section B: Beam Interactions with Materials and Atoms*, vol. 273, pp. 68–71, 2012.

CHAPTER

TWO

THE CARBON AND ITS POLYMORPHS

2.1 Introduction

Carbon is a nonmetallic element. It is the fourth most abundant element in the universe [1]. It is also the second abundant element in human body. Carbon is a unique element in many ways. Most importantly, it is crucial for life on earth because it formed the basis for all organic matters. Element carbon is present in abundance in the universe, in the sun, stars, comets, and in the atmosphere of the planets [2]. Many of these natural compounds are essential to the production of synthetic carbon materials. These include various coals (bituminous and anthracite), hydrocarbons complexes (petroleum, tar, and asphalt) and the gaseous hydrocarbons (e.g. methane). It is found mostly in the form of hydrocarbons and other chemical compounds.

2.2 The carbon polymorphism

Carbon atoms can exhibit three different hybrid orbitals, sp^3, sp^2 and sp^1. These three hybrid orbitals make it possible for carbon to exist in many forms [3]. The forms of carbon such as diamond, graphite, fullerenes and carbynes and host of others, are consequence of the ability of carbon to exhibit hybridization. The property of an element to exist in two or more forms, characterized by difference in physical properties but the same chemical properties is called allotropy [2]. The major natural allotropic forms of carbon are the crystalline forms comprising (diamond and graphite) and the amorphous carbon, which lacks crystalline structure.

There are also many synthetic forms of carbon such as fullerenes and glassy carbon, which combine two or three of the hybridized bond types. The carbon allotropes can display entirely different properties. For example, diamond is known to be the hardest material, while graphite is a soft solid. Diamond is transparent, while graphite is opaque. Diamond does not conduct electricity while graphite is a good conductor of electricity. Yet these two materials are composed of carbon atoms. The disparity in their properties is due to the difference in their structural configurations. Each allotropic form of carbon is discussed in the following sections.

2.2.1 Structure of diamond

It was stated above that sp^3 hybridization is responsible for the tetrahedral symmetry of the diamond structure. The four sp^3 hybridized orbitals are bonded to the orbitals of four other carbon atoms with a strong covalent bond to form a regular tetrahedron with equal angles of 109^o to each other (Figure 2.1). Diamond has several crystalline forms and polytypes, the two popular crystal structures are cubic and hexagonal diamond [4]. The diamond with cubic symmetry is most common and more stable than the hexagonal symmetry which is found in nature as the mineral lonsdaleite. The focus of

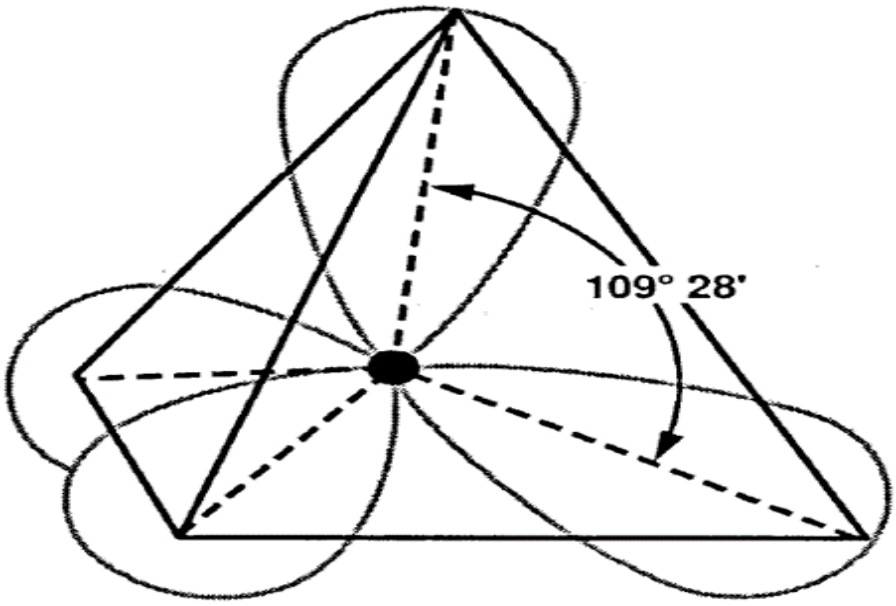

Figure 2.1: The tetrahedron structure of diamond [2]

this short description of diamond is on the cubic symmetry since it is the most common type. The covalent link between the carbon atoms of diamond is characterized by a small bond length 0.154 nm and a high bond energy of

713 kJ/mol. [5]. Diamond has extreme atom density of all materials, with atomic density of $1.77\times\ 10^{23}$ atoms/cm^3 [6]. Diamond is the stiffest and hardest of all substances. Another remarkable property of diamond is that, its high refractive index increases with the temperature [4]. Diamond is one of the most valuable and precious materials on Earth. Due to its excellent mechanical and optical properties, it is being used in a number of laboratory and industrial applications. For example, it is used in the manufacture of grinding, cutting and drilling tools due to its hardness and abrasion resistant. It is used in photonics for spectroscopy applications and manufacture of assorted ornamental materials.

2.2.2 Structure of graphite

Graphite is made up of series of stacked parallel plane layers with the covalent sp^2 bonding [7]. The carbon atom is bonded to three others within each plane layer, thereby producing a series of continuous hexagons which formed essentially infinite two-dimensional molecule (Figure 2.2). The sigma bonds by the hybridized orbitals are of high strength while the delocalized electron participates in bonding by the weak Van der Waals forces [3]. The layer stacking occurs in two ways, giving rise to hexagonal graphite and rhombohedral graphite structures. In the hexagonal graphite, the stacking sequence is ABABAB stacking order [7]. This means that the carbon atoms in all other layers are overlaid on each other. The thermodynamically stable form of graphite is the hexagonal form. The rhombohedral graphite has a

stacking sequence of ABCABC. Graphite is very useful for many industrial

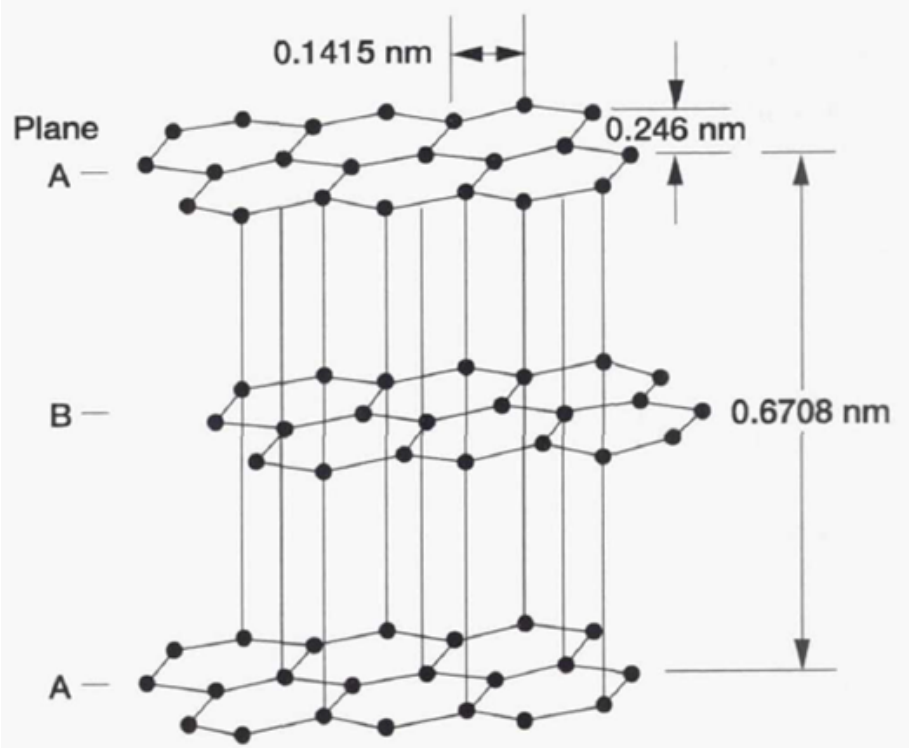

Figure 2.2: The hexagonal structure of graphite with ABAB stacking sequence [7]

processes where the high temperature stability, chemical inertness of graphite is in great demand. In some industries and laboratories, graphite is used as an electrode in the production of chemicals such as calcium carbide. Being a soft solid, graphite is used in the production of pencils. Graphite is used in the nuclear industry as neutron moderators. The mechanical properties of graphite is being harnessed in the manufacture of shafts, brake pads, piston rings in automobiles. As a good conductor of electricity, graphite is used in the manufacture of dry battery.

2.2.3 Structure of amorphous carbon

Structurally, amorphous carbon is composed of a mixture of two or even all of the sp^3, sp^2 and sp^1 hybrid bonds, with a possibility of containing up to 60 at.% hydrogen, as an impurity [8]. This is commonly referred as hydrogenated amorphous carbon, denoted by a-C:H. There are also, the hydrogen free amorphous carbon usually denoted by a:C [9]. The properties of amorphous carbon depend on the ratio of sp^2 to sp^3 hybridized bonds present in the material. Graphite consists purely of sp^2 hybridized bonds, whereas diamond consists purely of sp^3 hybridized bonds.

Amorphous carbon with high content in sp^3 hybridized bonds are referred to as tetrahedral amorphous carbon, due to the tetrahedral shape formed by the sp^3 hybridized bonds. Amorphous carbons are prepared by pyrolysis of organic polymer at temperatures below 1500 °C [10]. The structural development and final properties depend largely on the nature of the starting material and the preparation history. Amorphous carbon is known to be hard, abrasion resistant and has low thermal and electrical conductivities.

2.2.4 Structure of fullerenes

The fullerenes are another important allotropes of carbon. They have stable, finite and discrete molecular structure. They are different from diamond and graphite, which are not molecular but infinite-network of solids. The fullerenes are arranged into spherical shape without boundaries. The

fullerenes are formed from hybridized bonds linked to a mixture of sp^3 and sp^2 bonds. The first stable fullerene and the first to be discovered is the C_{60}, also known as buckyball [2]. Other higher molecular structure which are more stable have been identified and are structurally characterized as C_{70}, C_{76}, C_{78} and C_{84}. Figure 2.3 presents the schematic diagram of fullerene C_{60} molecular structure. It was suggested that C_{60} is the softest of the solid phases of carbon.

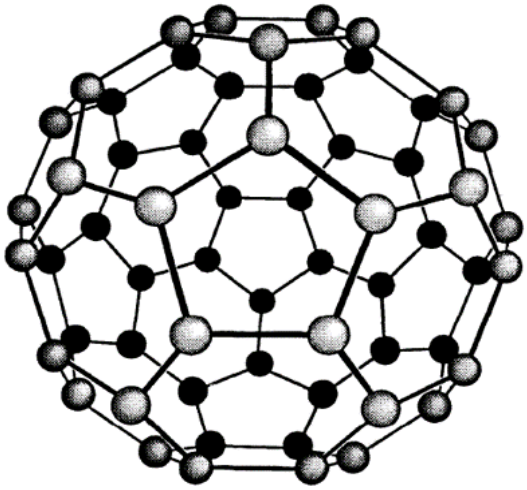

Figure 2.3: The fullerene C_{60} molecule [2]

However, calculations have shown that, when compressed to less than 70% of its initial volume under high pressure, they could be harder than even diamond [11]. Fullerenes are resilient and have high strength.

2.3 The glassy carbon

Glassy carbon, also called vitreous carbon, is a non-graphitizeable form of carbon [12]. It combines glassy and ceramic properties with those of graphite.

It takes its name from its shiny surface which looks like glass. The characteristic shared by all carbon materials, irrespective of their properties, is that they were all formed from organic precursors by a process called carbonization or pyrolysis. Pyrolysis is the process in which the organic precursor is transformed into a carbon material. It involves the organic precursor being heated slowly in an inert environment, over a range of high temperature, to obtain the carbon materials. Slow heating ensured that disruption and rupture of the carbon network is avoided [2], [13]. At high temperature, the organic precursor decomposed into a carbon residue while the volatile compounds diffuse out to the atmosphere. The carbon content of the residue is a function of the nature of the precursor and the pyrolysis temperature used. It usually exceeds 90% by weight at 900 °C and 99% by weight at 1300 °C [2].

The residual carbon materials formed after the pyrolysis of organic polymers, are essentially all carbon, with the following features [2]. The structures of the carbon materials have little graphitic ordering and consist of an aggregate of small crystallites. These crystallites are randomly oriented in different directions. The carbonized material is often referred to as amorphous or baked carbon. It is without long-range crystalline order.

Glassy carbon, being a carbon material is produced also by the pyrolysis of organic precursors. It is made from non - melting organic polymers by thermal degradation and conserves exactly the same morphology as that of the polymeric precursor in spite of volume shrinkage [14] during pyrolysis.

It has a structure that is more closely related to that of a glass material, that is, non-crystalline [2], while retaining the physical and chemical properties of carbon material. It has some remarkable properties, such as high strength, high resistance to chemical attack, and extremely low gas permeability. It does not graphitize readily. It is being produced in various shapes and sizes from a variety of thermosetting organic resins under different trade names by various manufacturers [13].

Glassy carbon, like other carbon products, is derived from organic polymers, mainly polyfurfuryl alcohol and phenolic resin [13] by pyrolysis as stated above, at high temperatures up to 3000 °C, in some cases. The polymeric precursors for production of glassy carbon must have these three characteristics to be considered a suitable precursors [2]; (i) The structure of the organic molecule must be cross-linked in three-dimension. (ii) Carbonization must take place in the solid state, without mesophase formation, and result in the formation of a char. (iii) The molecular weight and the degree of aromaticity (i.e benzene rings content) must be high to provide a relatively high carbon yield. These polymeric precursors, polyfurfuryl alcohol and phenolic resin have been used in the production many grades of glassy carbon [15], [16]. Polyfurfuryl alcohol is a thermosetting resin which is obtained by the polymerization of the furfuryl alcohol monomer catalysed with maleic acid. It has the chemical structure shown in Figure 2.4(a). Phenolic resins are class of organic polymers obtained by a condensation reaction, usually between phenol and formaldehyde [14]. This monomer unit, which combines with

other units to form the polymer has the chemical structure as given in Figure 2.4(b). When heated to a temperature of 250 °C, extensive cross-linking occurs, and a hard, rigid and insoluble polymer is obtained. The polymeric

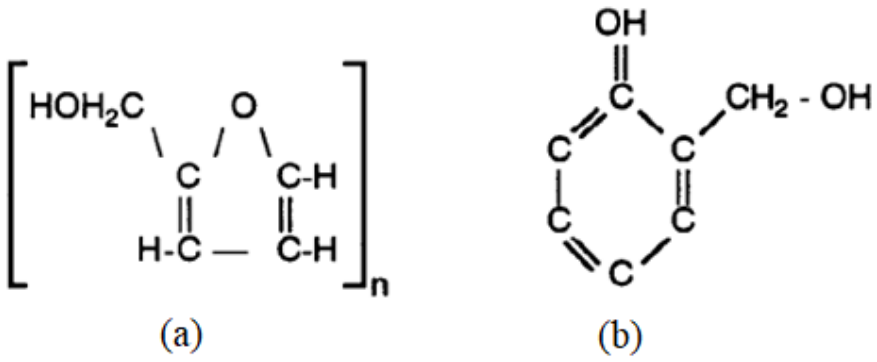

Figure 2.4: The unit structure of (a) polyfurfuryl alcohol (b) phenolic resin monomer [2], [14], [15]

precursors are often combined with other materials such as solvents to obtain the desired characteristics of the pyrolysis products. These compositions and processes are somewhat secret and considered proprietary by the glassy carbon manufacturers.

2.3.1 The structure of glassy carbon

Glassy carbon has a turbostratic structure in which randomly orientated graphitic planes are arranged in ribbons [17]. Despite the various manufacturing methods from different polymeric precursors, the mechanical properties of the products are fairly the same. The residual carbon material obtained after high temperature pyrolysis of organic precursor is essentially all carbon, called glassy carbon. A substance is considered vitreous (or glassy) when it

has no crystalline long-range order [2]. This means that the structure of glassy carbon is characterized by a small, randomly oriented crystallites ($L_c \approx 3$ nm) [18]. This random structure is believed to have the form of an extensive and stable network of graphitic ribbons [19] with sp^2 bonds (Figure 2.6). These ribbon-like tangled aromatic molecules are cross-linked by carbon-carbon covalent bonds with varying bond energies. It is believed that the graphitic layers in glassy carbon memorized the tangled structure of the polymeric precursor [20].

The structure of glassy carbon has been a research focus among many researchers since it was produced in the early 1960s [21]. Many researchers have expended a lot of energy, in a bid to unravel the structure of glassy carbon. A good number of the structural models were proposed for glassy carbon in the past. Some of the early investigators believed that the material had both sp^2 and sp^3 bonds. It is believed that glassy carbon contained the graphitic structure which intermingled with the tetrahedral domains.

It has been suggested that in addition to the graphitic sp^2 trigonal bond, the structure of glassy carbon also has some sp^3 tetragonal bonds which are characteristic of diamond structure [22]. It was believed that this would possibly contribute to the high strength and the hardness of glassy carbon. Thus, the presence of ribbon network of graphite and sp^2 tetragonal bonds, would prevent the structure glassy carbon from further ordering, irrespective of the graphitization temperature. One of the early popular models for the

structure of glassy carbon is shown in Figure 2.5. This structural model was credited to Noda and Inagaki [22], who proposed that the three-dimensional network of carbon atoms in glassy carbon is composed of tetrahedral parts (T-parts) and graphitic parts (G-parts), shown in Figure 2.5(a). The nearest neighbour distance in T-parts is 0.155 nm corresponding to a normal covalent single bond found around the tetrahedral carbon, while that in G-parts is 0.142 nm. This model was later modified by Yamada and Sato [23], [24] who suggested that oxygen atoms existed between T- and T-, T- and G-, and G- and G-parts along their boundaries as shown in Figure 2.5(b). It was believed that the oxygen bridges hinder the glassy carbon from graphitization upon heat treatments at temperatures lower than 1100 °C, but were destroyed by the heat treatments at temperature range of 2500 - 3000 °C.

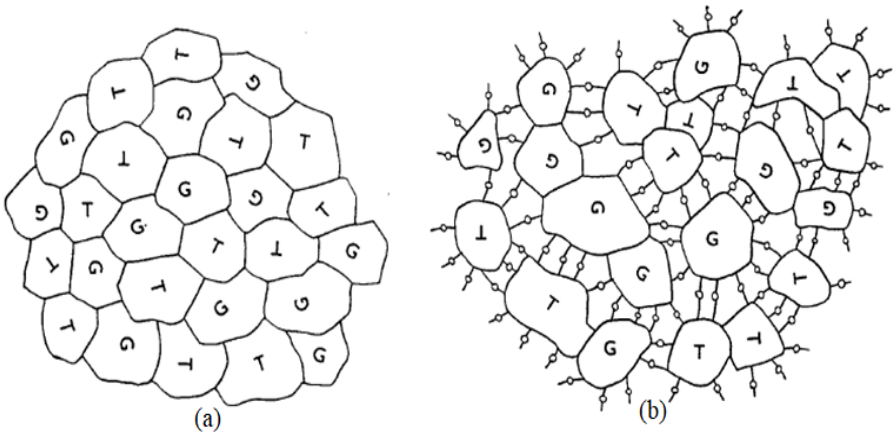

Figure 2.5: The early structural model for glassy carbon. (a) The structural model for glassy carbon proposed by Noda and Inagaki [22], T was a tetrahedral part in which the nearest neighbour distance was 0.155 nm and G, a graphitic part in which the nearest neighbor distance was 0.142 nm (b) The modified structural model for glassy carbon by Yamada and Sato [23], [24]. T was tetrahedral part; G graphite part; -o- oxygen bridge

.

A much popular model for the structure of glassy carbon was that proposed by Jenkins and Kawamura [19]. This model depicted in Figure 2.6, was based on the assumption that the molecular structure of the organic precursor is memorized and replicated in the carbonized glassy carbon. Hence, the structure of glassy carbon bears some resemblance to that of the polymeric precursor from which it was formed. The organic precursors normally are made of narrow fibrils which are twisted ribbons of graphitic domain.

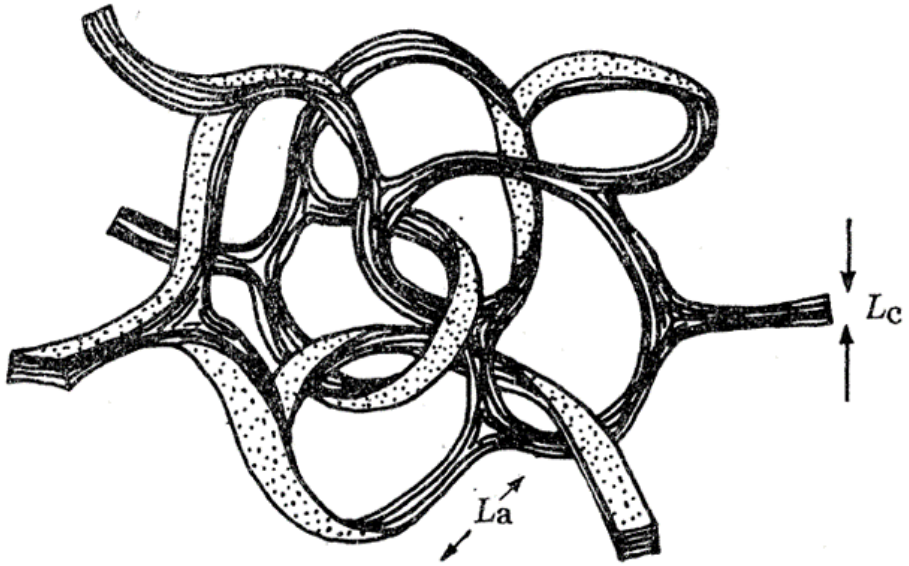

Figure 2.6: The Jenkins - Kawamura model of glassy carbon. L_a and L_c are the lengths of the graphitic domains perpendicular and parallel to the graphite c axis [19]

The model depicted in Figure 2.6, has many pores. It was expected that a structure such as this, should be easily permeable to gases. But this is contrary to the impermeability property of glassy carbon to gases. In addition, this model also shows a high proportion of edge atoms, which are believed to have a relatively high reactivity compared to the in-plane carbon atoms. This

again, was an aberration with the inert reactivity of glassy carbon. These are the two major drawbacks of Jenkins model.

The discovery of fullerenes by Kroto *et al.* [25] demonstrated that sp^2 bonded carbons containing non six- membered rings can be highly stable. Motivated by this, Harris [21] tried to explore the possibility that non-graphitizing carbons might have structures related to those of the fullerenes. Detailed studies of non-graphitizing carbons were carried out by Harris and Tsang [13], using high resolution transmission electron microscopy. These studies provided evidence for fullerene-related structure of glassy carbon. And consequently, a model was proposed for the structure of non-graphitizing carbons. This structure is believed to be made up of discrete fragments of curved carbon sheets, in which pentagons and heptagons were randomly distributed throughout networks of hexagons, depicted in the Figure 2.7 below.

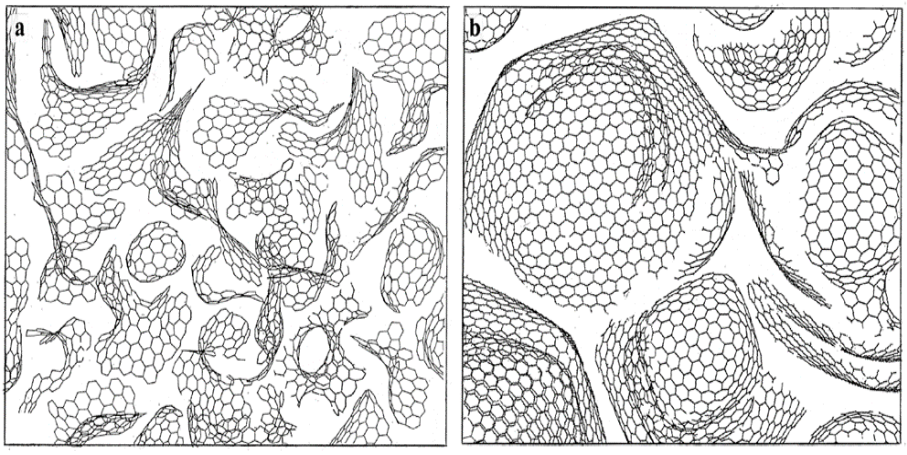

Figure 2.7: Models for the structure of non-graphitizing carbons (a) low-temperature and (b) high-temperature [13].

2.3.2 Properties of glassy carbon

Studies have shown that glassy carbon is characterized by the following properties [2], [13]; low permeability to gases, essentially non-porous, generally high resistance to chemical attack and is one of its outstanding characteristics. In many instances, it is far more chemically resistant than other forms of carbon, such as pyrolytic graphite. Glassy carbon does not react with nitric, sulfuric, hydrofluoric and chromic acids. It cannot be attacked by halogens such as bromine, even at high temperatures, as opposed to other graphitic materials which are attacked rapidly.

2.3.3 Applications of glassy carbon

2.3.3.1 Chemical applications

Many applications of vitreous carbon are based on its outstanding chemical resistance. These applications include vessels for chemical processing and analytical chemistry such as crucibles, beakers, boats, dishes, reaction tubes, lining for pressure vessels. Glassy carbon is also highly resistant to attack by acids. Thus, while normal graphite is reduced to a powder by a mixture of concentrated sulphuric and nitric acids at room temperature, glassy carbon is unaffected by such treatment, even after several months. This property makes glassy carbon a useful material for crucibles [2]. It is also used widely as an electrode material in electrochemistry, and its biocompatibility makes it a potential component of prosthetic devices.

2.3.3.2 Metallurgical and glass applications

Vitreous carbon reacts with metallic elements (Ti, Zr, Hf, Nb, Ta, W) in groups IV, V and VI of the Periodic table [2] to form carbides. However, it is inert to and not wetted by other molten metals and, for that reason, it is used widely as crucibles for the melting of noble metals and special alloys, particularly in dental technology. Vitreous carbon is not wetted by glass and is used as mold for lenses and other glass products.

2.3.3.3 Potential applications for glassy carbon

The chemical inertness and good electrical conductivity of vitreous carbon makes it a potentially excellent material for acid-battery electrodes. Due to its biocompatibility, glassy carbon is been investigated for possible use in heart valves, dental implants and transcutaneous access device [12], [26], [27]. In addition, it has a potential applications in the nuclear industry. It is been consider for use in encapsulating of nuclear fuel [28]. It might also find application as a protective layer on the graphite reactor core surface in molten salt breeder reactors [29]. It is been considered also, as a new material for long term nuclear waste storage [30]. This is the aspect of future applications of glassy carbon, for which this thesis is trying to make contribution.

REFERENCES

[1] Z. Ren, Y. Lan, and Y. Wang, *Aligned carbon nanotubes: Physics, concepts, fabrication and devices*. Springer Science & Business Media, London, 2012.

[2] H. Pierson, *Handbook of carbon, graphite, diamond and fullerenes*. Noyes Publications Park Ridge, New Jersey, 1993.

[3] M. Inagaki and F. Kang, *Materials science and engineering of carbon: Fundamentals*. Butterworth-Heinemann, London, 2014.

[4] C. Raman, "The diamond: Its structure and properties," in *Proceedings of the Indian Academy of Sciences-Section A*, Springer, vol. 67, 1968, pp. 231–246.

[5] W. D. Callister Jr and D. G. Rethwisch, *Fundamentals of materials science and engineering: An integrated approach*. John Wiley & Sons, New York, 2012.

[6] J. Biener, D. Ho, C. Wild, E. Woerner, M. Biener, B. El-dasher, D. Hicks, J. Eggert, P. Celliers, and G. Collins, "Diamond spheres for inertial confinement fusion," *Nuclear Fusion*, vol. 49, no. 11, pp. 112–119, 2009.

[7] K. Miyoshi, "Structures and mechanical properties of natural and synthetic diamonds, lewis research center, ohio," NASA TM-1998-107249, Tech. Rep., 1998.

[8] A. C. Ferrari and J. Robertson, "Interpretation of Raman spectra of disordered and amorphous carbon," *Physical review B*, vol. 61, no. 20, pp. 140–165, 2000.

[9] J. Robertson, "Amorphous carbon," *Current Opinion in Solid State and Materials Science*, vol. 1, no. 4, pp. 557–561, 1996.

[10] E. Falcao and F. Wudl, "Carbon allotropes: Beyond graphite and diamond," *Journal of Chemical Technology & Biotechnology: International Research in Process, Environmental & Clean Technology*, vol. 82, no. 6, pp. 524–531, 2007.

[11] J. E. Fischer, P. A. Heiney, and A. B. Smith III, "Solid-state chemistry of fullerene-based materials," *Accounts of chemical research*, vol. 25, no. 3, pp. 112–118, 1992.

[12] M. Hassler, "Other commonly used biomedical coatings: Pyrolytic carbon coatings," in *Coatings for biomedical applications*, Elsevier, London, 2012, pp. 75–105.

[13] P. J. Harris and S. C. Tsang, "High-resolution electron microscopy studies of non-graphitizing carbons," *Philosophical Magazine A*, vol. 76, no. 3, pp. 667–677, 1997.

[14] E. Fitzer, "Polymer carbon the start into a new age of polymer application," in *Contemporary Topics in Polymer Science*, Springer, London, 1984, pp. 101–138.

[15] R. Aggarwal, G. Bhatia, O. Bahl, and M. Malik, "Development of glass-like carbon from phenol formaldehyde resins employing monohydric and dihydric phenols," *Journal of materials science*, vol. 23, no. 5, pp. 1677–1684, 1988.

[16] E. Fitzer, W. Schaefer, and S. Yamada, "The formation of glasslike carbon by pyrolysis of polyfurfuryl alcohol and phenolic resin," *Carbon*, vol. 7, no. 6, pp. 643–648, 1969.

[17] J. Bokros, "Carbon biomedical devices," *Carbon*, vol. 15, no. 6, pp. 353–371, 1977.

[18] M. Jenkins, K. Kawamura, and L. Ban, "Formation and structure of polymeric carbons," *Proceedings of the Royal Society of London. Mathematical and Physical Sciences*, vol. 327, no. 1571, pp. 501–517, 1972.

[19] G. Jenkins and K. Kawamura, "Structure of glassy carbon," *Nature*, vol. 231, no. 5299, pp. 175–180, 1971.

[20] A. Craievich, "On the structure of glassy carbon," *Materials Research Bulletin*, vol. 11, no. 10, pp. 1249–1255, 1976.

[21] P. Harris, "Fullerene-related structure of commercial glassy carbons," *Philosophical Magazine*, vol. 84, no. 29, pp. 3159–3167, 2004.

[22] T. Noda and M. Inagaki, "The structure of glassy carbon," *Bulletin of the Chemical Society of Japan*, vol. 37, no. 10, pp. 1534–1538, 1964.

[23] S. Yamada and H. Sato, "Some physical properties of glassy carbon," *Nature*, vol. 193, no. 4812, pp. 261–270, 1962.

[24] S. Yamada, "A review of glasslike carbons," Battele memorial inst. Columbus OH, Defense ceramic information center, Tech. Rep., 1968.

[25] H. Kroto, "Jr heath. sc o'brien, rf curl and re smalley," *Astrophys. J*, vol. 314, pp. 352–358, 1987.

[26] T. Tarvainen, H. Pätiälä, T. Tunturi, I. Paronen, K. Lauslahti, and P. Rokkanen, "Bone growth into glassy carbon implants: A rabbit experiment," *Acta orthopaedica Scandinavica*, vol. 56, no. 1, pp. 63–66, 1985.

[27] T Albrektsson, G Zarb, P Worthington, and A. Eriksson, "The long-term efficacy of currently used dental implants: A review and proposed criteria of success," *Int j oral maxillofac implants*, vol. 1, no. 1, pp. 11–25, 1986.

[28] M. Hrovat, H. Huschka, and L. Rachor, "Process for conditioning radioactive and toxic wastes," pat., 1983.

[29] V. Bernardet, S. Gomes, S. Delpeux, M. Dubois, K Guérin, D. Avignant, G. Renaudin, and L Duclaux, "Protection of nuclear graphite toward fluoride molten salt by glassy carbon deposit," *Journal of Nuclear Materials*, vol. 384, no. 3, pp. 292–302, 2009.

[30] J. B. Malherbe, O. Odutemowo, E. Njoroge, D. Langa, T. Hlatshwayo, and C. Theron, "Ion bombardment of glassy carbon," *Vacuum*, vol. 149, pp. 19–22, 2018.

CHAPTER

THREE

TUNGSTEN AND ITS PROPERTIES

3.1 Introduction

Tungsten is a dull silver-coloured metallic element. It has the highest melting point of all pure metals, with a temperature of 3410 °C [1]. Tungsten is a transition element that belongs to group VI and period VI of the periodic table [2]. Being a transition metal, it is characterized by variable valence states, with oxidation states in various chemical compounds ranging from +1 to +6 [3]. Tungsten is not oxidized in air at ambient temperatures and is highly resistant to acids. Its chemical properties resemble those of molybdenum. Tungsten is also known as Wolfram, from which the element takes its symbol, W [2]. It is more resistant to fracture than diamond and is much harder than steel. This refractory metal has some unique properties. Its high strength and ability to withstand high temperatures, make it an ideal material for many commercial and industrial applications.

3.2 The electronic configuration and isotopes

Tungsten has atomic number of 74. The electronic configuration of the neutral atom of tungsten is given by [Xe]$4f^{14}5d^{4}6s^{2}$ [3]. The electrons in the partially filled *d*-orbital and *s*-orbital are available for forming variable oxidation states. The atomic weight of tungsten in its natural isotopic composition as agreed upon by the International Union of Pure and Applied Chemistry is 183.86 g/mol [3]. It contains 74 protons in its nucleus besides 84 to 116 neutrons. Thirty-five isotopes of tungsten are known. Five of them are naturally occurring while the rest can be formed artificially and are unstable. The half-life of these unstable isotopes varies between milliseconds and more than 200 days [4]. The properties of the natural and eight of the more important artificial isotopes in relation to decay mode and abundance are listed in Table 3.1.

Table 3.1: Isotopes of tungsten [5]

Mass number	Half-life	Decay mode	Abundance (%)
176	80 min	electron capture	—
177	130 min	electron capture	—
178	21.5 days	electron capture	—
179	30 min	electron capture	—
180	—	stable	0.1
181	145 days	electron capture	—
182	—	stable	26.4
183	—	stable	14.4
184	—	stable	30.7
185	73.2 days	$\beta-$	—
186	—	stable	28.4
187	24.1 hrs	$\beta-$	—
188	69.5 days	$\beta-$	—

3.3 Structural properties of tungsten

Tungsten exhibits two forms of polymorphic structures. These are the stable alpha-tungsten (α-W) and a metastable beta-tungsten (β-W) [3]. The stable form of tungsten (α-W) is simply referred to as tungsten. This stable form has a body-centred cubic (BCC) crystal structure, with two atoms per unit cell and a lattice constant of 0.3165 nm [6]. At room temperature, tungsten has the shortest interatomic distance of 0.2741 nm and a density of 19.3 g/cm^3 [3]. The density of tungsten is the same as that of gold. This density value is among the highest of all metals.

Figure 3.1 shows the XRD pattern for α- tungsten. The XRD technique showed that the crystal structure for α-tungsten is BCC and the preferred orientation is the (110) crystal plane. The β-W is considered as a metastable form of tungsten [7] . It generally contains small amounts of oxygen. Hence, it has therefore been regarded as W_3O [3]. Although, measurements have shown that the β-form is actually an allotropic tungsten modification [8]. The structure of β-W is cubic with eight atoms per unit cell. The lattice constant is 0.505 nm, with a density of density of 18.9 g/cm^3, at room temperature [3]. The shortest interatomic distance is 0.252 nm.

3.4 Defects in tungsten

There is no such thing as perfect crystal in reality. Even in a tungsten sample considered to be chemically pure, it is impossible to obtain a perfect crystal

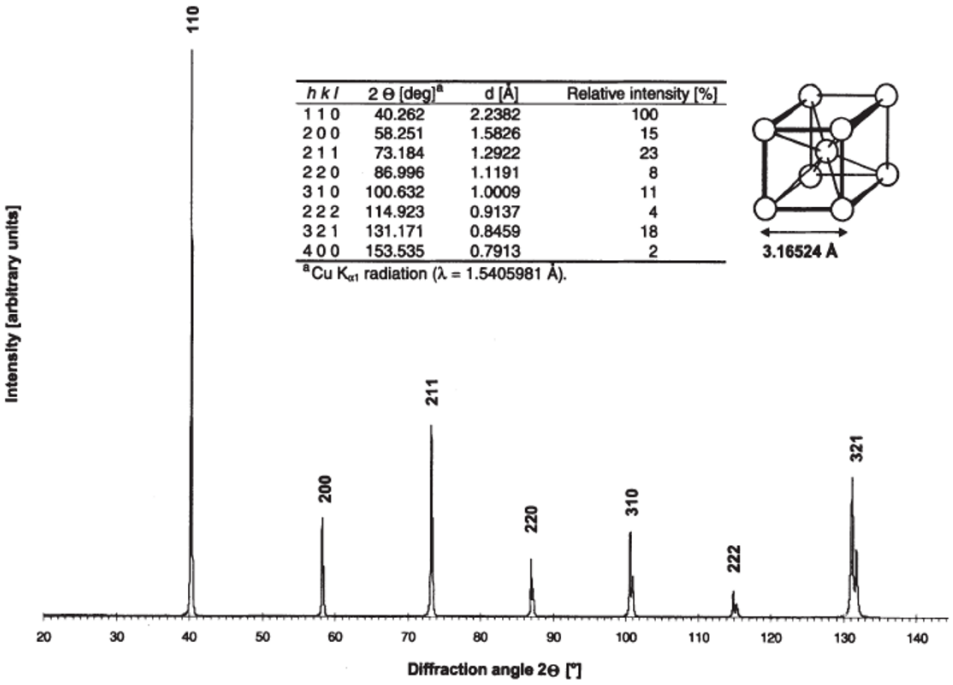

h k l	2 Θ [deg][a]	d [Å]	Relative intensity [%]
1 1 0	40.262	2.2382	100
2 0 0	58.251	1.5826	15
2 1 1	73.184	1.2922	23
2 2 0	86.996	1.1191	8
3 1 0	100.632	1.0009	11
2 2 2	114.923	0.9137	4
3 2 1	131.171	0.8459	18
4 0 0	153.535	0.7913	2

[a] Cu $K_{\alpha 1}$ radiation (λ = 1.5405981 Å).

Figure 3.1: X-ray diffraction diagram of α-tungsten [9]

lattice, because defects are always present. The number of defects present largely depends on the temperature of treatment and degree of deformation. Generally, lattice imperfections are divided into four groups [4]. These are point defects (vacancies, self-interstitial atoms, impurity atoms); line defects or dislocations; planar defects (stacking faults, grain boundaries, twins); and volume defects (voids, microcracks). The common defects in solids are discussed in detail in Chapter 4.

Vacancies: The activation energy for vacancy formation in tungsten has been found to be between 2.8 and 4.5 eV/atom [4]. The vacancy concentration

c in cm^2/s is given by [4]:

$$c = 760 \exp\left(-\frac{603kJ}{RT}\right) \tag{3.1}$$

where R is the universal gas constant and T is absolute temperature. The vacancy concentration increases substantially at high temperatures comparable with the melting point of tungsten.

Interstitial impurities: In a body centred cubic (BCC) lattice, two interstitial sites can be occupied. These are the octahedral and the tetrahedral sites. Carbon, oxygen and nitrogen always occupy the octahedral site while hydrogen takes the tetrahedral position in the tungsten host lattice [4]. Interstitial impurities cause lattice distortions to the host and thereby altering the mechanical properties.

Dislocations: Dislocation densities, that is, dislocation lines/cm^2 in the electron-beam-zone refined tungsten have been measured to be between 5 $\times$ 10^3 and 10^6 lines/cm^2 [3]. In the cold-worked foils, filings, rods and thin tungsten wires, the dislocation densities vary between 10^8 and 10^{12} lines/cm^2. [3]

3.5 Mechanical Properties of tungsten

For highly pure single crystalline tungsten, the mechanical properties are considered as intrinsic. From a technical point of view, poly-crystalline tungsten is the most important form of tungsten and, by far, the largest form of the

metal used for industrial and commercial purposes. Mechanical properties of tungsten are strongly influenced by the microstructure and the presence of interstitial impurities.

Microstructure: The microstructure of tungsten largely depends on its method of preparation. The widely used preparation methods are powder metallurgy, electron beam melting, zone refinement, chemical vapor deposition and the subsequent working (deformation, annealing, recrystallization) [4]. In the case of powder metallurgical processing, the crystal size and shape can be regulated by the sintering conditions, the type and degree of deformation. This way, it is possible to produce material of desired mechanical properties. Figure 3.2 presents examples of different microstructures arising from poly-crystalline tungsten due to different processing methods. This demonstrates how the processing method dictates the microstructure which in turn affects the mechanical properties and performance of tungsten specimen.

Impurity: Impurity atoms can be contained in tungsten in different modes. These modes are either homogeneously or quasi-homogeneously distributed. Interstitial impurities are often present in solid solution with tungsten. The solubility limit for interstitial elements such as hydrogen, nitrogen, oxygen and carbon in the host tungsten, at room temperature, is usually very low [10]. The solubility limit of these impurity elements at the melting temperature of tungsten usually increase substantially.

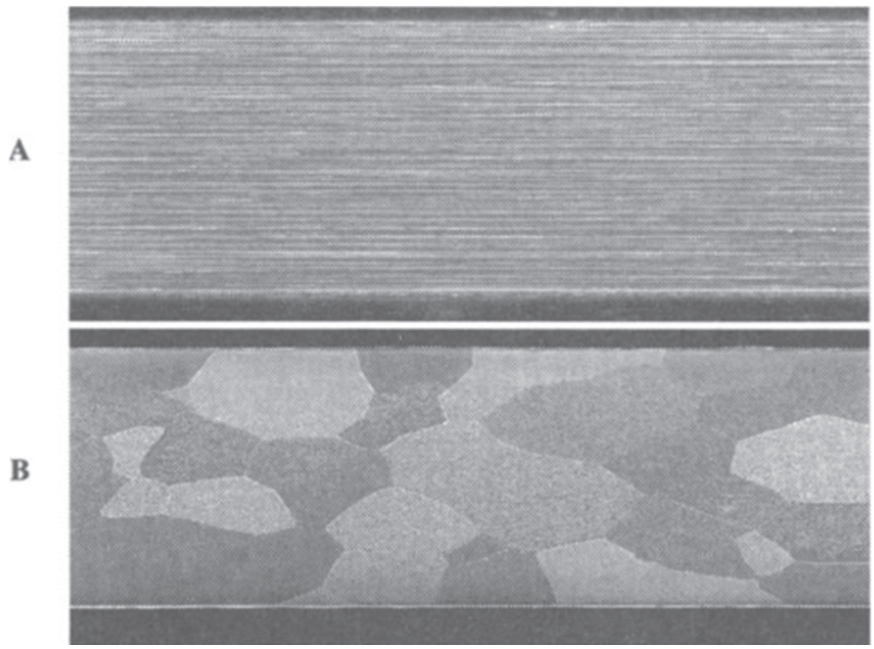

Figure 3.2: Microstructures of tungsten wires: (A) fibrous structure of as-drawn tungsten wire, (B) equiaxed grain structure of recrystallized pure wire. Adapted from [4]

3.5.1 Elastic properties of tungsten

Tungsten is one of the strong metallic elements. Like other metals, the mechanical properties of tungsten depend largely on the degree of cold work it was subjected to. The values for elastic properties for tungsten at room temperature are very high compared to other metals. At room temperature, the elastic constants for poly-crystalline tungsten have been measured to have the following range of values. Elastic modulus (390 - 410 GPa), bulk modulus (305 - 310 GPa) and Poisson's ratio (0.28 - 0.30) [11]. The elastic modulus (E_T) and compressional modulus (L_T) for poly-crystalline tungsten are temperature dependent. Their dependencies on absolute temperature T are expressed as

follows; [12]:

$$E_T = E_o \left(\frac{T_m - T}{T_m} \right)^{0.263} \tag{3.2}$$

$$L_T = (5.2 \times 10^{14}) - (3.7 \times 10^{10})T - (4.6 \times 10^{6})T^2 \tag{3.3}$$

where E_o is the elastic modulus at room temperature and T_m is the melting temperature of tungsten in Kelvin. The Vickers hardness for poly-crystalline tungsten at 0 °C and 400 °C are 450 and 240, respectively [13]. The hardness of poly-crystalline tungsten increases with reduction in the grain size. It was shown that hardness H and the mean grain size D obey the Hall-Petch relationship [14]:

$$H = H_o + K_H D^{-1/2} \tag{3.4}$$

where the constants H_o and K_H have the values of 350 kg/mm^2 and 10 $kg/mm^{-3/2}$, respectively. Grain size reduction gives rise to many grain boundaries, hence dislocation movement is restricted. This resulted in more strength of the material.

Tungsten exhibits a brittle characteristic during loading at certain temperature range. This behavioural change is known as the ductile-to-brittle transition temperature (DBTT), the minimum temperature at which a material can absorb certain amount of energy without fracture [4]. The temperature range for this behaviour is normally within the range of 200 - 300 °C [4]. The brittleness of poly-crystalline tungsten is linked to the weak grain boundaries, which gives rise to crack initiation. The DBTT of tungsten can be improved by

appropriate alloying with metals such as rhenium, titanium, technetium and osmium [15]. Pure single crystalline tungsten is always very ductile. Even as low as -253 °C, single crystalline tungsten still retain its ductility.

3.5.2 Strength of tungsten

The strength and creep properties of tungsten are very important indices for its application as structural material. At room temperature, poly-crystalline tungsten can possess ultimate tensile strength as high as 1470 MPa [3]. This value increases significantly with appropriate cold working. Calculations have shown that at room temperature, the ideal tensile strength of tungsten along the (100) plane was 61 GPa, while the ideal shear strength along the (110) plane ranged from 16.5 - 19 GPa [16]. These high values are reflections of the high bond energy in the BCC crystal structure of tungsten.

3.6 Thermal properties of tungsten

Among all the metallic elements, tungsten has the highest melting point. This is an important property in regard to many applications of refractory metals of which tungsten is one. The linear expansivity of tungsten is 4.68×10^{-6} K^{-1} at room temperature [3], [4]. At a temperature range of 293 - 1395 K, the linear expansivity of α-tungsten varies with temperature and its temperature dependence is given by [4];

$$\alpha = 10^{-6}(T - 293)[4 + (T - 293)9 \times 10^{-4} - 2 \times 10^{-7}(T - 293)^2] \qquad (3.5)$$

where T is absolute temperature.

Generally, the linear expansivity increases with temperature rise. The tungsten's thermal conductivity coefficient λ is 1.75 W.cm$^{-1}K^{-1}$ [17] at room temperature. At temperatures between 1200 and 2800 K, the coefficient of thermal conductivity λ is temperature dependent according to Equation 3.6 [17];

$$\lambda = 1.083 - 1.052 \times 10^{-4}T + \frac{234.199}{T} \tag{3.6}$$

where T is absolute temperature. The high thermal conductivity of tungsten in combination with its low specific heat capacity results in high cooling rates during hot-working of this metal. This makes the handling during hot-working process more difficult [4]. Tungsten is thermally stable, characterized by low thermal expansion property. This makes tungsten compatible with ceramics and glass in high temperature applications.

At certain elevated temperatures, tungsten experiences self-diffusion. This diffusion process is temperature dependent according to the Arrhenius equation [18];

$$D = D_o \exp\left(-Q/kT\right) \tag{3.7}$$

where D_o, Q, k and T are the pre-exponential, activation energy, Boltzmann constant and absolute temperature, respectively. The activation energies for tungsten self - diffusion were obtained between 502 and 586 kJ.mol^{-1} [19], [20] for polycrystalline tungsten, while the values of activation energies between 586 and 628 kJ.mol^{-1} [19], [20] were obtained for single crystalline tungsten.

This is due to significant contribution of grain boundary diffusion to the total volume diffusion in the poly-crystalline tungsten.

The creep behaviour of poly-crystalline tungsten, is of vital importance for their high temperature applications. The steady-creep rate ε for poly-crystalline tungsten is expressed by [21];

$$\varepsilon = B\sigma^n \exp(-Q/kT) \tag{3.8}$$

where B, n and k are constants, σ is the applied stress, Q is the activation energy for creep formation and T is the absolute temperature. To fully harness the great potential of tungsten for high temperature applications, the high temperature strength and creep resistance of tungsten can be improved by dispersion strengthening and precipitation hardening [4]. Solid solution strengthening by additions of Mo, Nb, and Ta can also improve the high temperature strength and creep resistance of tungsten.

3.7 Absorption property of tungsten

The tungsten being a heavy metal is used for many applications, where the high specific weight of the material plays an important role. The attenuation of X-ray radiation, which passes through a material of thickness x (cm), is given by [22];

$$I = I_o \exp(-\mu x) \tag{3.9}$$

where I is the intensity of the transmitted beam, I_o the intensity of the incident beam and μ is the linear absorption coefficient. Instead of μ, sometimes the mass absorption coefficient μ/ρ is used, given that ρ is the density of the absorber. The mass absorption coefficient for X-rays in tungsten is a function of X-ray wavelengths. Due to its high density and massive nucleus, tungsten is an effective X-ray absorber. Therefore, tungsten and some of its compounds have high absorption ability for X-rays and γ-rays. Due to this absorption property, tungsten finds application as a shield material at industrial scale.

3.8 Applications of tungsten

The applications of metallic tungsten are mainly based on its characteristic high melting point, high strength at elevated temperatures, resistance to wear and good thermal and electric conductivities. The largest application of tungsten is in the steel industry [3]. Tungsten is one of the components of special steels and hard-metals. These materials are used in large quantities for construction of variety of structures.

Due to its high atomic number and refractory properties, tungsten is used in the construction of X-ray cathode tubes, widely used for medical purposes. In Table 3.2, some of the common applications of tungsten in connection with the properties are summarized.

Table 3.2: Some applications of tungsten driven by properties[3]

Applications	High melting point	Good thermal conductivity	Good electrical conductivity	Good mechanical properties	Large atomic size
(i)Lamp filaments, strips and cathodes	×	×	×	×	
(ii)Anodes, X-ray grids, protection	×	×		×	×
(iii)Interruptors and contacts	×	×	×	×	
(iv)Nozzles, heat shields	×	×		×	×
(v)Field ion microscope	×	×	×	×	
(vi)Laboratory equipment; high-temperature structures	×	×		×	

3.8.1 Tungsten in lamp industry

Since the beginning of the 20th century, tungsten has been illuminating the world. In the electrical industries, tungsten is widely used as a filament in incandescent lamps, as electrodes for discharge tubes. The use of tungsten filaments in light bulbs is widespread, particularly in domestic lighting. Tungsten is used as bulb filaments because of its high melting temperature, high stiffness and excellent creep resistance at elevated temperatures. As at 2008,

about 4% of the annual tungsten production is consumed by the lighting industry, which constitutes about 15% [23] of the global electric power produced worldwide. Tungsten is used in the form of wires and coils in the incandescent lamps. It is also used as electrode in both low and high pressure discharge lamps.

3.8.2 Tungsten in steel industry

When added to steel, tungsten forms tungsten carbides or complex carbides with other carbide forming elements, such as chromium, molybdenum and vanadium [23]. Good wear resistance is the most important property of tool steels. Tungsten, next to vanadium in the periodic table is the most effective carbide forming element for increasing wear resistance. In addition, tungsten significantly increase the hardness and strength of steel. This leads to improved yield and tensile strengths without adversely affecting the ductility and fracture toughness of steel.

3.8.3 Tungsten in X-ray tubes

Tungsten is an excellent material when used as electron emitters. Although, other metals would yield higher emission rates, but the advantage of tungsten lies in its low vapour pressure even at high temperatures. X-ray tubes for medical use are equipped with a tungsten emitter coil. The rotating or static anode of X-ray tubes are made of tungsten too. The properties of tungsten

being explore in this applications are the low vapour pressure and high thermal conductivity. Tungsten electrodes are also used in the X-ray generators for security checks at the airports. Tungsten is used as important components in X-ray and radiation shields [4]. Typical examples of such shields are containers for radioactive materials and liquids, shielding construction parts in tomographic scanners, radiation therapy instruments, and containers and shielding for oil prospecting using radioactive sources.

3.8.4 High Temperature Applications

In the laboratory, many high temperature applications of tungsten are well known. For example, tungsten wires and tubes are used as heating elements in furnaces with a protective atmosphere, and in thermocouples for temperature measurement in excess of 2000 °C [4].

High temperature furnace parts (heating coils, radiation shields) which can withstand high temperatures of up to 2800 °C, are made of tungsten [3]. Tungsten nozzles with iridium inserts are used for the production of glass and ceramic wool for insulation applications. Seamless cylindrical tungsten crucibles are used for growing single crystals, required for semiconductors, LEDs, X-ray detectors, data storage or optical media [4].

3.8.5 Tungsten as lead substitute

Tungsten heavy metal composites are used as substitutes to lead. Tungsten shot and ammunition are environmental friendly alternatives to poisonous

lead for hunting and in military training. Tungsten heavy metal alloys are used for shielding radiation and as containers for radioactive substances. Tungsten compounds have been in use for the manufacture of non-lead radiation apparel. The advantage of non-lead radiation apparel is that they are approximately 20% [24] lighter than those made with lead.

3.8.6 Application of tungsten in the nuclear industry

Within the international thermonuclear experimental reactor (ITER), one of the most challenging components is the divertor, whose main function is to extract the power from the scrape-off layer of the plasma and to maintain plasma purity [25]. The main parts of the divertor, i.e. the inner and outer vertical target and the dome liner, comprise various materials which form a composite that is highly resistant to cyclic thermo-mechanical loads.

In designing the divertor for the ITER, almost all the divertor surface is covered with tungsten [26]. This application represents more than 100 tons in the case of the ITER construction [4]. During ITER operation, the tungsten target plates will have to be replaced between 5 to 8 times [4]. due to sputtering erosion. In this application, tungsten is expected to play two critical roles; (i) tungsten serves as a plasma facing armour or shield component material and (ii) tungsten serves as a structural material. An armour material needs to possess high cracking resistance under extreme thermal conditions whereas a structural material has to be ductile within the range of operation temperatures. And of course, in addition to these requirements, the material

need to be stable under high neutron irradiation.

In terms of neutron sensitivity associated with the analysis of engineering systems, tungsten is a key structural material for shielding fast breeder reactors and critical assemblies of fissionable materials [27]. The thermal neutron capture cross-section of tungsten is large, Friesenhahn, *et al.* [28] reported magnitude of 18.3±0.5 barns as the cross-sections for the natural W while the W isotopes ^{182}W, ^{183}W, ^{184}W and ^{186}W have the following values 20.7±0.5, 10.0±0.3, 1. 7±0.1, 37.8±1.2 barns, respectively.

Tungsten being an element with high atomic number with massive nucleus, can act as a shield component due to its ability to block gamma rays which low atomic number elements such as carbon cannot contain. The massive nucleus of tungsten indicates higher number of protons which equal the number of electrons per atom. Tungsten is able to block the gamma radiation through the mechanisms of photoelectric absorption, Compton scattering and pair production [29]. All these processes lead to the partial or complete transfer of the gamma radiation energies to electrons while some are converted to heat. Hence, the gamma radiation suffer loss in energy when they interact with electrons and are therefore brought to a halt. The energy of the incident gamma radiation determine which of the processes above dominate. Photoelectric absorption and pair production dominate at low and higher energies of the incident gamma radiation, respectively.

Neutrons have zero net charge, and therefore cannot interact in matter by

means of the coulomb force, which dominates the energy loss mechanisms for charged particles and electrons. This make neutrons highly penetrating type of radiation. When a neutron does undergo interaction, it is with a nucleus of the absorbing material [29]. Since neutron and proton have nearly identical masses, a neutron scattered from low-Z elements with Z<10, can lose most of its kinetic energy. In collision with hydrogen proton, even the entire kinetic energy of incident neutron can be transferred to the proton after a collision if it is scattered at 180°. This is similar to the collision of a billiard balls with identical masses. In contrast, the collision of neutron with a heavy nucleus is similar to scenario of a ping pong ball bouncing off a bowling ball after impact. Due to large difference in masses, neutrons are elastically scattered from the nuclei of heavy materials.

The performance of glassy carbon and tungsten in radiation shield will be complementary in the C-W system. High-Z materials (e.g. W) are ineffective in blocking the neutron radiation, as neutrons are uncharged and can easily pass through dense materials. On the other hand, materials composed of low-Z elements such as carbon are able to block neutron radiation because they have higher probability of forming cross-sections that will interact with neutrons. However, the low density materials can emit gamma radiation when blocking neutrons. This implies that shielding neutron radiation is most effective with application of both low and high density materials. The low density carbon can block neutron radiation while the tungsten being a high density material can block the gamma radiation by inelastic scattering.

REFERENCES

[1] I. L. Shabalin, *Ultra-high temperature materials I: Carbon (graphene/graphite) and refractory metals*. Springer, Manchester, 2014.

[2] G. F. Nordberg, B. A. Fowler, and M. Nordberg, *Handbook on the toxicology of metals*. Academic press, London, 2014.

[3] G. Rieck, *Tungsten and its compounds*. Oxford, Pergamon Press, Ltd, London, 1967.

[4] E. Lassner and W. D. Schubert, *Tungsten: Properties, chemistry, technology of the element, alloys, and chemical compounds*. Kluwer Academic / Plenum Publishers, New York, 1999, pp. 1–447.

[5] D. Strominger, J. M. Hollander, and G. T. Seaborg, "Table of isotopes," *Reviews of Modern Physics*, vol. 30, no. 2, pp. 585–986, 1958.

[6] J. Taylor, M. Mack, and W. Parrish, "Evaluation of truncation methods for accurate centroid lattice parameter determination," *Acta Crystallographica*, vol. 17, no. 10, pp. 1229–1245, 1964.

[7] A. Kiss, "Thermoanalytical study of the composition of beta-tungsten," *Journal of thermal analysis and calorimetry*, vol. 54, no. 3, pp. 815–824, 1998.

[8] H. Spier and W. Wanmaker, "Philips res," *Rep*, vol. 13, pp. 149–157, 1958.

[9] E. Prince and A. Wilson, *International tables for x-ray crystallography, vol. c*, 1995.

[10] J. P. Wittenauer, T. Nieh, and J. Wadsworth, "Tungsten and its alloys," *Advanced materials & processes*, vol. 142, no. 3, pp. 28–37, 1992.

[11] D. B. Miracle, S. L. Donaldson, S. D. Henry, C. Moosbrugger, G. J. Anton, B. R. Sanders, N. Hrivnak, C. Terman, J. Kinson, K. Muldoon, *et al.*, *ASM handbook*. ASM international Materials Park, OH, 2001, vol. 21.

[12] R. Lowrie and A. Gonas, "Dynamic elastic properties of polycrystalline tungsten, 24–1800 c," *Journal of Applied Physics*, vol. 36, no. 7, pp. 2189–2192, 1965.

[13] R. M. German and E. Olevsky, "Strength predictions for bulk structures fabricated from nanoscale tungsten powders," *International Journal of Refractory Metals and Hard Materials*, vol. 23, no. 2, pp. 77–84, 2005.

[14] C. Pande, R. Masumura, and R. Armstrong, "Pile-up based hall-petch relation for nanoscale materials," *Nanostructured materials*, vol. 2, no. 3, pp. 323–331, 1993.

[15] C. Ren, Z. Z. Fang, M. Koopman, B. Butler, J. Paramore, and S. Middlemas, "Methods for improving ductility of tungsten-a review," *International Journal of refractory metals and hard materials*, vol. 75, pp. 170–183, 2018.

[16] N. Macmillan, "The theoretical strength of solids," *Journal of Materials Science*, vol. 7, no. 2, pp. 239–254, 1972.

[17] C. Y. Ho, R. W. Powell, and P. E. Liley, "Thermal conductivity of the elements," *Journal of Physical and Chemical Reference Data*, vol. 1, no. 2, pp. 279–421, 1972.

[18] K. J. Laidler, "The development of the arrhenius equation," *Journal of Chemical Education*, vol. 61, no. 6, p. 494, 1984.

[19] E. Koch Bienemann, L. Berg, and G. Czack, *Gmelin handbook of inorganic and organometallic chemistry*, 1989.

[20] R. Andelin, J. Knight, and M Kahn, "Diffusion of tungsten and rhenium tracers in tungsten," *Trans. Met. Soc. AIME*, vol. 233, no. LADC-5849, 1965.

[21] S. Robinson and O. Sherby, "Mechanical behavior of polycrystalline tungsten at elevated temperature," *Acta Metallurgica*, vol. 17, no. 2, pp. 109–125, 1969.

[22] R. Tertian and F. Claisse, *Principles of quantitative X-ray fluorescence analysis*. Heyden, 1982.

[23] T. Eizenhöfer and W. Lixin, "21st annual general meeting, xiamen: International tungsten industry association," 2008.

[24] M. Zuguchi, K. Chida, M. Taura, Y. Inaba, A. Ebata, and S. Yamada, "Usefulness of non-lead aprons in radiation protection for physicians performing interventional procedures," *Radiation protection dosimetry*, vol. 131, no. 4, pp. 531–534, 2008.

[25] V. Philipps, "Tungsten as material for plasma-facing components in fusion devices," *Journal of nuclear materials*, vol. 415, no. 1, S2–S9, 2011.

[26] T. Hirai, S. Panayotis, V. Barabash, C. Amzallag, F. Escourbiac, A. Durocher, M. Merola, J. Linke, T. Loewenhoff, and G. Pintsuk, "Use of tungsten material for the ITER divertor," *Nuclear Materials and Energy*, vol. 9, pp. 616–622, 2016.

[27] M. T. Pigni and L. C. Leal, "Evaluated 182,183,184,186 W neutron cross sections and covariances in the resolved resonance region," Oak Ridge National Lab.(ORNL), Oak Ridge, TN (United States), Tech. Rep., 2015.

[28] S. Friesenhahn, E. Haddad, F. Froehner, and W. Lopez, "The neutron capture cross section of the tungsten isotopes from 0.01 to 10 electron volts," *Nuclear Science and Engineering*, vol. 26, no. 4, pp. 487–499, 1966.

[29] G. F. Knoll, *Radiation detection and measurement*. John Wiley & Sons, 2010.

CHAPTER

FOUR

DIFFUSION IN SOLIDS AND PHASE GROWTH KINETICS

4.1 Introduction

Diffusion plays a very important role in diverse phenomena. It has influence in many processes including, the intermixing of gases and liquids, evaporation of fluids, doping of silicon substrates for making semiconductor chips, case-hardening of steel gears used in automobile transmissions and transport of thermal neutrons in the nuclear reactors [1]. Diffusion is the phenomenon of material transport by atomic motion [2]. It is a process which leads to an equalization of concentration. Diffusion is relatively fast in gases, slow in liquids and very slow in solid media [1]. Diffusion in solids is a fundamental process in the science of materials and engineering. It is an important topic in the field of solid-state physics, metallurgy, materials science and physical chemistry. Diffusion processes are important for many microstructural

changes that occur during preparation, processing, and heat treatment of materials [1]. Nucleation of new phases, phase transformations, precipitation dissolution of a second phase and the homogenisation of alloys, all rely on diffusion processes.

4.2 Diffusion in solids

The diffusion in solid materials occurs mostly at temperatures in excess of the room temperature. The atoms in solids are constantly vibrating about their mean positions in their lattice sites [3]. These vibrations increase with temperature. It is not possible to observe the movement of individual atoms in solids [3], but diffusion does occur. So, there exists relative motion of the atoms in solid diffusion. Diffusion in solids occurs by periodic jumping of atoms from one lattice site to another. There is a separation of time scales between the jump processes of atoms in-between neighbouring lattice sites [1] and these successive steps constitute diffusion.

4.3 Diffusion mechanism

The theory of atomic diffusion in crystalline solids is closely tied to the diffusion mechanisms. In solids, crystal lattice confines the positions and the movement of atoms. The mechanisms for atomic diffusion in crystalline solids are closely related to presence of defects [1]. Point defects such as vacancies and interstitials are the common defects in solids, and these often aid diffusion

in crystalline solids. In addition, grain boundaries is another type of defect in polycrystalline solids. This defect act as pathway for high diffusivity often referred to as short circuit diffusion, because the atomic motion along this defect is much higher compared to diffusion through the bulk. Diffusion in solids is largely aided by the following diffusion mechanisms.

4.3.1 Interstitial diffusion

An atom is said to diffuse by an interstitial mechanism when it hops from one interstitial site to the nearest neighbor interstitial sites without permanently dislodging any of the solvent atoms [3]. For an impurity atoms to be able to jump from one lattice site to another, these atoms need energy to break bonds with neighbors. This energy comes from the thermal energy of the atomic vibrations. The solute interstitial atoms are usually smaller in size compared to the host atoms as shown in Figure 4.1. The interstitial sites are empty voids in the lattice structure which are not meant to be occupied by the host atoms.

Interstitial solid solution is favoured between two materials with considerably large difference in their atomic radii. When the interstitial atoms diffuse from one site to another, such diffusion cause lattice distortion to the lattice structure of the host atoms. The atomic size of even very small interstitial atom are larger than the interstitial sites [2], and as result, their presence introduce lattice strains on the adjacent solvent atoms. In BCC crystal structure for example, the atomic radius r of an interstitial solute which would not cause lattice strain on the host atoms with atomic radius R must be $r = 0.155R$

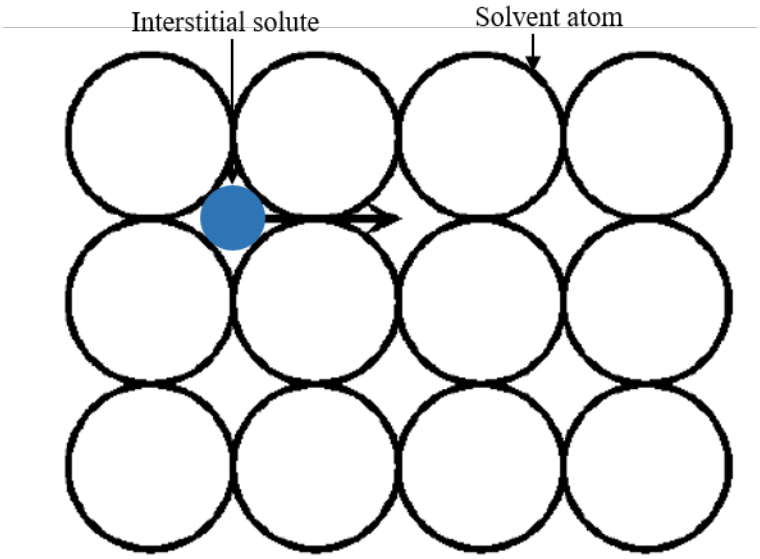

Figure 4.1: Interstitial solute atom in a crystal structure [4]

[2]. This gives $r = 0.02$ nm for tungsten as host atoms, r value for interstitial carbon is 0.07 nm. Generally, the degree of lattice distortion increase substantially with large numbers of interstitial solutes, and the effect can cause considerable change in properties of the host material. Atoms such as H, C, N and O characterized by small atomic radii usually diffuse through transition metals via interstitial mechanism [5], [6]. Carbides of tungsten and iron are formed by the interstitial diffusion of carbon in these transition metals.

4.3.2 Vacancy diffusion

Vacancy is a normally occupied lattice site from which an atom is missing [2]. There are vacancies in the crystal structures of all real crystalline solids. In fact, it is impossible to create a material that is free of vacancies [2]. These

unoccupied lattice sites are important for both self-diffusion and impurity solute diffusion. The host atom or substitutional solute atoms can diffuse by moving into the neighbouring vacant sites. The movement of such atom is in the direction opposite to that vacancy [3] and it constitutes vacancy diffusion. In this diffusion mechanism, vacancies can move relatively fast, but

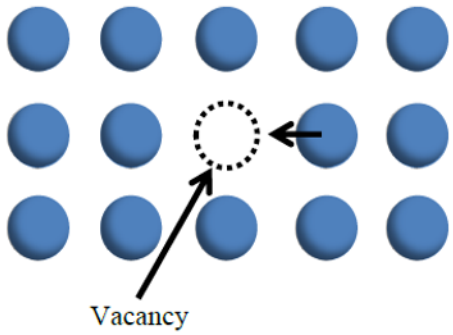

Figure 4.2: Vacancy diffusion mechanism [4]

the movement of self-atoms or the substitutional solute is normally influenced by the existence of a neighbouring vacant site with which it can exchange position. The substitutional solute atom and the host atoms have nearly equal atomic radii.

4.3.3 Grain boundary diffusion

Poly-crystalline solids are characterized by large amount of grain boundaries in their structures, diffusion takes place along these grain boundaries. The grain boundaries in poly-crystalline solids act as diffusion paths with enhanced atomic mobility [1]. The atomic arrangements at grain boundaries are highly flawed and therefore provide an easy diffusion paths to atomic

movement (Figure 4.3). Grain boundary diffusion is generally faster compared

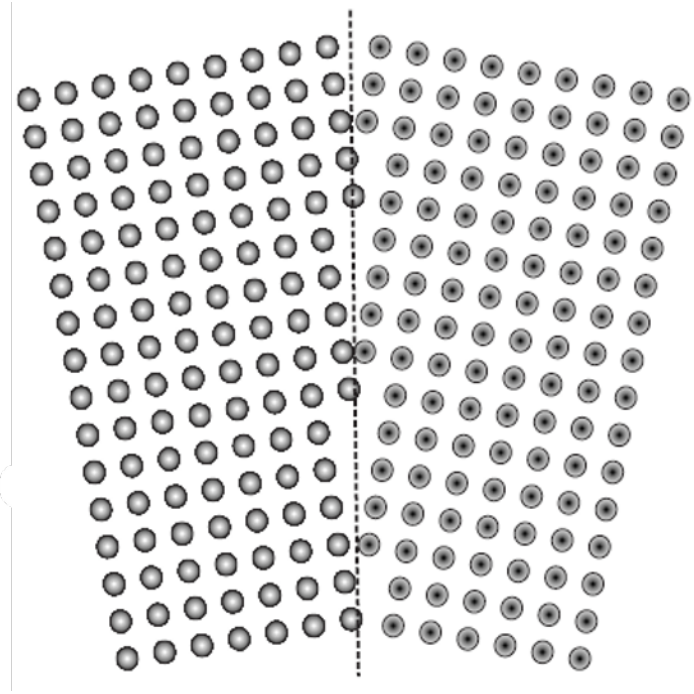

Figure 4.3: Dislocation model of a grain boundary [7]

to diffusion through the bulk material, also known as lattice diffusion. Grain boundary diffusion dominants at lower temperatures in solids with a given microstructure.

At relatively low temperatures, grain boundary diffusion mechanism is characterized by smaller activation energy compared to lattice diffusion [3]. At higher temperatures, diffusion through point defects in a solid increase, leading to increased bulk diffusion which surpasses the grain boundary diffusion.

In metallic thin films grown by physical vapour deposition techniques such as evaporation and sputtering; and chemical vapour deposition, their

structure is normally different from the bulk samples. Such films are characterized by small grain size and polycrystalline structures, with large number of grain boundaries [8]. The tendency for quick diffusion in thin films at lower temperatures is very high compared to the bulk samples due to the presence of large number of grain boundaries.

4.4 Theory of diffusion

Atomic diffusion takes place in solid media through the mechanisms described above in Section 4.2. The presence of a concentration gradient is an important factor which influences diffusion in solids. To have a better understanding of a diffusion process, it is important to know how fast the atoms or molecules migrate from the region of high concentration to that of lower concentration. The parameter which tells how fast diffusion propagates is the diffusion flux. It is the number of atoms (or amount of substance) diffusing through a unit area per unit time.

4.4.1 Fick's laws of diffusion

Consider a one-dimensional plane of reference and along the x- direction, the diffusion flux J_i is directly proportional to the concentration gradient $\frac{dC_i}{dx}$ for a number of atoms of kind i. This is the Fick's first law of diffusion and it is expressed mathematically as [9]:

$$J_i = \frac{m}{At} = -D_i \frac{dC_i}{dx} \tag{4.1}$$

where m is the mass of substance, A is cross-sectional area, t is time and D_i is the proportionality constant known as the diffusion coefficient. It measures the ease with which atoms migrate through a medium. Diffusion of atoms occur in solids in the presence of a concentration gradient $\frac{dC_i}{dx}$, where C_i represents the concentration usually in atoms/cm^3 and x is the distance along which the atoms migrate in one dimension. The negative sign emphasizes that diffusion occurs down the concentration gradient. Equation 4.1 is known as the steady state diffusion since it is time independent. The time dependence of the diffusion law is given by;

$$\frac{dC_i}{dt} = -\frac{dJ_i}{dx} = -\frac{d}{dx}\left(-D_i\frac{dC_i}{dx}\right) \tag{4.2}$$

If it is assumed that the diffusion coefficient does not dependent on the concentration, the equation above simplifies to this form;

$$\frac{dC_i}{dt} = D_i\frac{d^2C_i}{dx^2} \tag{4.3}$$

The temperature dependent diffusion coefficient D_i is given by an Arrhenius equation [3], [10]:

$$D_i = D_o exp(-Q/k_BT) \tag{4.4}$$

where D_o is a temperature independent pre-exponential factor, Q is the activation energy, k_B is the Boltzmann constant and T is the absolute temperature.

4.5 Random walk theory of diffusion

Random walk is an idealization of a path covered by a succession of random steps [11]. It serves as a model for different stochastic processes. Many individual displacements or jumps of the diffusing atoms, constitute diffusion in solids. From the microscopic point of view, diffusion in solids occurs by the random movement of atoms. As mentioned in Subsection 4.3.1, interstitial diffusion in solids occurs by atomic hopping from one lattice to another. The elementary diffusion jump of an atom in a lattice is very fast and has a time duration of approximately 1×10^{-13} s [1]. Jump duration is very rapid compared to the mean residence time of an atom in the lattice site.

The atomic jump processes can be described by a number of quantities such as the jump rates and jump distances. Atomic jump processes are promoted by thermal activation. The rate (number of jumps/sec) of an individual atomic jumps (Γ) is described by an Arrhenius law, given by [1], [12]:

$$\Gamma = \nu^o exp\left(-\frac{\Delta G}{k_B T}\right) \tag{4.5}$$

where ν^o denotes an attempt frequency of the order of the Debye frequency of the lattice. Typical values of Debye frequency lie between 1×10^{12} and 1×10^{13} s^{-1} [1]. ΔG is Gibbs free energy of activation, k_B is Boltzmann constant and T is absolute temperature.

The theory of random walk involves a back and forth process between the diffusion coefficient given by the Fick's laws of diffusion. A simplified

model of the random walk theory is given as follows. Consider a dimensional diffusion of interstitial solutes in a simple cubic crystal structure. In Figure 4.4, assume that the diffusing solute atoms migrate by hopping from one interstitial site to another with a jump length λ. Imagine a concentration gradient along the x-direction with the following parameters are defined as follows; Γ is the jump rate from one plane to the neigbouring one, n_1 is the number of interstitial solute per unit area in plane 1, and n_2 is number of interstitial solutes per unit area in plane 2. The zigzag jumps occur with the same jump

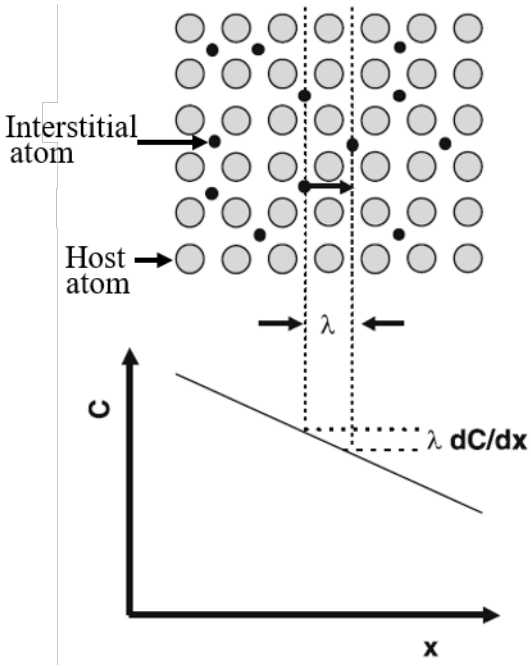

Figure 4.4: One dimensional diffusing interstitial atoms in a lattice. Adapted from [1]

rate and the net diffusion flux J from plane 1 to plane 2 is given by [1]:

$$J = \Gamma n_1 - \Gamma n_2 \tag{4.6}$$

where n_1 and n_2 are related to the volume concentrations C_1 and C_2 by [1]:

$$n_1 = \lambda C_1; n_2 = \lambda C_2 \tag{4.7}$$

From a Taylor expansion of the concentration-distance function [1], keeping only the first term in Figure 4.4 yields:

$$C_1 - C_2 = -\lambda \frac{dC}{dx} \tag{4.8}$$

Substituting Equations 4.8 and 4.7 into Equation 4.6, yields:

$$J = -\lambda^2 \Gamma \frac{dC}{dx} \tag{4.9}$$

The comparison of Equations 4.9 and 4.1 shows that the diffusion coefficient D is given by:

$$D = \lambda^2 \Gamma \tag{4.10}$$

Considering a simple cubic lattice, the atomic jump rate to one of its six nearest-neighbour interstices is related to its total jump rate through $\Gamma_{tot} = 6\Gamma$. This yields:

$$D = \frac{1}{6} \lambda^2 \Gamma_{tot} \tag{4.11}$$

Equation 4.11 shows that the product of the jump rate (per second) and square of the jump distance (square metre) essentially constitute the diffusion coefficient.

4.6 Phase growth kinetics

Equation 4.1 is not applicable in experimental diffusion study in the solid state systems, because the concentration of solute atoms at any point in the material changes with time and distance [13]. The concentration gradient in the growing phase between the adjacent interfaces is not known [14]. The unknown dependency of $\frac{dC_i}{dx}$ on temperature renders Equation 4.1 ineffective for determining the activation energy. To circumvent this problem, a much more transparent representation of the growth mechanism is obtained through the application of Nernst-Einstein relation [13]–[16]:

$$J_i = -C_i \frac{D_i^{ne}}{k_B T} \frac{d\mu_i}{dx} \tag{4.12}$$

where the concentration gradient is replaced with the gradient in chemical potential $\frac{d\mu_i}{dx}$, that is, the driving force of the solid phase reaction. C_i is the concentration of atoms of kind i in the growing phase.

4.6.1 Growth of single phase

If two substances react with one another to form one product phase which is separated from the reactants, then a heterogeneous solid state reaction is said to have occurred [16]. The appropriate expression describing a single product formation from the reaction between two elemental constituents A and B is described by the transformation expression: [14], [16]:

$$mA + nB \rightarrow A_m B_n \tag{4.13}$$

where A_mB_n represents the phase grown between two reservoirs of atoms of kinds A and B, as shown in Figure 4.5. If the growth is governed by a diffusion controlled mechanism, the growth rate $\frac{dx}{dt}$ of A_mB_n can be deduced as follows.

The increase in thickness of the growing phase is related to the fluxes j_A

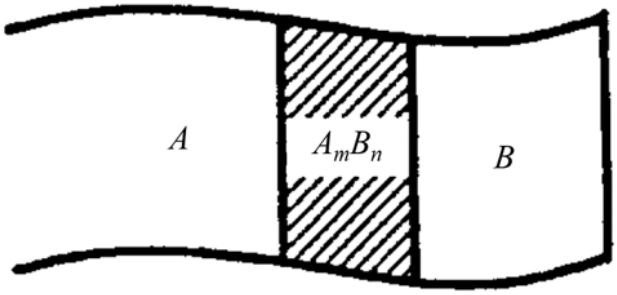

Figure 4.5: Schematic of the phase growth A_mB_n between the substrate atoms A and deposited film atoms B, upon annealing

and j_B of the individual atoms in close contact at the reaction interface where the compound is formed. For every mole of A atoms, $1/m$ moles of A_mB_n is formed, and the growth rate $\frac{dx_A}{dt}$ due to an influx j_A (in units of mol.$cm^{-2}s^{-1}$) can thus be written as: [16]:

$$\frac{dx_A}{dt} = \frac{|j_A|}{m} V_{A_mB_n} \tag{4.14}$$

where $V_{A_mB_n}$ is the volume of one mole of A_mB_n expressed in cm^3/mol. In a similar way the growth rate of A_mB_n due to an influx j_B of atoms B can be expressed as [16]:

$$\frac{dx_B}{dt} = \frac{|j_B|}{n} V_{A_mB_n} \tag{4.15}$$

The sum of Equations 4.14 and 4.15 then gives the total growth rate as:

$$\frac{dx}{dt} = \left(\frac{|j_A|}{m} + \frac{|j_B|}{n} \right) V_{A_m B_n} \tag{4.16}$$

The individual particle fluxes j_i can be taken directly from the Nernst-Einstein Equation 4.12, in which the atomic concentration C_i is given in units of mol./cm^3. When a local thermodynamic equilibrium is maintained, the element specific chemical potentials across the growing layer can be taken as [16];

$$\Delta\mu_A = \frac{\Delta G_{A_m B_n}}{m} \tag{4.17}$$

where $\Delta G_{A_m B_n}$ is the change in Gibbs free energy, in units of (eV/atom) for the formation of one molecule of $A_m B_n$.

And similarly,

$$\Delta\mu_B = \frac{\Delta G_{A_m B_n}}{n} \tag{4.18}$$

Using Equations 4.12, 4.17 and 4.18 in Equation 4.16 and noting that $C_i = N_i / V_{A_m B_n}$ [16], rearranging the expressions yields [14], [17], [18]:

$$\frac{dx}{dt} = \left(\frac{D_A}{m} + \frac{D_B}{n} \right) \frac{\Delta G_{A_m B_n}}{k_B T} \frac{1}{x} \tag{4.19}$$

This growth rate can be written in terms of the interdiffusion coefficient, thus [14], [16];

$$D = D_A N_B + D_B N_A \tag{4.20}$$

where $N_A = m/(m+n)$ and $N_B = n/(m+n)$ are the fractional concentrations

of A and B in the compound A_mB_n. Applying Equation 4.20 in Equation 4.19 yields [17], [18];

$$\frac{dx}{dt} = \frac{(m+n)^2}{mn}\frac{\Delta H_{A_mB_n}}{k_BT}\frac{D}{x} \tag{4.21}$$

where $\Delta G_{A_mB_n}$ has been approximated by the heat of formation $\Delta H_{A_mB_n}$ since ΔS can be considered infinitesimally small for solid phase transitions at lower temperatures. The temperature dependent interdiffusion coefficient D is related to the pre-exponential coefficient D_o and the activation energy via Equation 4.4.

For the second phase growth of compound A_mB_n from the reaction of A_pB_q with B, the situation is treated in slightly different way. Consider the following general reaction equation for subsequent phase formation [14], [17]:

$$mA_pB_q + (pn - mq)B \rightarrow pA_mB_n \tag{4.22}$$

Similar to the procedure previously adopted in the case of single phase growth above, the chemical potentials can be expressed as [14];

$$\Delta\mu_A = \frac{m+n}{m}\Delta H^R_{A_mB_n} \tag{4.23}$$

$$\Delta\mu_B = \frac{m+n}{n}\Delta H^R_{A_mB_n} \tag{4.24}$$

where $\Delta H^R_{A_mB_n}$ is the reaction enthalpy of the system. From the general reaction in Equation 4.22, the species specific growth rates are expressed as [14]:

$$\frac{dx_A}{dt} = \left(\frac{pn}{pn - mq}\frac{|j_A|}{m}\right) V_{A_mB_n} \tag{4.25}$$

$$\frac{dx_B}{dt} = \left(\frac{pn}{pn - mq}\frac{|j_B|}{n}\right) V_{A_mB_n} \tag{4.26}$$

Adding Equations 4.25 and 4.26 and applying Equations 4.12 and 4.20 yields the total growth rate as [14], [17]:

$$\frac{dx}{dt} = \frac{pn}{pn - mq}\frac{(m+n)^2}{mn}\frac{\Delta H_{A_mB_n}}{k_BT}\frac{D}{x} \tag{4.27}$$

Equation 4.27 is the growth of a compound A_mB_n from the reaction between element B and compound A_pB_q. If $q = 0$, it implies that Equation 4.22 reduces to Equation 4.13 and hence, Equation 4.27 also reduces to Equation 4.21. This shows that Equation 4.27 represents the general equation of the growth rate.

4.6.2 Growth kinetics due to annealing

During an isothermal annealing, the sample is maintained at a constant temperature for a period of time while the thin film reacts at the interface. The integral of Equation 4.27 can used to demonstrates how the thickness of the growing compound evolves with annealing duration [14], [17].

$$\int_0^x x\,dx = \frac{pn}{pn - mq}\frac{(m+n)^2}{mn}\frac{\Delta H_{A_mB_n}}{k_BT}D\int_0^t dt \tag{4.28}$$

$$x^2 = 2\frac{pn}{pn - mq}\frac{(m+n)^2}{mn}\frac{\Delta H_{A_mB_n}}{k_BT}Dt \tag{4.29}$$

$$x = k \cdot t^{1/2} \tag{4.30}$$

$$k = \left(2\frac{pn}{pn - mq}\frac{(m+n)^2}{mn}\frac{\Delta H_{A_mB_n}}{k_B T}D\right)^2 \tag{4.31}$$

k is the parabolic reaction constant [17]. Equation 4.30 shows that the thickness of a phase grown in a diffusion controlled mechanism evolves quadratically as a function of annealing duration. As such, the diffusion controlled growth is often referred to as parabolic growth. The plot the experimentally obtained thickness as a function of the square root of the annealing time, provides an easy way to check whether the growth can be classified as diffusion controlled or not.

4.7 Evaluation of diffusion parameters

When the phase formation is favoured by the parabolic growth, the activation energy Q and pre-exponential factor D_o governing the growth rates can be evaluated through a number of methods. Popular among these methods are the isothermal annealing campaigns coupled with construction of an Arrhenius [10] plot, and ramped annealing, followed by Kissinger analysis [17], [19]. The Arrhenius method was used in this research work. With this method, the activation energy can be evaluated from the Arrhenius plots, having estimated the reaction constant in Equation 4.30 from the parabolic growth for different isothermal annealing temperatures. The slope of the linear

fit through the logarithm of the reaction constant versus inverse annealing temperature is equivalent to the activation energy, while intercept is a means for estimating the pre-exponential factor.

REFERENCES

[1] H. Mehrer, *Diffusion in solids: Fundamentals, methods, materials, diffusion-controlled processes*. Springer Science & Business Media, Dresden, Germany, 2007.

[2] W. D. Callister and D. G. Rethwisch, *Materials science and engineering: An introduction*. John wiley & sons, New York, 2007.

[3] P. Shewmon, *Diffusion in solids*. Springer, Switzerland, 2016.

[4] K. A. Jackson, *Kinetic processes: Crystal growth, diffusion, and phase transformations in materials*. John Wiley & Sons, New York, 2006.

[5] R. Abbaschian and R. E. Reed-Hill, *Physical metallurgy principles*. Cengage Learning, USA, 2008.

[6] P. Kofstad, "Defects and transport properties of metal oxides," *Oxidation of metals*, vol. 44, no. 1-2, pp. 3–27, 1995.

[7] G. S. Was, *Fundamentals of radiation materials science: Metals and alloys*. Springer, New York, 2016.

[8] M. Ohring, *Materials science of thin films*. Elsevier, London, 2001.

[9] J. Crank, *The mathematics of diffusion*. Oxford university press, London, 1979.

[10] K. J. Laidler, "The development of the Arrhenius equation," *Journal of Chemical Education*, vol. 61, no. 6, pp. 494–508, 1984.

[11] R. Wojnar, "Random walk, diffusion and wave equation.," *Acta Physica Polonica B*, vol. 44, no. 5, pp. 1067–1083, 2013.

[12] A. S. Nowick, *Diffusion in solids: Recent developments*. Elsevier, London, 2012.

[13] F. d'Heurle and P Gas, "Kinetics of formation of silicides: A review," *Journal of materials research*, vol. 1, no. 1, pp. 205–221, 1986.

[14] J. Demeulemeester, "PhD thesis, Universiteit Leuven, Belgium," 2010.

[15] A. Einstein, "On the motion of small particles suspended in liquids at rest required by the molecular-kinetic theory of heat," *Annalen der physik*, vol. 17, pp. 549–560, 1905.

[16] H. Schmalzried, *Solid state reactions*. Verlag chemie, Weinheim-Germany, 1974.

[17] C. Theron, J. Lombaard, and R Pretorius, "Real-time RBS of solid-state reaction in thin films," *Nuclear Instruments and Methods in Physics Research Section B: Beam Interactions with Materials and Atoms*, vol. 161, pp. 48–55, 2000.

[18] H. Schmalzried, "Solid-state reactions," in *Treatise on Solid State Chemistry: Volume 4 Reactivity of Solids*, N. B. Hannay, Ed. Boston, MA: Springer US, 1976, pp. 233–279.

[19] H. E. Kissinger, "Reaction kinetics in differential thermal analysis," *Analytical chemistry*, vol. 29, no. 11, pp. 1702–1706, 1957.

CHAPTER

FIVE

THE THERMODYNAMICS OF CARBON-TUNGSTEN INTERACTION

5.1 Introduction

The interaction between carbon and metals is of great scientific and technological importance, as it has a broad range of implications in the field of material physics [1]. The transition metals (V, Nb, Ta, Cr, Mo, W) in groups IV-VI react with carbon to form carbides which are strongly nonstoichiometric interstitial compounds [2]. The characteristic feature of the structures of these compounds is the presence of the face centered cubic (FCC) or hexagonal close packed (HCP) metallic lattice. Carbon atoms are located in the center of octahedral or trigonal interstitials of the metallic lattice [3] for the BCC structure. Thus, the crystal structure of the metals changes upon carbide formation. Metals with the body centred cubic (BCC) structure such as tungsten, form carbides with the cubic (BCC and FCC) or hexagonal metallic sublattices.

The polymorphic transformation of crystal structure of these metals upon formation of carbides suggests a strong metal - carbon interaction.

5.2 Solubility of carbon in tungsten

The homogeneous mixture of two or more kinds of atoms in the solid state, is known as solid solution [4]. These solid solutions are usually crystalline materials. Solid solutions occur in either of two distinct types; these are substitutional solid solution and the interstitial solid solutions. In the first case, a direct substitution of one kind of atom for another takes place such that the solute atoms enter the crystal to take the lattice sites originally occupied by host atoms. In a substitutional solution, there exists a negligible atomic size difference between the foreign atoms and the host atoms. In the case of interstitial solid solution, there is considerable difference in the atomic size of the solute and the solvent atoms. The difference between the two solid solutions is pictorially depicted in Figure 5.1.

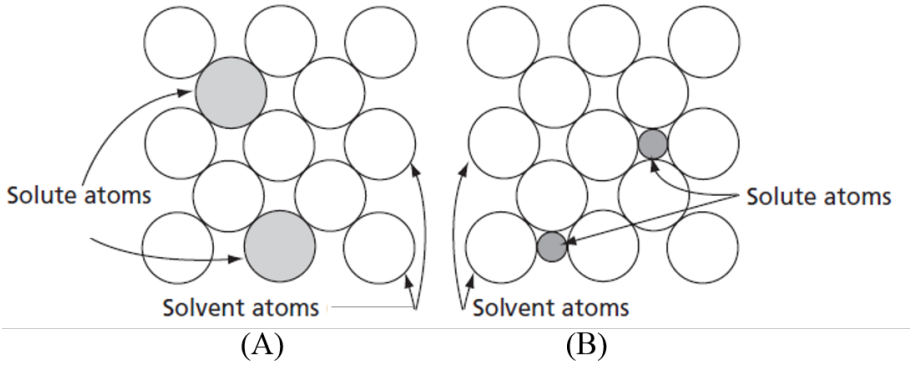

Figure 5.1: Two basic types of solid solutions. (A) Substitutional solid solution (B) Interstitial solid solution. Adapted from [4]

The conditions that determine the solubility in both substitutional and interstitial solutions have been studied in details by Hume-Rothery [4], [5]. According to the Hume-Rothery rules, an extensive interstitial solid solution forms if only the interstitial atom has an apparent diameter 0.59 smaller than that of the host atoms [4]. The four most significant interstitial atoms are the carbon, nitrogen, oxygen and hydrogen [4], [6], all of which are characterized by small atomic sizes.

The solubility of carbon in tungsten occurs by the interstitial mode [4], [5], [7]. The degree to which interstitial atoms dissolve in transition metals depends on the metal and the solute atom in question, but the solubility limit is usually small. One of the earlier measurements of the carbon solid solubility was done by Goldschmidt and Brand [8]. They reported that, carbon has a small solubility limit in tungsten. The maximum solubility limit of 0.3 at.% C is attained at the eutectic temperature of 2400 °C. This value decreased rapidly to 0.05 at.% C at 2000 °C and to trace amounts at lower temperatures. In the temperature range of 1400 - 2600 °C, the solubility of carbon in tungsten is expressed by [9]:

$$\ln x = 4.67 - 15000/T \tag{5.1}$$

where x is carbon concentration (at.% C) and T is absolute temperature. In the W-C phase diagram (Figure 5.2), the maximum solubility of C in W occurred at temperature of 2988 K, with solubility limit of approximately 1.8 at.% C. Although, these figures have some variations but the common trend

is that, interstitial solubility of carbon in tungsten generally increase with temperature.

5.3 W-C phase diagram

The refractory compounds formed by the interaction of tungsten and carbon are represented in the tungsten-carbon phase diagram. The phase diagram for the W-C was measured several times [10]. The early schematic phase diagram for the W-C was proposed by Willey and Margolin [11]. It was based mainly on the work of Rudy in 1969 [12]. The W-C phase diagram had witnessed various modifications and adjustments over the years. The most recent work on the W-C phase diagram was reported by Kurlov and Gusev [13], shown in Figure 5.2.

In the W-C phase diagram, in addition to tungsten (W) and carbon (C), there are two single phases; namely ditungsten carbide W_2C and tungsten monocarbide WC [13], [14]. Each phase has a number of structural modifications, which are stable in different temperature and composition ranges. The ditungsten carbide W_2C has three modifications β, β' and β'' while the tungsten monocarbide WC has two modifications denoted by δ and γ [12], [13]. The γ modification exists only at elevated temperature.

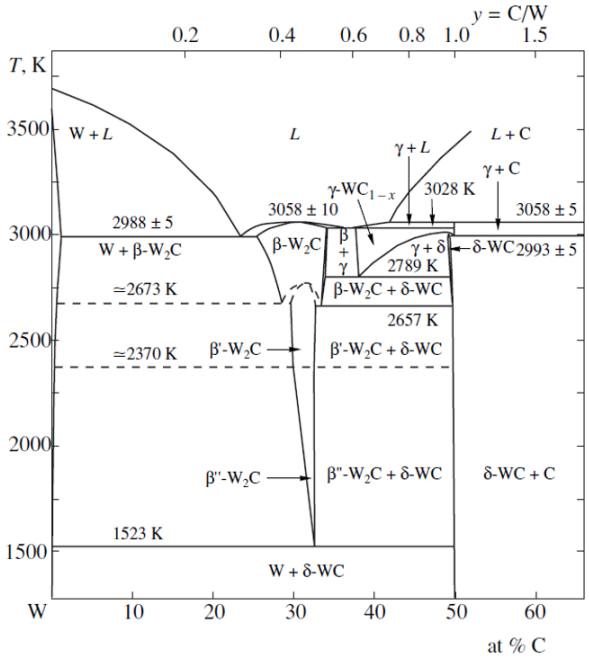

Figure 5.2: The W-C phase diagram [13]

5.3.1 Phases on the W-C phase diagram

5.3.1.1 W_2C phase

The ditungsten carbide W_2C, was initially believed to be stable from room temperature up to its melting temperature [13]. However, it was later shown that, it does not exist in thermodynamic equilibrium, below 1523 K [13]. It undergoes eutectoid decomposition to W and δ-WC at 1523 K. According to Figure 5.2, W_2C exists in three polymorphs; the low-temperature polymorph (β''), the intermediate (β'), and high-temperature polymorph (β). In all the three polymorphs, the tungsten atoms form an HCP sublattice in which half of the octahedral interstices are occupied by carbon atoms [13]. W_2C is a nonstoichiometric compound with varying carbon compositions (Table 5.1).

Table 5.1: Structural data for phases existing in the W-C phase diagram above 1300 K [13]

Phase	Composition (at. % C)	Lattice constants (nm)	Crystal type
W	0-1.0	a=0.3165	BCC
β''-W_2C	29.5-32.5	a = 0.2985, c = 0.4717	HCP
β'-W_2C	29.5-33.0	a = 0.2985, c = 0.6009	HCP
β-W_2C	25.5-34.0	a = 0.3002, c = 0.4750	HCP
γ-WC_{1-x}	37.0-39.5	a = 0.4266	FCC
δ-WC	50	a = 0.2906, c = 0.2837	HCP
C (graphite)	100	a = 0.142, c = 0.339	HCP

5.3.1.2 WC_{1-x} phase

The carbide, WC_{1-x} is a nonstoichiometric compound in the composition range of $WC_{0.58}$ to $WC_{0.65}$ at temperatures above 2789 K [12]. It was believed to be a high temperature modification of WC [3], but its carbon content is quite different from that of the stoichiometric WC. It also has a distinguishable feature of possessing an FCC structure. At a temperature of approximately 2789 K, WC_{1-x} decompose eutectoidally to β-W_2C and δ-WC.

5.3.1.3 WC phase

The tungsten monocarbide WC with the hexagonal structure is designated as δ-WC or simply WC [3]. Unlike the β-W_2C and WC_{1-x}, WC has a very negligibly small homogeneity region or does not have it at all [3], [12]. Under normal conditions, the hexagonal tungsten carbide WC is a stoichiometric compound. Tungsten and carbon atoms in WC form simple hexagonal sublattices, in which C atoms are located in the centres of trigonal prismatic interstitials of

the tungsten sublattice [3]. Table 5.1 presents the summarized data on the crystal structures of the phases in the W-C phase diagram. It can be easily observed in Figure 5.1 and Table 5.1 that the carbide WC is a stoichiometric compound with the highest carbon composition of 50 at.% C.

5.4 Thermodynamics of W_2C and WC formation

According to W-C phase diagram in Figure 5.2, tungsten is in thermodynamic equilibrium with WC at low temperatures (below 1523 K) and with W_2C at high temperatures (between 1523 K and 3058 K). The eutectoid reaction

$$W_2C \rightarrow W + WC \tag{5.2}$$

occurs at a temperature of 1523 K. The free energy of formation of WC (ΔG^o) from the reaction

$$W + C \rightarrow WC \tag{5.3}$$

can be expressed by [15]:

$$\Delta G^o = -RT \ln K = -RT \ln \frac{a_{WC}}{a_W a_C} \tag{5.4}$$

where R is the universal gas constant, T is absolute temperature, a is activity of carbon. But W and WC are essentially pure substances, the mole fraction of C dissolved in W at 1600 K is less than $\times 10^{-4}$ [15]. Hence, $a_{WC} = a_W = 1$. This implies that Equation 5.4 reduces to Equation 5.5 [15]:

$$\Delta G^o = RT \ln a_C = \Delta G_f^o(WC) \qquad (T < 1523K) \tag{5.5}$$

In similar manner, the free energy of formation of W_2C can be determined from the reaction below [15]:

$$2W + C \rightarrow W_2C \tag{5.6}$$

Assuming that W_2C exists as a nearly stoichiometric compound between the temperature 1523 to 1660 K, it implies that its free energy of formation can be expressed as [15]:

$$\Delta G^o = RT \ln a_C = \Delta G_f^o(W_2C) \qquad (T > 1523K) \tag{5.7}$$

Gupta and Seigle [15] reported that the free energy of formation and enthalpy in the unit of (J/mol.) for the two carbide phases from their experimental campaigns on the thermodynamic properties of carbon in solid tungsten, have the following relations for the WC phase [15]:

$$\begin{aligned} \Delta G_f^o(WC) &= -42300 \pm 400 + 4.98/T \\ \Delta H_f^o(WC) &= -42300 \pm 800 \end{aligned} \tag{5.8}$$

where T, the absolute temperature has the range 298 K < T < 1523 K.

For the W_2C phase, the free energy and enthalpy of formation are [15]:

$$\begin{aligned} \Delta G_f^o(W_2C) &= -30500 \pm 400 - 2.34T \\ \Delta H_f^o(W_2C) &= -30500 \pm 1300 \end{aligned} \tag{5.9}$$

where T has the range 1523 K < T < 1600 K.

The accuracy of the calculated thermodynamic properties of C in W depends on the accuracy of the solubility data as well as the reliability of the

carbon activity measurements [15]. The values of these thermodynamic data are different from other experimental sources. For example, these researchers [16]–[19] have reported varying data for enthalpy and free energy of formation for WC and W_2C. At room temperature (298 K), different values of the enthalpy of formation for W_2C were obtained as follows; $\Delta H_f^o(W_2C) = -26400 \pm 2500$ J/mol. [16]. $\Delta H_f^o(W_2C) = -13400$ J/mol. [17]. The following data exist for enthalpy of formation of WC at room temperature (298 K). $\Delta H_f^o(WC) = -44400 \pm 800$ J/mol [15], $\Delta H_f^o(WC) = -41200 \pm 500$ J/mol [17].

For the change in free energy of formation, these data exist for WC and W_2C at these range of temperatures.

$\Delta G_f^o(WC) = -52330 + 14.06$ J/mol. (1173$<$ T $<$1573 K) [18].

$\Delta G_f^o(WC) = -38000 - 8.4T$ J/mol. (500 to 1200 K) [19].

$\Delta G_f^o(W_2C) = -26000 - 14T$ J/mol. (1573 to 2500 K) [19].

One of the recent investigations involving the evaluation of thermodynamic data of tungsten carbides was done by Gronvold *et al.* [17]. They carried out a detailed study which covered a wide range of temperature between 10 to 2000 K. The values of enthalpy, entropy and Gibbs energy of formation of W_2C and WC tabulated in Table 5.2.

The difference in values of the thermodynamic data can be linked to difference experimental methods, range of temperature of investigation in addition to varying degree in sources of errors. The general trend in all these

Table 5.2: Enthalpy, entropy and Gibbs energy of formation of W_2C and WC [17]

T (K)	$M(W_2C_{0.833}) = 377.71$ g mol^{-1}			$M(WC) = 195.86$ g mol^{-1}		
	$\Delta_f H^\ominus$ (kJ mol^{-1})	$\Delta_f S^\ominus$ (J K^{-1} mol^{-1})	$\Delta_f G^\ominus$ (kJ mol^{-1})	$\Delta_f H^\ominus$ (kJ mol^{-1})	$\Delta_f S^\ominus$ (J K^{-1} mol^{-1})	$\Delta_f G^\ominus$ (kJ mol^{-1})
298.15	−13.41	5.75	−15.12	−40.40	−6.28	−38.53
300	−13.40	5.77	−15.13	−40.39	−6.26	−38.52
400	−12.96	7.02	−15.77	−40.00	−5.13	−37.95
500	−12.38	8.31	−16.53	−39.62	−4.28	−37.48
600	−11.80	9.37	−17.42	−39.34	−3.76	−37.08
700	−11.27	10.19	−18.40	−39.13	−3.44	−36.72
800	−10.78	10.85	−19.45	−38.95	−3.21	−36.39
900	−10.31	11.40	−20.57	−38.79	−3.02	−36.08
1000	−9.86	11.87	−21.73	−38.64	−2.85	−35.79
1100	−9.46	12.24	−22.94	−38.49	−2.71	−35.51
1200	−9.13	12.54	−24.28	−38.34	−2.58	−35.24
1300	−8.86	12.75	−25.44	−38.20	−2.46	−34.99
1400	−8.64	12.92	−26.72	−38.05	−2.36	−34.75
1500	−8.46	13.04	−28.02	−37.90	−2.25	−34.52
1550	−8.38	13.10	−28.68	−37.81	−2.20	−34.41
1600	−8.30	13.14	−29.33	−37.73	−2.14	−34.30
1700	−8.18	13.22	−30.65	−37.55	−2.03	−34.09
1800	−8.08	13.28	−31.98	−37.36	−1.93	−33.89
1900	−8.01	13.31	−33.30	−37.18	−1.83	−33.71
2000	−7.98	13.32	−34.37	−37.01	−1.74	−33.53

data is that the WC has the most negative values for both enthalpy and free energy of formation compared to W_2C.

It can be seen from Table 5.2 that at room temperature, the change in free energies of formation (ΔG_f^o) for both WC and W_2C are favoured by exothermic reactions, with that for WC more favourable since it has more negative value. This trend runs opposite to each in these carbides with increasing temperature. At the highest temperature of 2000 K, the formation of W_2C is expected to be thermodynamically more favourable based on its free energy of formation coupled with the increase in its entropy value.

Although, phase formation and diffusion of other form of carbon in W have been previously investigated [10], [13]–[15], [20], [21], but glassy carbon

is expected to interact differently with W. In terms of chemical reactivity, glassy carbon is less reactive compared to other forms of carbon. This is because it has low porosity and high impermeability compared other carbons [22]. It also has a disordered structure which make it almost impossible to form an intercalation compounds [22]. Therefore, it is expected that the interaction of glassy carbon with tungsten will be characterized by slow reaction rate.

5.5 Mechanism of tungsten carbide formation

Carbon and tungsten interact at higher temperatures to form tungsten carbides. The temperatures at which tungsten carbides are formed depend on the form of the reactants and the interaction atmosphere [20]. For example, the carburization of polycrystalline tungsten wires with carbon powder started at 1550 °C. But, with pure single-crystalline W wires, no carbide formation was observed up to a temperature of 1900 °C [20]. Thin layers of C and W deposited by decomposition of gaseous hydrocarbons reacted at temperatures as low as 800 °C to form W_2C and WC [20]. In sputter deposited multi-layers of C and W films, carbide formation was observed even at room temperature [20]. This suggests the presence of more grain boundaries which act as diffusion paths at lower temperatures.

The process of tungsten carbide formation from the interaction of carbon with tungsten depends on three factors [20]. These are (i) the amount of carbon atoms supplied to the surface of the tungsten; (ii) the diffusion rate of carbon

through the layer of tungsten carbide and (iii) the chemical reaction rate at the interface of the two elements. It has been confirmed [21] that the second factor above dominates at all experimental events where contact is permitted between carbon and the tungsten. An analysis of the carburization kinetics of tungsten powders mixed with carbon and heated in H_2 atmosphere has been attempted with a mathematical model, which presumed C diffusion through a shell of WC growing into the W particles as the rate-determining factor. The rate of carburization is found to be inversely proportional to the square of the crystallite size [20]. The coarser the tungsten particles, the higher the temperature required for complete carburization and the longer the time required.

5.6 Phase selection

When thin films of two substances in close contact are heated, the phase formation is usually sequential [23] In the past, it was difficult to understand this because phase formation sequence was evaluated from bulk diffusion couples where phases appeared to form simultaneously. Phase formation sequence in thin films is now well recognized [23] and experimentally verified by a number of experimental techniques such as Rutherford backscattering spectrometry (e.g. Figure 5.3) and transmission electron microscopy.

From thermodynamic point of view, the phase selection is believed to rely on two main factors. These are; (i) the need for the existence of sufficiently

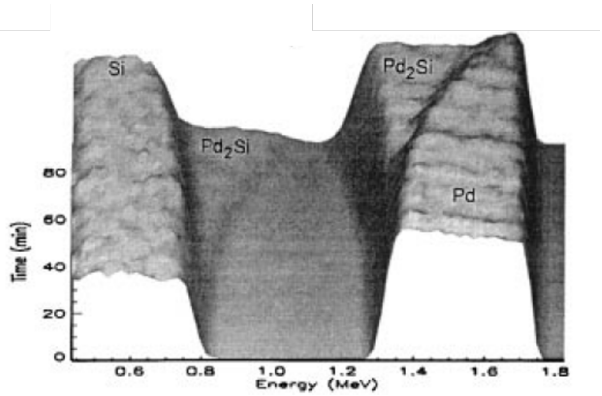

Figure 5.3: An example of single phase formation observed in thin films study with RBS technique. The phase observed was Pd_2Si. Adapted from [23]

large thermodynamic driving force for phase formation (ii) In addition to a driving force, phase formation requires adequate atomic mobility for fast growth kinetics. There were a lot of studies reported in the literature on which of the factors mentioned above dominate in predicting phase formation involving solid-state reactions [24]–[27]. This has led to several postulates trying to predict correctly the first phase to form, in addition to subsequent phase selection. The most popular postulates in the literature are described briefly below.

5.6.1 First phase selection based on kinetics

The selection rule for the first phase has been put forward by d'Heurle [28]. This postulate states that:

In general, one gets that which grows!

This postulate assumes that all phases are initially allowed to grow without

any nucleation issues. Subsequently, the phases are competing for specie consumption. As a result, the one that grows fastest is the phase for which the diffusion process has the largest diffusion coefficient at a particular temperature, will be the first phase to be observed.

Despite the appealing logic of this model, it is not popularly applied for modelling thin film solid phase interactions [29]. The major reason for this, is that the diffusion coefficients for thin film solid phase interactions are rather difficult to evaluate. Bulk diffusion coefficients cannot be adopted for thin film diffusion [30] because of the differences in grain boundary, density, texture and stress contents.

5.6.2 Effective heat of formation model

Thermodynamically, the driving force for phase formation and transformation in solid state interaction is the change in Gibbs free energy ΔG [31]:

$$\Delta G = \Delta H - T\Delta S \tag{5.10}$$

where ΔH and ΔS are the enthalpy and entropy changes, respectively, during a reaction at temperature T. The change in entropy ΔS is usually negligible during solid state interactions [23], [31], [32]. Therefore, the change in enthalpy of formation of compound ΔH, is a good measure of the free energy change ΔG during solid state interaction [23]. But ΔH alone cannot be used to accurately predict the first phase formation and phase formation sequence. However, several researchers [24]–[27], were unsuccessful in trying to use the values

of enthalpies substances to predict first phase formation. The failure of their models was because the concentration of the reactants at the growth interface was not incorporated into those models [23].

Pretorius *et al.* [32] modified the heat of formation using the concept of the effective heat of formation (EHF) model. With EHF, it is possible to calculate heats of formation as a function of concentration of the reactants at the growth interface. This model is expressed by [23]:

$$\Delta H^{'} = \Delta H^{o} \times \frac{effective\ concentration\ limiting\ element}{compound\ concentration\ limiting\ element} \tag{5.11}$$

where $\Delta H^{'}$ and ΔH^{o} are the effective heat of formation and standard heat of formation, respectively. Both are expressed in kJ/mol.at. At the interaction interface in a solid, the two elements will be available in a specific ratio (the effective concentration) and when forming a specific compound, the elements are consumed in the compound ratio. When the effective concentration of a given element is less than its concentration in the compound to be formed, that element is the limiting element. The EHF model assumes single phase formation, because phase formation at the growth interface is a dynamic non-equilibrium process.

The EHF model can be used to predict phase formation if the effective concentrations of the two reacting species at the growth interface is known. It is not possible to determine what the actual effective concentrations of the reactants at the growth interface are, during solid phase interaction. This

problem was circumvented by efforts of Brown and Ashby [33], who have shown that solid state diffusion correlates well with the melting point (i.e. the eutectic point) of a solid. The lower the melting point, the greater the atomic mobility. The most effective intermixing at a reaction interface upon heating occurs at the composition of the liquidus minimum of the binary phase diagram [33]. Therefore, the composition at the liquidus minimum in any binary phase diagram therefore is chosen as the effective concentration during solid state interaction at the growth interface.

The Plot of $\Delta H^{'}$ as a function of elemental effective concentration for the possible phases in a binary phase diagram results in triangularly shaped diagrams, Figure 5.4 (a). When constructing EHF diagrams, the ΔH^{o} value is used and plotted against the atomic concentration of a particular element in a compound. Each triangle represents the energy released during the formation of a particular phase.

For example, Figure 5.4 shows the Co-Si binary phase diagram with triangularly shaped diagrams for $\Delta H^{'}$ versus Si concentration. In this Co-Si phase diagram, the effective heat of formation diagram, Figure 5.4 (a), shows that for an effective concentration at the growth interface of less than about 38 at.% Si, formation of Co_2Si will lead to the biggest change in free energy, while above 38 at.% Si, formation of CoSi is thermodynamically favoured [23], [31].

This Co-Si phase diagram has a well defined lowest eutectic point of 1195 °C at a composition of about 24 at.% Si. Mixing is thus expected to take place at this

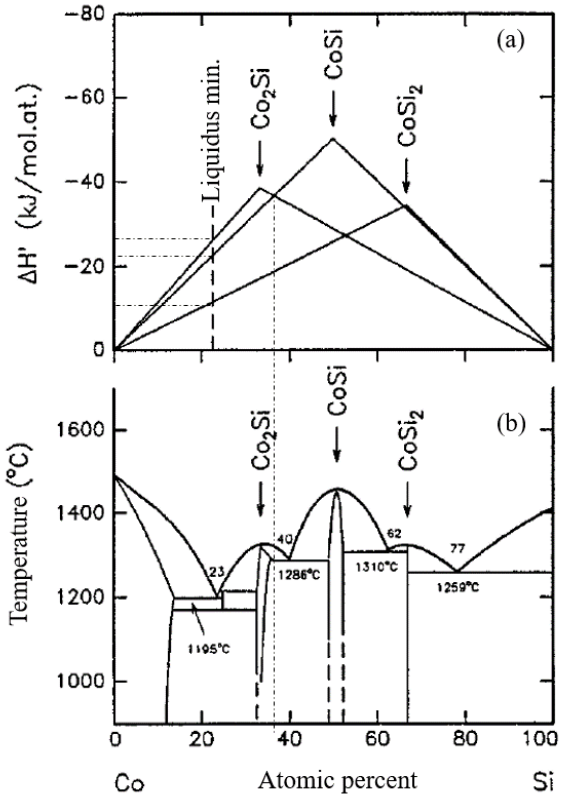

Figure 5.4: The EHF diagram for the Co-Si binary phase diagram, showing that at the concentration of the liquidus minimum the phase Co_2Si has the most negative effective heat of formation [23]

composition and the EHF model therefore predicts Co_2Si as the first phase to form since it has the most negative effective heat of formation of -26 kJ/mol.at. Using the liquidus minimum line, the next phase sequence is followed by CoSi and $CoSi_2$, as the second and third phase, with the effective heat of formation of -22.5 and -10 kJ/mol.at., respectively. This model correctly predicted the first phase formation for 64 out of 84 [23] binary phase diagrams investigated. The ability of EHF model to predict phase formation and sequence, will be harnessed in Chapter 7, to explain the phase formation sequence of the

tungsten carbides observe in this study. This will be done in conjunction with the available thermodynamic data for tungsten carbides discussed in Section 5.4.

REFERENCES

[1] Y. L. Liu, H. B. Zhou, S. Jin, Y. Zhang, and G. H. Lu, "Dissolution and diffusion properties of carbon in tungsten," *Journal of Physics: Condensed Matter*, vol. 22, no. 44, pp. 445–504, 2010.

[2] A. I. Gusev, A. A. Rempel, and A. J. Magerl, *Disorder and order in strongly nonstoichiometric compounds: Transition metal carbides, nitrides and oxides*. Springer Science & Business Media, 2013, vol. 47.

[3] A. Kurlov and A. Gusev, "Tungsten carbides: Structure, properties and application in hardmetals. Springer, Cham-Heidelberg, New York," 2013.

[4] R. Abbaschian and R. E. Reed-Hill, *Physical metallurgy principles*. Cengage Learning, USA, 2008.

[5] W. D. Callister and D. G. Rethwisch, *Materials science and engineering: An introduction*. John wiley & sons, New York, 2007.

[6] E. Lassner and W. D. Schubert, *Tungsten: Properties, chemistry, technology of the element, alloys, and chemical compounds*. Kluwer Academic / Plenum Publishers, New York, 1999, pp. 1–447.

[7] P. Kofstad, "Defects and transport properties of metal oxides," *Oxidation of metals*, vol. 44, no. 1-2, pp. 3–27, 1995.

[8] H. Goldschmidt and J. Brand, "The tungsten-rich region of the system tungsten-carbon," *Journal of the Less Common Metals*, vol. 5, no. 2, pp. 181–194, 1963.

[9] I. L. Shabalin, *Ultra-high temperature materials I: Carbon (graphene/graphite) and refractory metals*. Springer, Manchester, 2014.

[10] P. Gustafson, "Thermodynamic evaluation of C-W system," *Materials science and technology*, vol. 2, no. 7, pp. 653–658, 1986.

[11] L. Willey and H Margolin, "Metals handbook," *Metallography, Structures and Phase Diagrams, 8th edition, American Society for Metals, Metal Park, Ohio*, vol. 8, pp. 386–678, 1973.

[12] E. Rudy, "Conpendium of phase diagram data. Ternary phase equilibria in transition metal–boron–carbon–silicon systems," *Final Report, Air Force Materials Laboratory, Wright-Patterson Air Force Base, Ohio*, vol. 522, 1969.

[13] A. Kurlov and A. Gusev, "Tungsten carbides and WC phase diagram," *Inorganic Materials*, vol. 42, no. 2, pp. 121–127, 2006.

[14] R. Sara, "Phase equilibria in the system tungsten-carbon," *Journal of the American Ceramic Society*, vol. 48, no. 5, pp. 251–257, 1965.

[15] D. Gupta and L. Seigle, "Free energies of formation of WC and W_2C, and the thermodynamic properties of carbon in solid tungsten," *Metallurgical Transactions A*, vol. 6, no. 10, pp. 1939–1944, 1975.

[16] A. D. Mah, "Heats of combustion and formation of carbides of tungsten and molybdenum," Bureau of Mines, Berkeley, CA (USA), Tech. Rep., 1963.

[17] F. Gronvold, S. Stolen, E. F. Westrum Jr, A. K. Labban, and B. Uhrenius, "Heat capacity and thermodynamic properties of ditungsten carbide, W_2C_{1-x}, from 10 to 1000 K," *Thermochimicu Acta*, pp. 115–125, 1988.

[18] T. Iwai, I. Takahashi, and M. Handa, "Gibbs free energies of formation of molybdenum carbide and tungsten carbide from 1173 to 1573 k," *Metallurgical Transactions A*, vol. 17, no. 11, pp. 2031–2034, 1986.

[19] R. Coltters and G. Belton, "High temperature thermodynamic properties of the tungsten carbide WC determined using a galvanic cell technique," *Metallurgical Transactions A*, vol. 14, no. 9, pp. 1915–1919, 1983.

[20] H. Jehn, G. Bär, E. Best, and E. Koch, "Reactions with carbon," in *W Tungsten: Supplement Volume A 5B Metal, Chemical Reactions with Nonmetals Nitrogen to Arsenic*, Springer, Berlin, 1993, pp. 131–154.

[21] M. Pirani and J. Sandor, "Diffusion of carbon into tungsten," *Journal of the institute of metals*, vol. 73, no. 5, pp. 385–395, 1947.

[22] SPi Supplies, USA, *Glassy carbon product information*, https://www.2spi.com/catalog/documents/Glassy-Vitreous-Carbon-Info.pdf, Accessed: May 24, 2020.

[23] R. Pretorius, C. C. Theron, A. Vantomme, and J. W. Mayer, "Compound phase formation in thin film structures," *Critical reviews in solid state and materials sciences*, vol. 24, no. 1, pp. 1–62, 1999.

[24] G. Majni, C. Nobili, G. Ottaviani, M. Costato, and E. Galli, "Gold-aluminum thin-film interactions and compound formation," *Journal of Applied Physics*, vol. 52, no. 6, pp. 4047–4054, 1981.

[25] K. Tu, G. Ottaviani, R. Thompson, and J. Mayer, "Thermal stability and growth kinetics of co2si and cosi in thin-film reactions," *Journal of Applied Physics*, vol. 53, no. 6, pp. 4406–4410, 1982.

[26] E. Colgan, "Phase formation and dissociation in the thin-film pt/al system," *Journal of applied physics*, vol. 62, no. 4, pp. 1224–1231, 1987.

[27] R. Bene, "A kinetic model for solid-state silicide nucleation," *Journal of applied physics*, vol. 61, no. 5, pp. 1826–1833, 1987.

[28] F. d'Heurle, "Theoretical considerations about phase growth and phase formation," *MRS Online Proceedings Library Archive*, vol. 402, 1995.

[29] J. Demeulemeester, "PhD thesis, Universiteit Leuven, Belgium," 2010.

[30] F. d'Heurle, "Nucleation of a new phase from the interaction of two adjacent phases: Some silicides," *Journal of materials research*, vol. 3, no. 1, pp. 167–195, 1988.

[31] J. Li, J. Strane, S. Russell, S. Hong, J. Mayer, T. Marais, C. Theron, and R Pretorius, "Observation and prediction of first phase formation in binary Cu-metal thin films," *Journal of applied physics*, vol. 72, no. 7, pp. 2810–2816, 1992.

[32] R. Pretorius, A. Vredenberg, F. Saris, and R. De Reus, "Prediction of phase formation sequence and phase stability in binary metal-aluminum thin-film systems using the effective heat of formation rule," *Journal of applied physics*, vol. 70, no. 7, pp. 3636–3646, 1991.

[33] A. Brown and M. Ashby, "Correlations for diffusion constants," *Acta Metallurgica*, vol. 28, no. 8, pp. 1085–1101, 1980.

CHAPTER

SIX

EXPERIMENTAL TECHNIQUES AND PROCEDURES

6.1 Introduction

In this chapter, a brief but concise description of the preliminary steps taken to ensure that the samples conditions meet the minimum standard required to achieve better results are given. Great care was taken in the sample preparation, sputtering and annealing stages. This helps to avoid sample mishandling and contamination, which could adversely affect the experimental results. The main techniques employed for the study of glassy carbon interaction with tungsten are also described in this chapter. The techniques used in this research for sample characterization are the Rutherford backscattering spectrometry, X-ray diffraction, Raman spectroscopy, scanning electron microscopy and atomic force microscopy. A brief descriptions are provided on each of these techniques.

6.2 Sample preparation

The starting materials in this study were strips of glassy carbon. The rectangular glassy carbon strips were obtained from Hochtemperatur-Werkstoffe GmbH, Germany. The Sigradur© G glassy carbon grade has a density of 1.42 g/cm^3, flexural strength of 260 MPa, compressive strength of 480 MPa, Young's modulus of 35 GPa, thermal conductivity of 6.3 W/m.K and maximum service temperature up to 3000 °C [1]. This Sigradur© G grade of glassy carbons were prepared from phenolic resins by controlled pyrolysis in an inert atmosphere at temperature in excess of 2000 °C [1].

The glassy carbon strips were cut into smaller size of 5 mm $\times$ 10 mm$\times$ 2 mm. The samples were mechanically polished on an ATM Saphir 500 polishing machine, using 0.25 μm diamond solution before being cleaned. The cleaning procedure involved placing the samples in ultrasonic bath and got them cleaned in alkaline soap solution. The de-ionized water was used to remove the soap solution from the samples. This was repeated thrice to ensure that there was no soap solution left behind on the samples. Thereafter, methanol was used to rinse the samples for 10 minutes so as to remove the de-ionized water. The samples were then placed in an oven at 30 °C for 3h to ensure they were thoroughly dried. The tungsten (W) metal target used for sputtering was obtained from Sigma-Aldrich Pty Ltd, South Africa. It is in a form of a rectangular block with a dimension of 0.25 in.$\times$ 2 in. $\times$ 6 in. The purity of the W target is 99.95 % [2].

6.3 Physical vapour deposition

Preparation of thin films by physical vapor deposition (PVD) is of high technological importance in many industrial processes. PVD is widely used in the production of hard and wear resistant coatings, diffusion couples and many other applications in semi-conductor devices.

Generally, PVD is based on the production of a vapour by physical processes and the subsequent condensation on the substrates as thin films [3]. The two most popular methods of producing thin films are the sputtering and evaporation. The evaporation method involves transfers of target atoms thermally into the gas phase while in sputtering, target atoms are ejected by ion bombardment and the atoms condense onto a substrate in a high vacuum [4].

Figure 6.1 illustrates a general manifestation of a magnetron sputtering system. A permanent magnetic structure is located behind a target serving as a deposition source in magnetron sputtering system [5]. Plasma confinement on the target surface is achieved by the permanent magnetic structure placed behind the sputtering target. The resulting magnetic field forms a closed-loop annular path, acting as an electron trap, shown in Figure 6.1 (a). This reshapes the trajectories of the secondary electrons ejected from the target into a cycloidal path. This in turn, greatly increases the probability of ionization of the sputtering gas within the confinement zone.

In the sputtering process, a target plate is bombarded by energetic ions

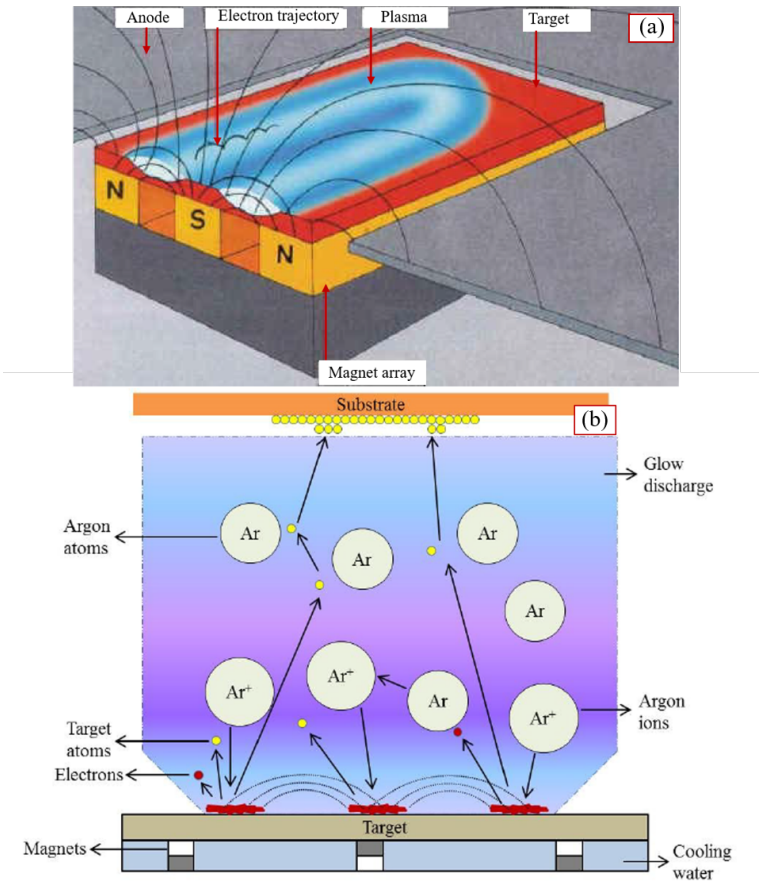

Figure 6.1: General principle of operation of magnetron sputtering system. (a) Cycloidal path formation in sputtering target (b) Transport of sputtered atoms in plasma medium. Adapted from [5]

generated in a glow discharge plasma, situated in front of the target. The bombardment process causes the sputtering of the target atoms, which then condense on the substrate as a thin films. Secondary electrons are also ejected from the target surface as a result of the ion bombardment [6], [7] and these electrons play an important role in sustaining the plasma.

Inert gases, specifically argon, are usually employed as the sputtering gas because they do not react with the target material [4]. By applying a

biased voltage to the cathode, i.e. the sputtering target, positively charged ions are attracted from the plasma towards the target. This resulted in the bombardment of target, where atoms are being removed from its surface. These sputtered atoms are then transported to the substrate surface (see Figure 6.1 (b)) where condensation and accumulation of target material take place to form a solid deposit [8].

The film deposition rate largely depends on the sputtering power and the gas pressure. Sputtering is usually carried out in a chamber which is adequately pumped down, with the chamber pressures typically in the range of 10^{-4} to 10^{-7} mbar [9]. With appropriate deposition parameters, thin films deposition by sputtering has the advantage of producing films which are fairly uniform with good adhesion to the substrate.

6.3.1 Tungsten film preparation

In this study, the MDX magnetron sputtering system made by Advanced energy industries, Inc. was employed for sputtering tungsten films onto the glassy carbon substrates. This sputtering system is housed in the Physics department of University of Pretoria. The sputtering preparation began with carefully mounting the glassy carbon substrates on a cleaned circular sample holder. Small pins and screws were used to fix the samples to the metallic holder with a diameter of 10 cm. The chamber of the magnetron sputtering system was then opened, and the samples firmly fixed to the holder were carefully mounted on the socket meant for the sample holder. The distance

between the mounted samples and tungsten target was approximately 20 cm. The chamber cover was replaced with the lid fastened with bolts and nuts. Then the chamber was pumped down by a combination of fore pump and turbo pump until the pressure of 10^{-6} mbar was achieved.

Prior to thin film deposition, the argon gas was introduced into the chamber with its pressure adjusted to 3×10^{-2} mbar. This gave rise to gaseous plasma in the chamber when the magnetron was switched on. The surface of W target was etched by the Ar plasma for 5 min to ensure that any contaminant on its surface was removed before the actual sputtering process began. The magnetron sputtering system consists of a cathode (target) and an anode (sample holder) positioned opposed to each other in a vacuum chamber. When a high voltage in the range of 2000 V is applied between cathode and anode, a glow discharge is ignited.

The sputtering parameters were carefully optimized after several attempts to ensure good adhesion between the W films and glassy carbon substrates. Most of the films prepared during the optimization of the sputtering parameters, were characterized by rough surfaces. These films easily got delaminated upon annealing and peeled off. The magnetron was powered by a voltage of 500 V. With the optimized working gas pressure and current of 4×10^{-3} mbar and 0.29 A on the magnetron, respectively, the sputtering power of 145 W was used to carry out the sputtering of the samples. These sputtering parameters

gave a power density applied to the sputtering target as 0.66 W/cm^2. Subsequent W films prepared with these sputtering parameters were smooth and firmly adhered to the glassy carbon. The observations of the films under the scanning electron microscope (SEM), showed an absence of delamination for films annealed even at 1000 °C.

The optimized sputtering parameters were obtained by decreasing the working gas pressure. Unlike the initially prepared W films which peeled off easily, the W atoms do not undergo many collisions with the Ar atoms in the plasma [10]. So, the sputtered W atoms attached to the growing films with higher energy and easily diffuse into the films, which resulted in the formation of dense film structure. Increased working gas pressures caused the film structure to have a voided structure with isolated columnar crystallites characterized by tensile stress [11], hence such films peeled off. At the end of each sputtering exercise, once the magnetron was turned off, the vacuum chamber was left under vacuum for at least 6 hours before breaking the vacuum. This was done to avoid possible oxidation of the films.

At the early stage of the study, a number of samples were sputtered for various durations to determine the average deposition rate. Four W films were prepared at sputtering duration of 5, 10, 15 and 20 min and films were analysed with RBS. The film thicknesses were estimated from RUMP simulation. These thicknesses were plotted against the sputtering duration (Figure 6.2). The slope of the graph is equivalent to the average deposition rate of W films on the

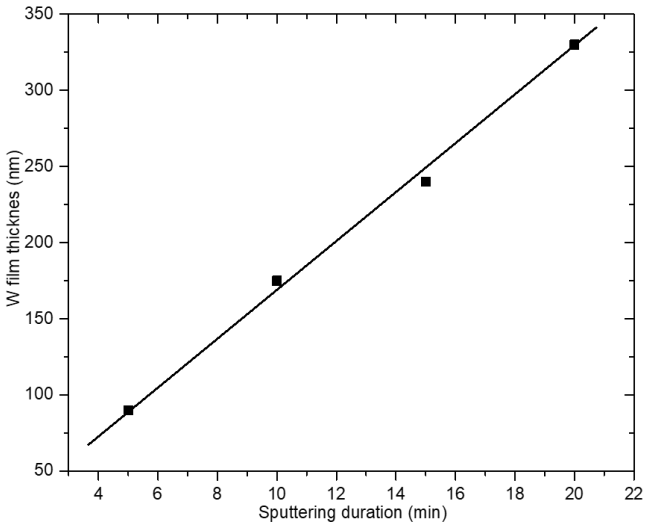

Figure 6.2: Estimation of W deposition rate

glassy carbon substrates and it was estimated to be $\sim$ 16 nm/min. With this estimated deposition rate, it was easy to predict fairly accurately, the amount of sputtering duration needed to obtain a desired W film thickness, provided the sputtering parameters remain almost the same. The first set of samples in this study were sputtered for 4 min to achieve W film thickness estimated at 62 nm. The second and third set were sputtered for 7 min and 14 min to achieve W film thicknesses estimated at 115 nm and 230 nm, respectively.

6.4 Annealing of samples

In solid-state investigation, intermixing of atoms of different species at the interface can be speed up by annealing. This is possible because heat treatment causes higher atomic vibrations. During annealing, the energy needed

to break bonds is provided such that atomic migration is enhanced. For example, diffusion annealing is a popularly used method in the semiconductor industries to drive in impurity atoms into the silicon wafers [12]. The annealing exercise in this study involved heating the W-glassy carbon couples at a desired temperature, for a given duration under high vacuum better than 1×10^{-7} mbar. The tube furnace annealing system shown in Figure 6.3 was used in this study. It can attain a maximum temperature of 1000 °C. Maximum temperature is reached in the regions around the centre of the furnace, and it decreases towards the sides of the furnace. A thermocouple for reading the temperature of the furnace is connected to the sample holder. It's reading had an accuracy of ± 2.2 °C [13]. A large quartz tube which encloses the small tube and the sample is inserted into the turbo pump housing, equipped with two rubber seals to ensure air leak-proof. The furnace itself, has two white circular aluminium oxide, a ceramic materials, which can be inserted at both ends to prevent heat loss to the surrounding.

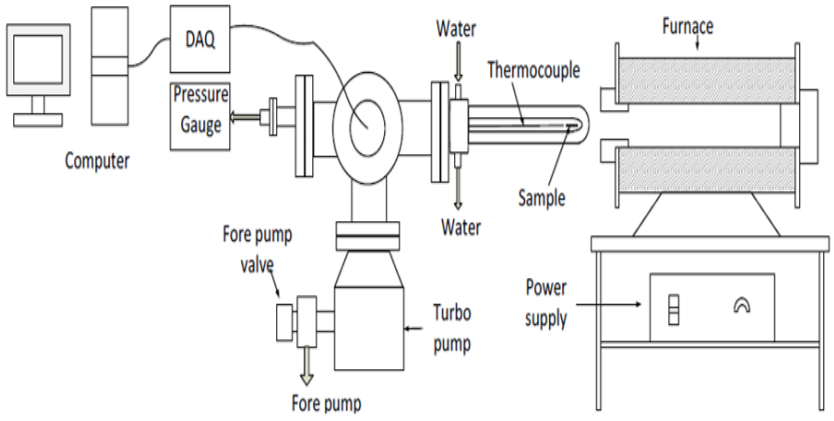

Figure 6.3: The vacuum tube annealing system. Adapted from [14]

The stages in annealing a sample, starts with sample loading process. This involves carefully taking out the tube and placing the sample in the smaller tube which serves as a sample holder. Then the fore pump was first switched on until a pressure of 10^{-3} mbar is attained before switching on the turbo pump. This procedure was observed to be sure that the fore pump is functioning well. The two pumps were left running until the vacuum tube attained a low pressure better than 10^{-6} mbar. The annealing temperature was pre-set at the beginning with the furnace turned on allowing sufficient time to heat up and stabilize at the pre-set temperature. When the user is satisfied with the pressure level, the furnace is drawn over the glass quartz tube already loaded with the sample. The data acquisition program displays on the monitor, the temperature of the furnace during annealing.

At the end of annealing duration, the furnace was pulled away from the annealed sample to allow it to cool down naturally, to room the temperature. Unloading of the samples is only done at room temperature. This was to ensure that the sample did not get oxidized. Oxidation of samples during the annealing process is difficult due to the high level of vacuum obtained before the annealing.

The annealing cycles were done in three different categories; the first set of samples were annealed isochronally at temperatures of 600, 700, 800, 900 and 1000 °C for 1 h. While the second set were annealed isothermally at 300, 400, 500 and 600 °C, for duration of 6, 12, 18 and 24 h, for each sample. The third

set of the samples were annealed from 700 - 1000 °C with a step size of 100 °C for annealing duration of 0.5, 1, 2 and 3 h. These annealed samples were taken for characterizations.

6.5 Rutherford backscattering spectrometry

The most common use of high-energy ion beams is elastic scattering popularly known as Rutherford backscattering spectrometry (RBS) [15], [16]. Other ion beams analysis techniques include the nuclear reaction analysis (NRA) for quantitative light-element detection, particle induced x-ray emission (PIXE) for elemental analysis, and elastic recoil detection (ERD) for depth profiling of hydrogen and its isotopes [16].

In the RBS technique, an accelerator generates a beam of mono-energetic ions of energy in the MeV range, with a typical current of 10 to 100 nA for a beam spot of about 1 mm^2 [15]. In RBS measurement, a mono-energetic ion beam is collimated and incident on a target material. When the positive energetic ions interact with the atomic nuclei of the target material, they are backscattered as a result of coulombic repulsion exerted by the two nuclei. Some of the backscattered ions are recorded by a solid state particle detector mounted at a fixed backscattering angle. With the aid of a multichannel analyzer (MCA), the number of backscattered ions detected are sorted into bins according to their individual energy.

Generally, the detector delivers a signal whose amplitude is proportional to

the backscattered ion energy. RBS analysis give both qualitative and quantitative results. It is usually employed in the analysis involving study of thin film layers to investigate intermixing layers, phase formation and diffusion studies [17]. In addition, the film thickness and elemental composition of layer can be determined from a RBS measurement. The RBS technique is non-destructive and is best suited for analysis of light elements beneath the heavy elements [8], [15]. Helium ions (He^+) with incident energy ranging from 1 to 3 MeV [15] is one the commonly used energetic ion in RBS measurements. The energetic ions which make close encounter with the target nucleus are backscattered. Energies of the backscattered ions are then measured from the scattered events both at the surface and some depths within the target. Backscattering angles commonly used in for RBS measurements ranged between 150° and 170° [15] for better mass resolution.

The classical elastic scattering, governed by Coulomb repulsive effects between the positively charged ions and the nuclei of target atoms is the foundation of RBS technique. This foundation leads to three basic physical concepts of RBS analysis, which are the advantages of this technique. The energy transfer from a projectile to the target nucleus in two body elastic collision leads to the concept of the kinematic factor [15]. This is the mass detection ability of the RBS. The probability of occurrence of this two-body collision leads to the concept of scattering cross section [15], which is the basis of quantitative analysis of atomic composition by RBS. The average energy loss of an ion traversing through the target medium leads to the depth detection

ability of a RBS [15]. The limitation of RBS is associated with poor mass and depth resolutions. This is associated with effects of energy straggling, arising from the statistical fluctuations in the energy loss of an ion traversing moving through a dense target medium [15]. These physical processes which describe the main characteristics of RBS measurements are briefly explained in the sections that follow.

6.5.1 Kinematic factor

The kinematic factor of the target material denoted as K provides the relationship between the incident energy E_o and the backscattered ion energy E_1. This relationship enables the RBS technique to detect the mass of the target material. When an energetic ion of mass M_1 moving with constant velocity, collides elastically with a stationary target of mass M_2 (Figure 6.4), energy will be transferred from the incident ion to the stationary target. The assumption that the interaction between the two bodies is properly described by a simple elastic collision of two isolated particles rests on two conditions [15]:
(1) The projectile energy E_o must be much larger than the binding energy of the atoms in the target. Chemical bonds are of the order of 10 eV, so that E_o is very much larger than that.
(2) Nuclear reactions and resonances must be absent. With He^+ for example, the nuclear effects begin to appear at energy of 2 to 3 MeV.

Figure 6.4 shows the laboratory reference frame geometry of a two-body collision of an incident ion and the target atom initially at rest. For a perfectly

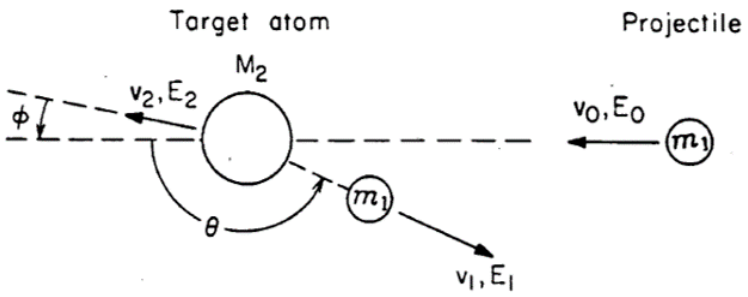

Figure 6.4: Schematic representation of elastic collision between a projectile of mass M_1, velocity v_o and a target of mass M_2 initially at rest [15]

elastic collision, the energy of the backscattered ion after collision depends on the mass of the ion M_1, ion initial energy E_o, initial velocity v_o; the mass of target atom M_2 which was initially at rest, and the backscattering angle θ [18]. After the collision, the ion and the target mass have velocities and energies v_1, E_1 and v_2, E_2, respectively. The angles θ and ϕ are the backscattered and recoil angles of ion and target atoms, respectively.

The derivation of this relationship is demonstrated as follows. In Figure 6.4, using the laws of conservation of energy and momentum along the x and y directions, these expressions are given as follows;

The kinetic energies of the two bodies before and after collision gives:

$$\frac{1}{2}M_1v_o^2 = \frac{1}{2}M_1v_1^2 + \frac{1}{2}M_2v_2^2 \tag{6.1}$$

The momenta before and after collision along the x direction gives:

$$-M_1v_o = M_1v_1\sin(\theta - 90^o) - M_2v_2\cos\phi \tag{6.2}$$

The momenta before and after collision along the y direction yields:

$$0 = -M_1 v_1 \cos(\theta - 90^o) + M_2 v_2 \sin\phi \tag{6.3}$$

By squaring both sides of Equations 6.2 and 6.3 and substituting in Equation 6.1, yields Equation 6.4 upon rearrangement;

$$\frac{M_2}{M_1}\left(1 - \frac{v_1^2}{v_2^2}\right) = \frac{v_1^2}{v_2^2} + 1 - 2\frac{v_1}{v_2}\cos\theta \tag{6.4}$$

And simplifying Equation 6.4 further, yields Equation 6.5:

$$\frac{v_1}{v_o} = \frac{M_1 \cos\theta \pm \sqrt{M_2^2 - M_1^2 \sin^2\theta}}{M_1 + M_2} \tag{6.5}$$

The kinematic factor of the target atom K_{M_2} is the ratio of the backscattered kinetic energy of the projectile ion E_1 to its initial incident energy E_o [15].

$$K_{M_2} = \frac{E_1}{E_o} = \frac{\frac{1}{2}M_1 v_1^2}{\frac{1}{2}M_1 v_o^2} = \left(\frac{v_1}{v_o}\right)^2 \tag{6.6}$$

By applying Equation 6.6 in Equation 6.5, yields Equation 6.7 [15]:

$$K_{M_2} = \left[\frac{M_1 \cos\theta \pm \sqrt{M_2^2 - M_1^2 \sin^2\theta}}{M_1 + M_2}\right]^2 \tag{6.7}$$

Equation 6.7 tells us that, with the full knowledge of scattering angle θ and the energy E_0 possessed by the incident ion, with atomic mass M_1, K_{M_2} can be evaluated from the RBS spectrum. Hence, the mass of the target atom M_2 can be calculated [15] and the target element can be identified.

6.5.2 Scattering cross section

To know how frequently the elastic collisions occur and actually results in a scattering event at angle θ, the knowledge of the differential scattering cross section denoted by $d\sigma/dQ$ is very important. Consider a narrow beam of ions impinging on a thin uniform target which is wider than the beam (Figure 6.5). At the scattering angle θ, a small fraction of the ions are scattered in a very small differential solid angle $\partial\Omega$.

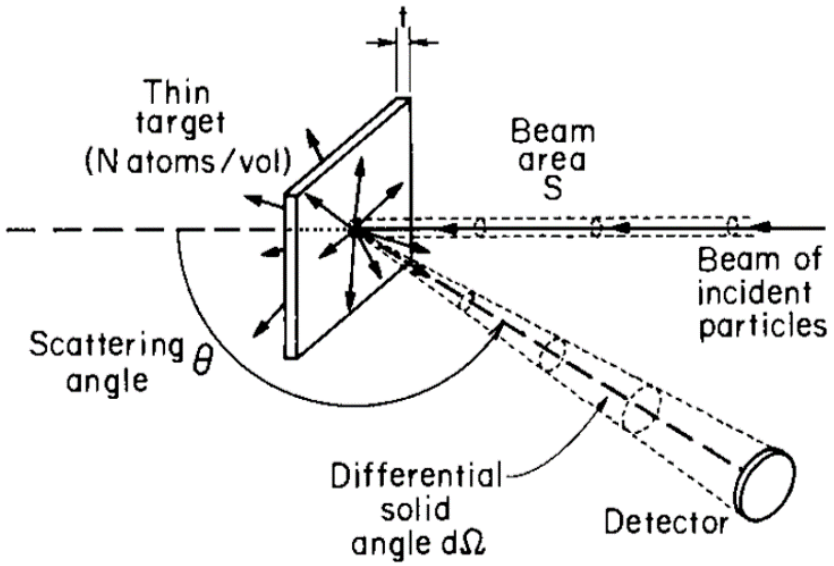

Figure 6.5: Simplified layout of a scattering experiment. Only those few ions scattered within the solid angle $\partial\Omega$ covered by the detector are counted [15]

If Q is the total number of ions that impinged on the target surface and ∂Q is the number of ions counted by the detector, then the differential scattering cross section $\partial\sigma/\partial Q$ is defined as [15]:

$$\frac{\partial\sigma}{\partial\Omega} = \frac{1}{Nt}\left(\frac{\partial Q}{\partial\Omega}\right)\frac{1}{Q} \tag{6.8}$$

where N is the volume density of atoms in the target and t is its thickness. Thus Nt is the number of target atoms per unit area (areal density). But the average differential scattering cross section σ is given by [15];

$$\sigma = \frac{1}{\Omega}\left(\frac{\partial\sigma}{\partial\Omega}\right)\partial\Omega \tag{6.9}$$

For very small detector angles Ω, $\sigma \rightarrow \frac{\partial\sigma}{\partial\Omega}$. By substituting Equation 6.8 into 6.9, it yields:

$$\sigma = \frac{A}{\Omega \cdot Q \cdot Nt} \tag{6.10}$$

where $A = \partial Q$ is the number of backscattered ions counted by the detector, Ω is the solid angle subtended by the detector (Ω=3.41 mSr in this study). The scattering cross section σ is the probability that the scattering events will result in the backscattered ions ending up at the detector. It has the dimension of an area, often expressed in barn, 1 barn = 1×10^{-24} cm^2 [15]. Equation 6.10 shows that when σ and Ω are known, and the numbers of incident ions Q and numbers of detected ions A are counted, then the number of target atoms per unit area Nt, can be determined. This demonstrates the ability of RBS technique to provide quantitative information on the number of atoms present per unit area of a target sample.

6.5.3 RBS energy loss and depth detection

When an energetic ion or particle impinge on a target and traverse into it, the ion suffers a loss in its kinetic energy. This energy loss occurs due to the

electron cloud of the target atoms which lie along its path and various small-angle deflections it encounters due to collisions with atomic nuclei along its way. The amount of energy lost ΔE per length traversed Δx depends largely on the type of energetic ion, the nature of the target and the initial velocity of the ion.

Figure 6.6 depicts the energy loss inwards and outwards by a typical energetic ion with initial energy E_o. Assuming the energy possessed by the

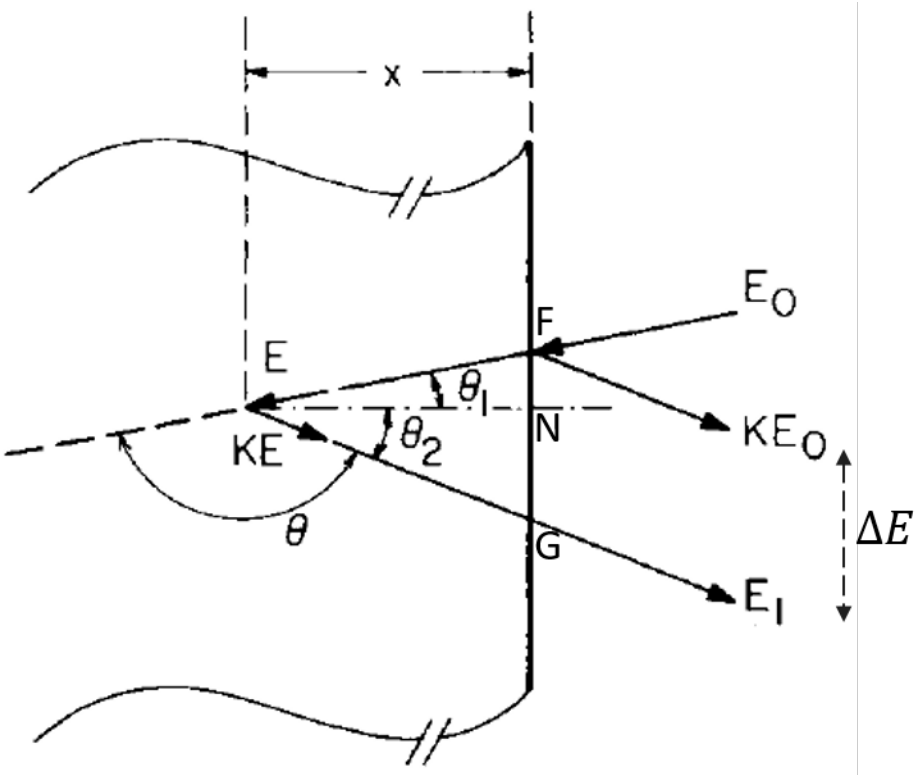

Figure 6.6: Schematic of scattering events of incident ions on the surface and at depth x below the target surface [15]

ion immediately before scattering event at a particular depth x is E, and the energy of the ion after its emergence from the target surface is E_1, the relation

between the energy loss and the depth traversed in the target material can be established using Figure 6.6. Angle θ_1 represents the angle between the target normal and the direction of the incident beam, and θ_2 is the angle between the target normal and the direction of backscattered ion. In triangle FEN, it follows that:

$$\cos\theta_1 = \frac{EN}{EF} = \frac{x}{E_o - E} \tag{6.11}$$

If it is assumed that the energy loss per unit length $\partial E/\partial x$ along the inward and outward paths is constant, then from Equation 6.11, it follows that [15];

$$E_o - E \approx \frac{x}{\cos\theta_1}\left(\frac{\partial E}{\partial x}\right)_{in} \tag{6.12}$$

Similarly for outwards path, using triangle NEG, it follows that;

$$KE - E_1 \approx \frac{x}{\cos\theta_2}\left(\frac{\partial E}{\partial x}\right)_{out} \tag{6.13}$$

By substituting Equation 6.12 into 6.13 to eliminate the energy E immediately before scattering, it yields [15];

$$KE_o - E_1 = \left[\frac{K}{\cos\theta_1}\left(\frac{\partial E}{\partial x}\right)_{in} + \frac{1}{\cos\theta_2}\left(\frac{\partial E}{\partial x}\right)_{out}\right] x \tag{6.14}$$

where KE_o is the energy of ions backscattered from the target atoms at the surface. The difference between these two energies counted by the detector is the energy loss ΔE, given by [15];

$$KE_o - E_1 = \Delta E = [S]x \tag{6.15}$$

where;

$$[S] = \left[\frac{K}{\cos\theta_1}\left(\frac{\partial E}{\partial x}\right)_{in} + \frac{1}{\cos\theta_2}\left(\frac{\partial E}{\partial x}\right)_{out}\right] \tag{6.16}$$

is called the energy loss factor. Equation 6.15 is the basis for depth detection ability of the RBS technique. It shows that the energy lost by a traversing ion is directly proportional to the depth penetrated into the target sample [15].

The unit of depth in RBS measurement is conveniently expressed in atoms per unit area (at./cm^2). Therefore, the proportionality stated above can be mathematically expressed as [15];

$$\Delta E \propto Nx \tag{6.17}$$

This implies that:

$$\Delta E = \varepsilon N x \qquad \varepsilon = \frac{1}{N}\frac{\partial E}{\partial x} \tag{6.18}$$

where N is the atomic density of the target material and ε is the proportionality constant, known as the stopping cross section [18]. Equation 6.15 can be expressed in terms of stopping cross section instead of energy loss by unit length $\partial E/\partial x$ by application of Equation 6.18 in 6.16. Thus;

$$\Delta E = \left[\frac{K}{\cos\theta_1}(\varepsilon)_{in} + \frac{1}{\cos\theta_2}(\varepsilon)_{out}\right] Nx \tag{6.19}$$

$$\Delta E = [\varepsilon] N x \tag{6.20}$$

where;

$$[\varepsilon] = \left[\frac{K}{\cos\theta_1}(\varepsilon)_{in} + \frac{1}{\cos\theta_2}(\varepsilon)_{out}\right] \tag{6.21}$$

is the stopping cross section factor [15]. Any one of Equations 6.15 and 6.18 can easily be used to determine the thickness of thin film since the values of $[S]$ and $[\varepsilon]$ are usually tabulated in the literature.

6.5.4 The RBS setup

A typical RBS setup consists of these main components; ionization chamber for ions generation, a network of beam lines in which the ions are accelerated and a scattering chamber, where the interactions between the energetic ions and the target materials occur. The beam line is under high nitrogen pressure to prevent sparking.

For experimental purposes, the most popular accelerator in use is the Van de Graaff accelerator (Figure 6.7). To produce an accelerated beam of positive ions requires an ion source, an accelerating voltage, an evacuated acceleration path, a vacuum system, and an adequate control system.

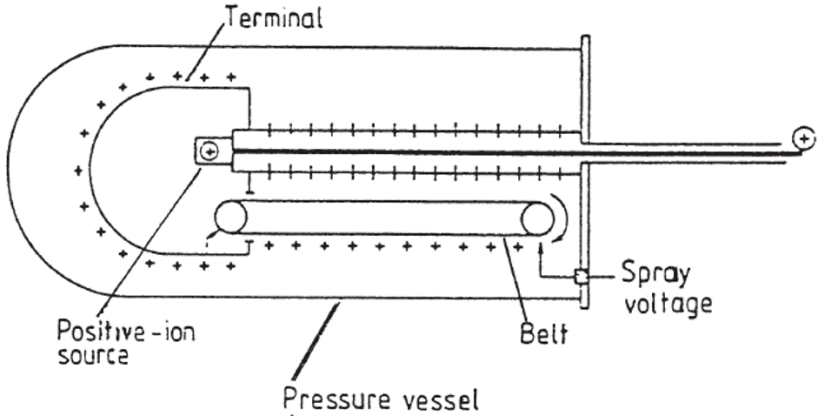

Figure 6.7: Schematic of a Van de Graaff accelerator [19]

The positive ion source uses a glass bottle to which RF energy is applied so that

the gas introduced into the source bottle is ionized. This results in a plasma that is magnetically focused at the exit canal of the source bottle. Positive ions are initially expelled through the exit canal into the acceleration path by a potential applied to the anode of the source bottle (Figure 6.7). Further acceleration is provided by the voltage gradient developed along the tube.

A high voltage is produced on the terminal shell by continuously charging it by means of a rapidly moving belt that conveys charges between ground potential and the terminal. A voltage insulating tube mechanically supports the terminal and the belt-charging system. This tube provides the electrostatic environment for the accelerator tube that maintain the voltage gradient along the tube. The drive motor moves the charging belt that is built into the upper pulley for terminal power. The belt charging current is supplied from a DC power source located outside the pressure vessel. The acceleration path for the positive ion beam is provided by an accelerator tube, which is under high vacuum to minimize collisions between the accelerated ions and the extraneous gas molecules in the tube. The normal operating pressure of the accelerator tube system is about 10^{-6} mbar.

The ions, after passing through a short drift tube, enter an analysis magnet, where the various species of ions are separated. The analyzed beam is then collimated and directed onto the target. A few of the ions are elastically backscattered from the target, but only those which are backscattered in a particular direction are detected by the particle detector; their energy is

analyzed and stored in an appropriate data storage system.

The scattering chamber has a platform for mounting samples. Also present in the scattering chamber are; three axis goniometer for controlled tilting and rotating of the samples, a silicon based solid-state detector (SSD) fixed at 165° relative to the incident beam direction and a 1 mm diameter collimator connected to the beam line [14]. All these components are linked to the sample platform. The scattering chamber evacuation system consists of a fore pump and turbo pump. By running both pumps, the chamber pressure can attain a low pressure better than 10^{-7} mbar.

6.5.5 RBS measurement procedure and data acquisition

The measurement procedure starts with first checking that everything is fine, especially the gas reading. Once the control system is powered up, a short period of time is allowed for the helium gas to get ionized. At this point, measurement section is next where the vacuum in the scattering chamber is broken and the chamber cover is left opened with the aid of crane. Then a sample to be measured is loaded and the chamber gently closed. Then the chamber pumping down procedure, which involves a turbo and fore pumps is carried out. Once a chamber pressure below 1×10^{-5} mbar is achieved, the beam line is opened. Due to the configuration adopted, there is no room for multiple samples, as only one sample can be measured at a time. When the straight beam is established in the control section, efforts and manipulation skill are essential to successfully adjust the gas pressure, beam current and

the charging control knobs until the analysis beam which passes through the right beam line is established.

The Van de Graaff accelerator at the University of Pretoria is capable of producing a beam of He ions with energies up to 2.7 MeV. Beam energies of 1.4 MeV and 1.6 MeV are usually adopted for measurements in the laboratory. As reported by Brijs, *et al*. [20], lowering the energy of the probing beam between 0.5 MeV and 2 MeV, helps to improve the depth resolution and sensitivity of RBS.

The backscattered ions are detected by the SSD, which is fixed at a scattering angle of 165° relative to the direction of the incident beam (Figures 6.5 and 6.6). When the backscattered ions impinge on the detector, they deposit their energies on the detector to create electron-hole pairs. These electron-hole pairs are separated by an applied electric field, a reverse bias of 40V (Figure 6.8) and create a signal pulse. The number of these electron-hole pairs and height of pulse are proportional to the energy deposited by the backscattered ions [15]. The Si detector is connected to a pre-amplifier and an amplifier where the output signal is fed into a multichannel analyser (MCA).

The current collected at the back of the target sample is fed into the current integrator, where it is converted into digital form. The logic signal from the current integrator is sent into a charge counter where its output is fed to the MCA and the counter. The digital signal from this current prompts the MCA to start processing the unipolar signal from the amplifier [21]. It also instructs

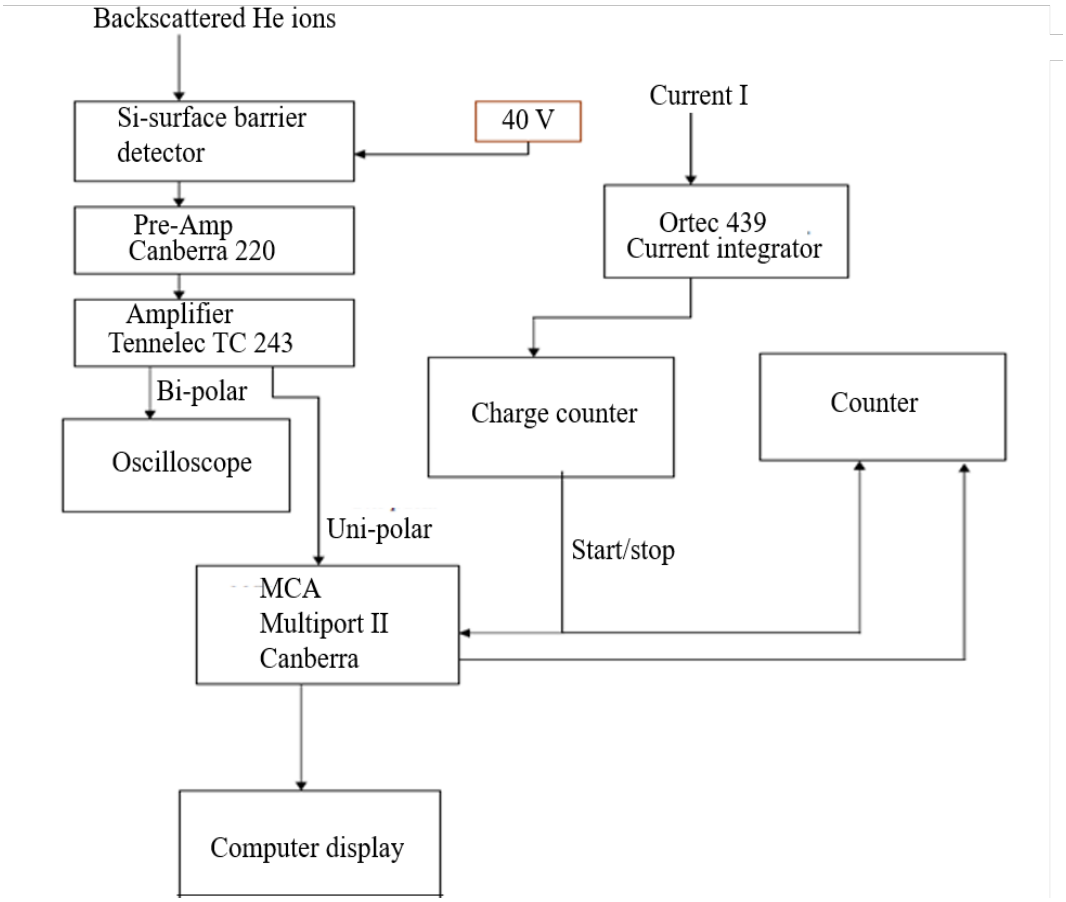

Figure 6.8: Schematic of the electronic circuit for RBS measurements [21]

the counter when to start counting and when to stop. The Canberra-220 MCA which is interfaced with a computer, further process the data. The MCA has 512 channels, so the RBS energy spectrum is displayed with energy ranging from 0 to 1.6 MeV within this channel range. In each channel, a specific energy of the backscattered ions are sorted according to the energy discriminator [22].

The RBS results in counts versus channel numbers were obtained by collecting a total charge of 8 μC per measurement. The beam current was maintained at 5 nA, this helps to minimize pile up and early degradation of the detector.

For better statistics in the counts, each measurement was repeated 3 times. The average of the measurements was adopted for further analyses. Depending on the beam current, it takes between 10 to 25 minutes to measure a sample.

The channel numbers have a linear relationship with the backscattered energy of ions that impinged on the detector. This linear relation is given by [15];

$$E = kx + c \tag{6.22}$$

where k is energy per channel in keV/ch., x is channel number and c is the intercept or offset expressed in keV. Accurate energy calibration is an important step for better RBS simulation. Section 7.2 presents the procedure for determining these parameters.

6.5.6 RBS simulation codes and data analysis

Simulation programs are required for analysis of the RBS data. There is a variety of computer programs used for simulating RBS spectra. Each simulation code has its own advantages and disadvantages. The popular computer simulation codes include RUMP, RBX, SIMNRA, DEPTH and Data Furnace [23]. These computer codes calculate RBS spectrum for a given target structure and allow fitting of target compositions to the measured RBS spectra.

RUMP and SIMNRA are the available simulation codes in our research group. SIMNRA is known to be one of the best and most commonly used simulation programs. SIMNRA works in Microsoft Windows system and it

provides simulation of backscattering spectra for ion beam analysis and is mainly intended for nuclear reactions, elastic recoil detection analysis and non-Rutherford backscattering, but can also be used for RBS [23]. It can calculate for any combination of impinging ions and target atoms at any geometry of experimental equipment. RUMP (Rutherford Universal Manipulation Program) is the second most commonly used simulation program for RBS data [24]. The first version of RUMP program was created in FORTRAN language but later was based on the ANSI C programming language. The original computer code was developed by Doolittle, *et al.* [25], who were members of Dr. J.W. Mayer's research group at Cornell University. This program was specifically designed for the simulation and analysis of RBS data. Stopping powers in RUMP were ensured for helium, hydrogen and deuterium for energies ranging up to 3 MeV [26].

6.5.7 RUMP simulation

RUMP code was used in this study to simulate the RBS spectra. RUMP code make use of the stopping power values credited to Ziegler, *et al.* [27]. Simulations with RUMP code requires a lot of investment in time and computer skills. This code is not user friendly like windows based programs, hence it requires a lot of user interventions. The simulation is an iterative, time consuming tasks which involves constantly comparing the simulated spectrum with the experimental RBS spectrum, and continuously making adjustments to the simulation description file until the best fit is achieved [26].

Simulation with RUMP starts with entering some of the experimental parameters into the code. Parameters such as type of incident ions, energy of incident ions, geometry of experiment, energy per channel and offset, charge collected, current, scattering angle, solid angle of detector, detector energy FWHM as well as the appropriate sample composition must to be inputted into the simulation code. In addition, a number of layers is specified and the thickness and elemental composition of W and glassy carbon defined (Figure 6.9). Then the simulated spectra is generated and compared with the experimental RBS spectrum. The main objective is to simulate a spectrum which agrees with the experimental RBS spectrum with the best accuracy possible. In comparing the simulated spectra with the experimental RBS spectra,

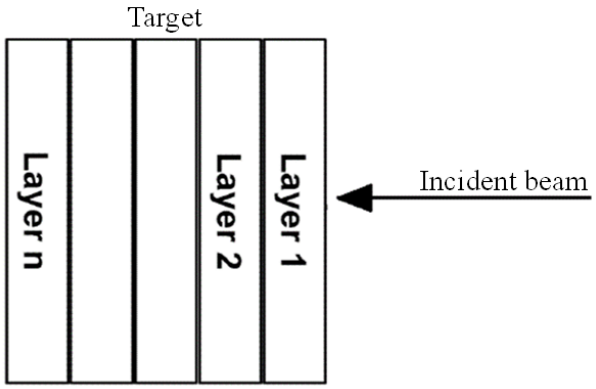

Figure 6.9: Schematic of sample structure divided into a number of n-layers for RUMP simulation]

two important considerations must be bore in mind;

(1) the reliability and physical meaning of fits obtained. It is possible, that the obtained simulated spectrum does not agree with the experimental RBS spectrum. This could be due to insufficient characterisation of all processes

which were possible during RBS measurements. For example, effect of multiple scattering from a thick film is not reproducible in RUMP code.
(2) the simulated spectrum obtained may agree well with the RBS data, but may not have any physical meaning. Hence, the onus is on the user to find a compromise between these two facts, during simulation of the RBS data. The correct knowledge of the sample history is key to accurate RBS data simulation with RUMP code.

6.6 Raman spectroscopy

Raman spectroscopy is a non-destructive technique used for chemical and structural analysis of materials by application of Raman effect. It allows sensitive structural identification of trace amounts of substances based on their unique vibrational characteristics (fingerprints) [28]. It provides detailed information about chemical structure, crystallinity and polymorphism [28]. This technique is based on the interaction of light with the chemical bonds within a material under investigation.

The genesis of Raman spectroscopy was in the first quarter of the 20th century when the scattering of monochromatic radiation with change of frequency was predicted theoretically by an Austrian physicist S. Adolf [29]. Although, many studies on light scattering from various media had long been studied by several researchers between 1871 and 1910 [30], but no change of wavelength had been observed, except for certain types of scattering in

the X-ray spectral region observed by Compton [31]. As a follow up on this background, Raman and Krishnan [32] first reported the idea of inelastic scattering.

The information provided by Raman spectroscopy results from a light scattering process. Raman spectroscopy gives information about intra and inter-molecular vibrations of molecules. This technique provides a spectrum which is characteristic of the specific vibrations of a molecule and are valuable for identifying a substance. No two substances give exactly the same Raman spectrum, and the intensity of the scattered light is related to the amount of material present. This makes it easy to obtain both qualitative and quantitative information about the sample

6.6.1 Principle of Raman Spectroscopy

When light photon interacts with molecules, it can be absorbed if the energy of the incident photon matches the energy difference, ΔE, between the ground state and an excited state, thereby fulfilling the Bohr frequency condition [33], [34]:

$$\Delta E = hv \tag{6.23}$$

where h is the Planck constant and v is the frequency of the incident photon. However, in most cases the incident photon does not match the molecular transition and the vast majority of the photons are scattered with the same energy as the incident photons [33]. This phenomenon is referred to as elastic

or Rayleigh scattering. In a very few cases, the molecule changes its vibrational state upon interaction with the incident photon and the photons are scattered at a different frequencies from that of the incident photon (Figure 6.10). This process is referred to as inelastic scattering or the Raman effect, named after Sir C.V. Raman.

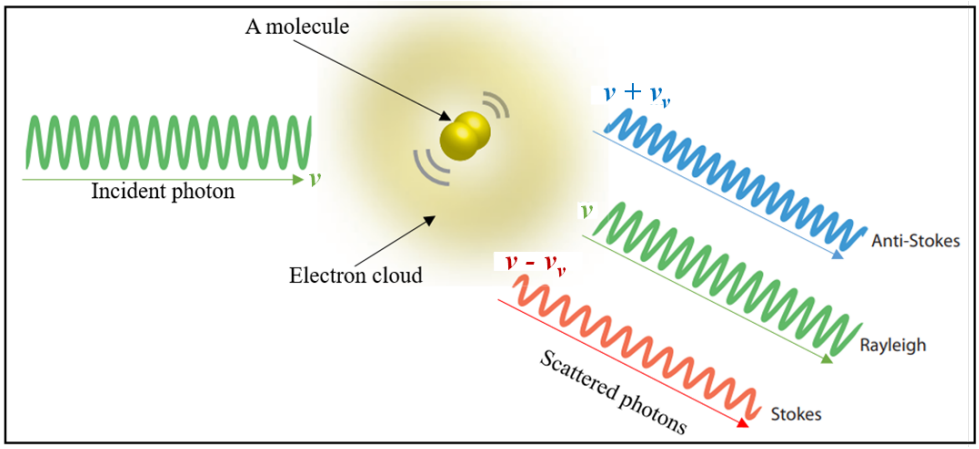

Figure 6.10: Rayleigh (elastic) and Raman (inelastic) scattering from a molecule. Adapted from [33]

In the Stokes scattering case, the initial state is the ground state, and after the scattering process, the molecule is in excited vibrational state (the scattered photon has lower energy compared to the incident photon) [33]. In the case of anti-Stokes, the molecule was already in an excited vibrational state and returns to the ground state during the scattering process (the scattered photon has higher energy compared to the incident photon).

Interaction of light with a molecule can induce a deformation of its electron cloud. This deformation is known as a change in polarizability [34]. Raman spectroscopy looks at changes in polarizability of molecular bonds. Molecular

bonds have specific energy transitions in which a change of polarizability occurs, giving rise to Raman active modes.

When light is scattered by a molecule (Figure 6.10), the time-dependent electric field component E of the incident electromagnetic wave distorts the electron cloud of the molecule, which induces an electric dipole moment. This distortion occurs because the molecule experiences the incident radiation as an oscillating electric field due to the considerably smaller size of the molecule compared to typical wavelength of Raman excitation in the visible part of the electromagnetic spectrum (400-700 nm) [33]. The induced dipole moment μ, is directly proportional to the electric field intensity E according Equation 6.24 [34].

$$\mu = \alpha E \tag{6.24}$$

where α is the constant of proportionality, called the polarizability. It is the measure of deformability of the electron cloud of the molecule by the electric field. For any molecular vibration to be Raman active, such vibration must be accompanied by a change in the polarizability of the molecule.

The oscillating electric field E of the electromagnetic radiation in close interaction with the molecule is a time dependent function, defined by Equation 6.25 [33], [34]:

$$E = E_o \cos 2\pi v t \tag{6.25}$$

where E_o is a constant, the maximum value of the electric field, v is the frequency of the radiation, and t is time. The oscillating electric field E will

induce in the molecule an oscillating dipole moment μ whose frequency will be the same as that of the external electric field. Putting Equation 6.25 into Equation 6.24, yields:

$$\mu = \alpha E_o \cos 2\pi v t \tag{6.26}$$

In molecular vibration, the polarizability α is not constant because certain vibrations and rotations cause α to vary. For instance, during the vibration of a diatomic molecule, the molecular shape is alternately under compression and tension [34], like a spiral spring. Since the election cloud is not identical at the extremes of the vibration, this results in a change in the polarizability α. For small displacements the polarizability α can be expanded in a Taylor series as defined by Equation 6.27 [33], [34]:

$$\alpha = \alpha_o + \frac{\partial \alpha}{\partial Q} Q + \cdots \tag{6.27}$$

where α_o is the equilibrium polarizability, $\frac{\partial \alpha}{\partial Q}$ is the rate of change of polarizability with respect to Q measured at the equilibrium configuration and Q is the displacement of the molecule in vibration mode about its equilibrium configuration. Q is also time dependent defined by [33], [34]:

$$Q = Q_o \cos 2\pi v_v t \tag{6.28}$$

where v_v is the frequency of the displacement Q and Q_o is a constant, the maximum value for Q. Putting Equation 6.28 into 6.27, and ignoring the

higher order of the expansion, yields:

$$\alpha = \alpha_o + \frac{\partial \alpha}{\partial Q} Q_o \cos 2\pi v_v t \tag{6.29}$$

Putting Equation 6.29 into 6.26, yields:

$$\mu = \alpha_o E_o \cos 2\pi v t + \frac{\partial \alpha}{\partial Q} Q_o E_o \cos 2\pi v t \cos 2\pi v_v t \tag{6.30}$$

Applying a trigonometric identity, Equation 6.30 becomes [33], [34]:

$$\mu = \alpha_o E_o \cos 2\pi v t + \frac{\partial \alpha}{\partial Q} \frac{Q_o E_o}{2} [\cos 2\pi (v - v_v) t + \cos 2\pi (v + v_v) t] \tag{6.31}$$

It can be seen from Equation 6.31 that the induced dipole moment μ varies with three component frequencies v, $v - v_v$ and $v + v_v$ (Figure 6.10), which correspond to the elastic scattering (Rayleigh scattering), Stokes (Raman scattering) and anti-Stokes (Raman scattering), respectively.

6.6.2 Raman setup and measurement

A Raman spectrometer is composed of monochromatic light source (usually a laser source), monochromator, sample holder and detector [28]. Several types of lasers can be used as the excitation source, like krypton (530.9 and 647.1 nm), He and Ne (632.8 nm), Nd (1064 nm and 532 nm), argon (488.0 and 514.5 nm) [35].

The Raman spectroscopy used in this study is a Horiba Jobin-Yvon T64000 spectrometer with an argon-krypton laser of an excitation source with a laser of wavelength of 514.5 nm and power of 148 mW. To record a Raman spectrum

of samples, a laser beam in the ultraviolet, visible or near infrared region is illuminated on the samples. The scattered photons can be harvested with the aid of lens and sent through a monochromator to obtain the Raman spectrum of the analytes. The sensitivity of the Raman instrument to the Raman scattering can be improved by the use of notch filters. Multi-channel detectors such as the charged coupled devices [33] are normally used to improve the sensitivity of the detection system used in Raman measurements. This technique is relatively easy to use. It does not require any special sample preparation. Depending on the range of analysis selected, it takes between 15 - 25 minutes to completely measure a sample. The spectra were obtained for Raman shifts between 200 cm^{-1} and 1800 $^{-1}$. The system is equipped with Labspec 5 software for analysis of the Raman spectra.

6.7 Scanning electron microscopy

A scanning electron microscope (SEM) is a microscope that uses electrons rather than light to form an image of objects on a very fine scale [36]. In SEM the technique, a beam of electrons is focus on a specimen to create a highly-magnified image of it. This technique has been used in diverse applications such as the analysis of surface morphology and microstructure evolution of thin films.

The interactions between the incident electrons and electrons of the specimen resulted in both elastic and inelastic scatterings. Some of the incident

electrons transfer their energies to the target atoms, thereby scattering with reduced energy [36]. Elastic scattering results from the deflection of the incoming electrons by the atomic nucleus of the specimen. Backscattered electrons (BSE) resulted from the elastic collision between incident beam and target atoms. BSEs are high-energy electrons which were reflected off the target sample, shown in Figure 6.11. BSE contributes a useful signal for imaging formation, because it possesses higher energy than SE and give information from deeper regions on the sample. The inelastic collisions between the in-

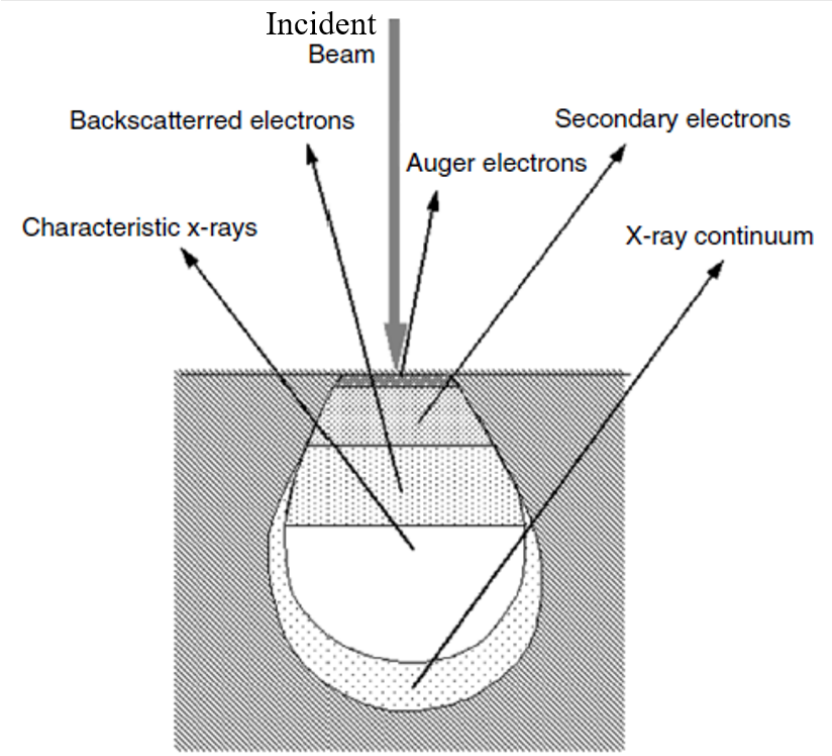

Figure 6.11: Schematic of several signals generated by the electron beam-sample interactions in SEM and the regions from which the signals can be detected [36]

coming electrons and the target atoms produce the secondary electrons (SE),

which in turn can create secondary electrons. SEs have less energy compared to the BSEs [37]. Surface topography of samples are studied by the signals from SEs. Due to their low energy, only SEs which are located near the surface can exit the sample and be examined, others due to their low energy, are absorbed by the sample [38]. Other signals created in addition to SEs include the characteristic X-rays, Auger electrons (Figure 6.11).

6.7.1 SEM configuration

Shown in Figure 6.12 is an electron column of a conventional SEM. The electron gun at the top of the column, creates the primary electrons and accelerates them to an energy level of 0.1-30 keV [36], [39]. Modern SEM systems demand that the electron gun creates a stable electron beam with high current, small spot size, adjustable energy, and small energy dispersion. There are many types of electron guns used in the SEM system. The first generation SEMs generally used tungsten or lanthanum hexaboride (LaB_6) cathodes, while in modern SEMs, the use of field emission sources are well established. Once these electrons are accelerated, a moderate vacuum allows electrons to move freely from the electron beam source to the sample and then to the detectors [40]. Scanning coils comprise of a number of electromagnetic lenses that focus the beam to create a small, focused electron probe on the sample surface with beam spot size of less than 10 nm in diameter. Usually, the depth of the electron beam interactions with the specimen is, approximately 1 μm but this depends on electron energy and sample characteristics [41].

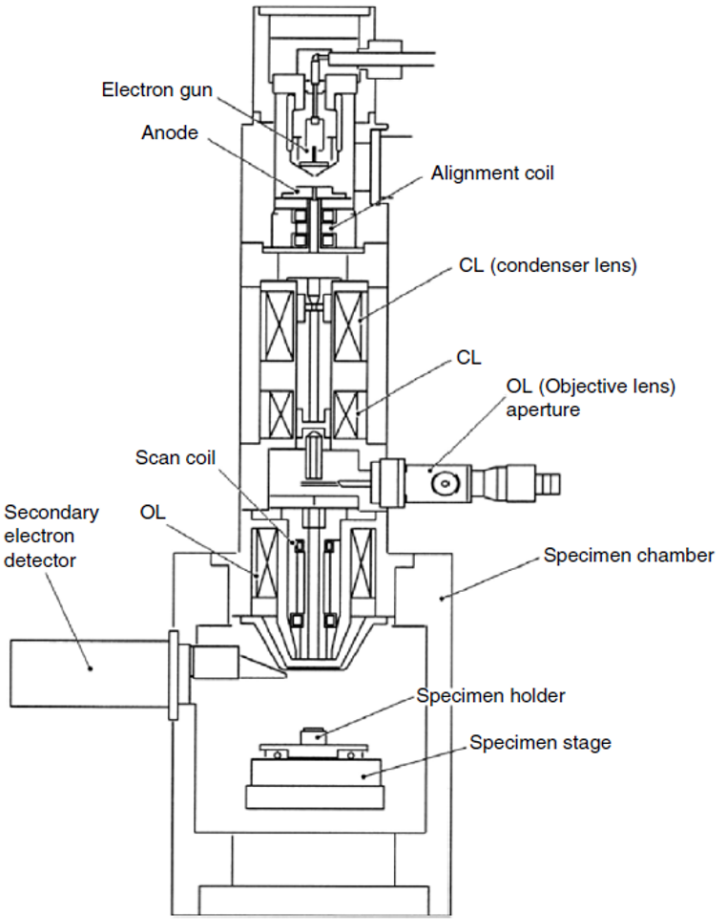

Figure 6.12: Schematic diagram of a scanning electron microscope [36]

6.7.2 SEM setup and measurement

The typical SEM components are the electron column, scanning system, detectors, display, vacuum system and electronic controls. In this study, a Zeiss Ultra 55 field emission scanning electron microscope was used to examine the samples surface morphology. This optical instrument is equipped with a field emission electron gun (FEG). The FEG is made up of tungsten wire of sharp tip with a small radius of less than 100 nm. If the electric field intensity

reaches about 10 V/nm [21] at the tip, electrons are emitted. This microscope is equipped with SE, BE and in-lens SE detectors. In this study, in order to focus on the near surface area of the samples, SEM images of the samples surfaces were taken at beam energies of 2 kV at various magnifications.

6.8 X-ray diffraction

X-ray diffraction technique belongs to a family of non-invasive analytical techniques. It is capable of revealing information about the crystallographic structure, chemical composition and physical properties of materials and thin films being analyzed [42]. This technique is based on observing the scattered intensity of an X-ray beam hitting a sample as a function of incident and scattered angles, and the wavelength. X-Rays are electromagnetic radiation of exactly the same nature as light, but of very much shorter wavelength. X-ray diffraction technique allows for both qualitative and quantitative analyses [43]. Qualitative analysis is applied for identification of phases in a specimen by comparison with the reference patterns. Quantitative analysis determines the structural characteristics and phase proportions with numerical precision.

X-rays are produced when electrons with energy in the range 10-40 keV [44] interact with the metal targets. The maximum energy of the X-ray photons produced is limited by the energy of incident energy. Metals such as Cu, Cr, Fe, Co and Mo are used as the anode [44]. Most common X-ray tubes are made of Cu anodes which emit a radiation (Kα) with a wavelength of 1.5406 Å

[45]. When a monochromatic X-ray beam with wavelength λ is focused onto a crystalline material at an angle θ, the diffraction of the beam is possible if the following condition is fulfilled: the distance travelled by the X-rays reflected from successive planes differs by integer multiple of the wavelength of the radiation (Figure 6.13).

The atoms in the crystal lattice are arranged in a fairly regularly repeated pattern, so that, the X-rays diffracted beam can constructively interfere. These conditions were proposed by Sir William Lawrence Bragg in 1912, which is popularly known as Bragg's law [44]. In Figure 6.13, the ray BAY leads ray BA'Y by the amount of path-length $(n\lambda)$ [46], which is geometrically given by:

$$n\lambda = BA' + A'D = d\sin\theta + d\sin\theta \tag{6.32}$$

This leads to the Bragg's law of diffraction [44], [46]:

$$n\lambda = 2d\sin\theta \tag{6.33}$$

where n is any positive integer, λ is the wavelength of the X-ray, d is the spacing between crystal planes and θ is the diffraction angle from the plane (hkl) [47]. XRD experiments are performed at a fixed wavelength, therefore from Equation 6.33 the measurement of the diffraction angles allow for calculation of the associated d-spacing. For crystalline materials with cubic structures, the lattice parameter (a) is given by [46]:

$$a = \frac{d_{hkl}}{\sqrt{h^2 + k^2 + l^2}} \tag{6.34}$$

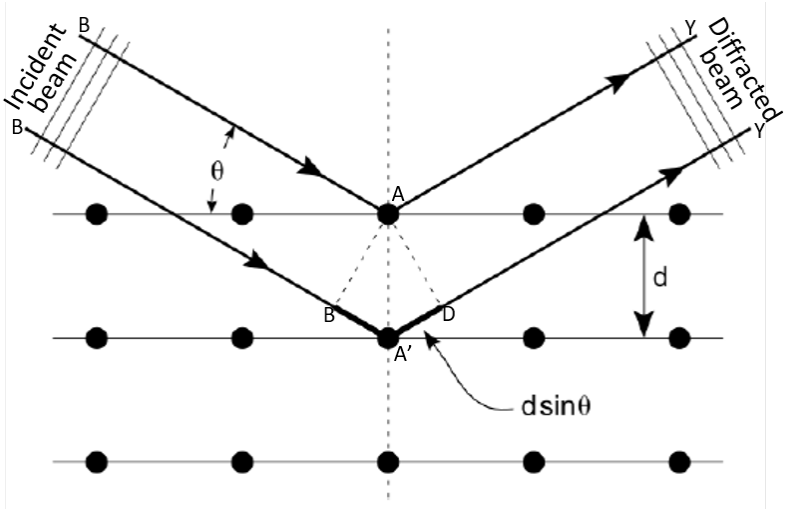

Figure 6.13: Schematic of X-ray interaction with crystal planes. Adapted from [46]

where *hkl* are the Miller indices for the (*hkl*) plane. Equations 6.33 and 6.34 can be used to determine the crystal structure of a material, if the peaks of the diffraction pattern are correctly indexed.

6.8.1 Crystal size determination from XRD peak broadening

The XRD peak broadening is dependent on three major factors [48]: (i) crystallite size of the material, (ii) instrumental contributions to peak broadening and (iii) strain in the material. If the strain in material is negligible, peak broadening can be used to estimate crystallite size, provided that proper correction is made for the instrumental broadening. It has been established that XRD peak broadening decreases with increase in the crystallite sizes [49].

Consider the schematic graphs of diffracted intensities vs. 2θ of the forms shown in Figure 6.14. Illustrated by Figure 6.14 (a) is a diffraction pattern from a material with a very small crystallite size in contrast to Figure 6.14 (b),

which depicts a pattern from a pure crystalline material with large crystallite size. Both are hypothetical case of diffraction occurring only at the exact Bragg angle θ_B. The width of the diffraction pattern in Figure 6.14 (a) increases as the thickness l of the crystal size decreases. In this figure, B is the full width at half maximum (FWHM) usually measured, in radians.

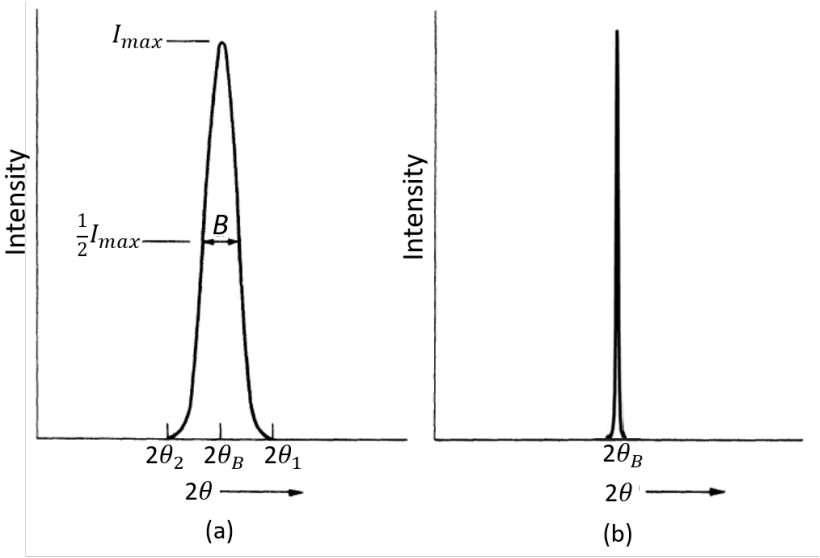

Figure 6.14: Schematic of effect of crystal size on diffraction patterns (a) small crystal size (b) big crystal size. Adapted from [48]

As a rough measure of B, we can take half the difference between the two extreme angles at which the intensity is zero [48]. That is:

$$B = \frac{1}{2}(2\theta_1 - 2\theta_2) = \theta_1 - \theta_2 \tag{6.35}$$

The path-difference equations for these two angles are given by [48]:

$$(n+1)\lambda = 2l\sin\theta_1 \tag{6.36}$$

$$(n-1)\lambda = 2l\sin\theta_2 \tag{6.37}$$

By subtracting Equation 6.37 from 6.36, it follows that:

$$\lambda = l(\sin\theta_1 - \sin\theta_2) \tag{6.38}$$

Applying trigonometric identity to Equation 6.38, yields:

$$\lambda = 2l\cos\left(\frac{\theta_1+\theta_2}{2}\right)\sin\left(\frac{\theta_1-\theta_2}{2}\right) \tag{6.39}$$

But θ_1 and θ_2 are both very nearly equal to θ_B, so that $\theta_1 + \theta_2 \approx 2\theta_B$ and $\sin\left(\frac{\theta_1-\theta_2}{2}\right) \approx \left(\frac{\theta_1-\theta_2}{2}\right)$ [48]. Substituting these into Equation 6.39 yields:

$$\lambda = 2l\left(\frac{\theta_1-\theta_2}{2}\right)\cos\theta_B \tag{6.40}$$

And finally, applying Equation 6.35 in 6.40 and rearranging, yields:

$$l = \frac{\lambda}{B\cos\theta_B} \tag{6.41}$$

An exact treatment of Equation 6.41 yields Equation 6.42 [48], which is the introduction of a dimensionless shape factor k. The shape factor has a typical value of about 0.9, but varies with the actual shape of the crystallites [48]:

$$l = \frac{k\lambda}{B\cos\theta_B} \tag{6.42}$$

Equation 6.42 is known as the Scherrer formula, where k is the Scherrer constant. Equation 6.42 is often used to estimate the crystallite size of materials

from the calculated FWHM of XRD patterns. B can be corrected for instrumental broadening using Equation 6.43 [48]:

$$B = \sqrt{(B_m)^2 - (B_i)^2} \tag{6.43}$$

where B_m is the measured FWHM (in radians) from the intensity peak of the analyte while B_i is the instrumental broadening, given by the relation [50], [51]:

$$B_i = \tan^{-1}\left(\frac{W_R}{R_G}\right) + 2\left(\frac{\Delta\lambda}{\lambda}\right)\tan\theta \tag{6.44}$$

where W_R is the receiving slit width, R_G is the radius of goniometer and $\Delta\lambda$ is resolution of the diffractometer.

6.8.2 XRD setup and measurement

A popular technique for analysing thin films is the use of the grazing incidence angle geometry, known as grazing incidence XRD (GIXRD). This geometry which is a slight modification of conventional Bragg-Brentano geometry is attained by making the X-rays strike the sample surface at a very small incident angle (typically, θ=1-5°) [52] while the detector on the 2θ axis scans the XRD pattern.

Thin films possess peculiar properties which are essentially different from the corresponding bulk materials. This is due to their altered physical dimensions and microstructure compared to the bulk ones. Many techniques based on the applications of X-ray such as X-ray reflectivity (XRR) have been

used to probe the structure of materials including thin films. X-ray diffraction techniques have played a leading role in this aspect.

In this study, thin film characterization by GIXRD was done at Radio-Analysis Laboratory of the South Africa Nuclear Energy Corporation. The GIXRD analyses were performed on the samples using the D8 Advanced diffractometer system. The X-ray tube employed was a Cu anode which emits radiation (Kα) with wavelength of λ = 1.5406 Å. The X-ray measurement was done with the gionometer in locked couple configuration while the diffractometer collect the diffracted beam at two-theta range of 10 - 100° with step size of 0.04° and average time per step size kept at 3 s. This gave a measurement time of about 112 min for each sample. The incident beam for GIXRD analysis was maintained at a low grazing angle of 1° relative to the surface of the sample.

To ensure easy comparison of the obtained XRD results with the standard diffraction files, the database from the International Centre for Diffraction Data files (ICDD-PDF-2) were used. Chapter 7 presents the results obtained in this study and the analysis therein.

6.9 Atomic force microscopy

An atomic force microscopy (AFM) is a technique used in surface science for surface morphology characterization. This technique forms the topographic image of surface at a high resolution of 1 nm [53]. As nondestructive tools,

AFMs have popular applications for investigating the surface morphologies of many materials ranging from thin films to organic cells [54]. The ability of an AFM to characterize the surface morphology relies on exerting a force with its movable tip [55] on the surface atoms of the sample.

The principle of operation of an AFM is based on the interatomic potential [56]. The sharp tip of an AFM is fixed to the end of spring cantilever. When the tip is brought very close (within interatomic separation distance) to the sample surface, interatomic potential develop between the atoms of the tip of AFM and surface atoms of the sample [56]. As the sharp tip moves across the sample surface (Figure 6.15), the interatomic potential cause the cantilever to bounce up and down in respond to change in roughness of the sample surface. The topographic features of the sample surface are mapped out by

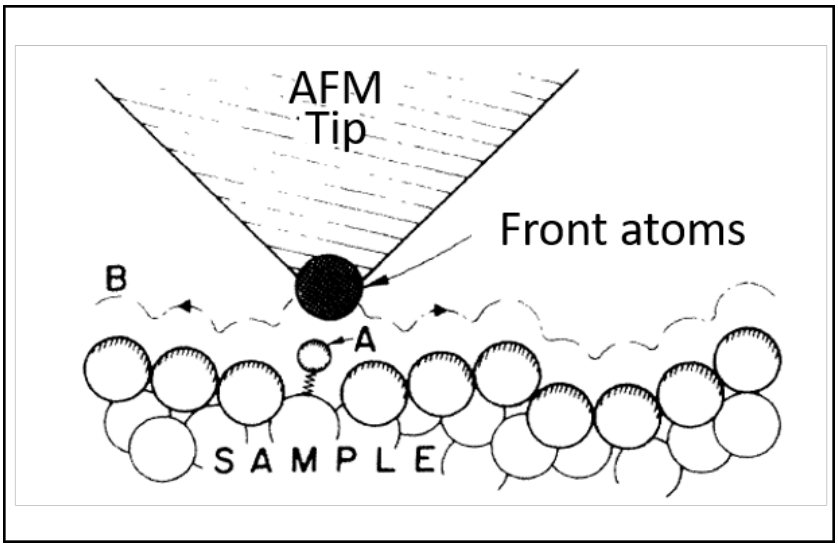

Figure 6.15: Description of the principle of operation of an AFM. The tip follows contour B, to maintain constant force between the AFM tip and the sample's surface atoms [53]

measuring the deflections of the cantilever. The force exerted between atoms on the sample surface and atoms on AFM tip is measured by a laser and a detector. A 3D image is constructed by recording the cantilever motion in the z-direction as a function of sample's x and y positions [56]. AFM analysis provides in addition to information on surface morphology, the quantitative roughness value and grain size.

6.9.1 AFM setup and measurement

The samples were mounted on metal plates using a glue. The AFM images were obtained using the Dimension Icon AFM system. It works in contact mode using a sharp nitride lever (SNL) tip with a spring constant of 0.30 N/m. The SNL probe has resonant frequency ranging from 40 to 75 kHz. The AFM probe has a tip radius of 2 nm, the scan rate used for samples analysis was 0.3 Hz. This AFM setting was maintained for the analysis of all the samples. The AFM images obtained were analysed using NanoScope Analysis (Bruker, USA) software.

REFERENCES

[1] Hochtemperatur-Werkstoffe GmbH, Germany, *Properties of glassy carbon*, http://htw-germany.com/technology.php5?lang=en&nav0=2&nav1=16, Accessed: October 28, 2019.

[2] Sigma-Aldrich Pty Ltd, South Africa, *Tungsten sputtering target*, https://www.sigmaaldrich.com/catalog/product/aldrich/767522?lang=en&region=ZA, Accessed: August 22, 2018.

[3] J. E. Mahan, *Physical vapor deposition of thin films*. Wiley, Verlag Chemie Weinheim, Germany, 2000, p. 336.

[4] M Ohring, "Materials science of thin films: Deposition and structure, academic press," *San Diego, CA*, 2002.

[5] Materials science Inc., San Diego, *Magnetron sputtering*, http://www.msi-pse.com/magnetron_sputtering.htm, Accessed: June 12, 2019.

[6] P. J. Kelly and R. D. Arnell, "Magnetron sputtering: A review of recent developments and applications," *Vacuum*, vol. 56, no. 3, pp. 159–172, 2000.

[7] Kurt J. Lesker Company, Jefferson Hills, PA 15025 USA, *The effect of sputter cathode design on deposition parameters: Design enhancements expand capabilities for the magnetron sputtering of thin films*, https://www.lesker.com/newweb/blog/post.cfm/the-effect-of-sputter-cathode-design-on-deposition-parameters-design-enhancements-expand-capabilities-for-the-magnetron-sputtering-of-thin-films, Accessed: December 8, 2019.

[8] D. M. Mattox, *Handbook of physical vapor deposition (PVD) processing, film formation, adhesion, surface preparation and contamination control*. Noyes Publications, Westwood, New Jersey, USA., 1998.

[9] K. L. Chopra, *Thin film phenomena*. McGraw-Hill, New York, USA, 1969.

[10] V. Guilbaud-Massereau, A. Celerier, and J. Machet, "Study and improvement of the adhesion of chromium thin films deposited by magnetron sputtering," *Thin Solid Films*, vol. 258, no. 1-2, pp. 185–193, 1995.

[11] J. A. Thornton and D. W. Hoffman, "Internal stresses in titanium, nickel, molybdenum, and tantalum films deposited by cylindrical magnetron sputtering," *Journal of vacuum science and technology*, vol. 14, no. 1, pp. 164–168, 1977.

[12] W. D. Callister and D. G. Rethwisch, *Materials science and engineering: An introduction*. John wiley & sons, New York, 2007.

[13] Agilent Technologies, Inc., United States, *Agilent data acquisition unit: User's guide*, http://www.me.umn.edu/courses/me4331/FILES/Agilent34970A-UsersGuide.pdf, Accessed: July 15, 2019.

[14] E. G. Njoroge, "PhD thesis, University of Pretoria, Hatfield," 2014.

[15] C. Wei-Kan, J. Mayer, and M. Nicolet, *Backscattering spectrometry*. Academic Press, New York, 1978.

[16] L. Feldman, "Applications of ion beams to materials science," in *Interaction of charged particles with solids and surfaces*, Springer, London, 1991, pp. 309–311.

[17] W. Chu, J. Mayer, M. Nicolet, T. M. Buck, G. Amsel, and F. Eisen, "Principles and applications of ion beam techniques for the analysis of solids and thin films," *Thin Solid Films*, vol. 17, no. 1, pp. 1–41, 1973.

[18] J. Tesmer, M. Nastasi, J. Barbour, C. Maggiore, and J. Mayer, *Handbook of modern ion beam materials analysis*. Materials Research Society, Pittsburgh, USA, 1995.

[19] H. H. Andersen, "Accelerators and stopping power experiments," in *Interaction of Charged Particles with Solids and Surfaces*, Springer, New York, 1991, pp. 145–192.

[20] B. Brijs, J. Deleu, C. Huyghebaert, S. Nauwelaerts, K Nakajima, K Kimura, and W. Vandervorst, "Advanced rbs analysis of thin films in micro-electronics," in *AIP Conference Proceedings*, AIP, vol. 576, 2001, pp. 470–475.

[21] T. T. Hlatshwayo, "PhD thesis, University of Pretoria, Hatfield," 2010.

[22] W. Chu and J. Liu, "Rutherford backscattering spectrometry: Reminiscences and progresses," *Materials chemistry and physics*, vol. 46, no. 2-3, pp. 183–188, 1996.

[23] M. Mayer, "Rutherford backscattering spectrometry (RBS)," in *Workshop on Nuclear Data for Science and Technology: Materials Analysis*, vol. 34, 2003.

[24] D. Karolina, "PhD thesis, Technische Universitat, Darmstadt," 2013.

[25] L. R. Doolittle, "Algorithms for the rapid simulation of Rutherford backscattering spectra," *Nuclear Instruments and Methods in Physics Research Section B: Beam Interactions with Materials and Atoms*, vol. 9, no. 3, pp. 344–351, 1985.

[26] J Padayachee, K. Meyer, and V. Prozesky, "Automatic analysis of Rutherford backscattering spectrometry spectra," *Nuclear Instruments and Methods in Physics Research Section B: Beam Interactions with Materials and Atoms*, vol. 181, no. 1-4, pp. 122–127, 2001.

[27] J. Ziegler, J. Biersack, and U. Littmark, *Empirical stopping powers for ions in solids*. IBM Research Report RC9250, 1982.

[28] P. Rostron, S. Gaber, and D. Gaber, "Raman spectroscopy, review," *International Journal of Engineering and Technical Research*, vol. 6, pp. 50–64, 2016.

[29] A. Smekal, "The quantum theory of dispersion," *Naturwissenschaften*, vol. 11, no. 43, pp. 873–875, 1923.

[30] J. Laserna, "An introduction to raman spectroscopy: Introduction and basic principles," *Raman/Infrared Spectroscopy*, pp. 1–6,

[31] A. H. Compton, "A quantum theory of the scattering of x-rays by light elements," *Physical review*, vol. 21, no. 5, pp. 483–502, 1923.

[32] C. V. Raman and K. S. Krishnan, "The optical analogue of the Compton effect," *Nature*, vol. 121, no. 3053, p. 711, 1928.

[33] L. Opilik, T. Schmid, and R. Zenobi, "Modern Raman imaging: Vibrational spectroscopy on the micrometer and nanometer scales," *Annual Reviews of Analytical Chemistry*, pp. 379–398, 2013.

[34] N. Colthup and D. Lawrence, *Introduction to infrared and Raman spectroscopy*. Academic Press, New York, 2012.

[35] J. Ferraro, K. Nakamoto, and C. Brown, *Introductory Raman spectroscopy*. Academic Press, San Diego, 2003.

[36] W. Zhou and Z. L. Wang, *Scanning microscopy for nanotechnology: Techniques and applications*. Springer science & business media, New York, 2007.

[37] B. Hafner, "Scanning electron microscopy primer," *Characterization Facility, University of Minnesota-Twin Cities*, pp. 1–29, 2007.

[38] E. C. Stefanaki, "Electron microscopy: The basics," *Physics of Advanced Materials, Winter School*, pp. 1–11, 2008.

[39] R. F. Egerton, *Physical principles of electron microscopy*. Springer, New York, 2005.

[40] M. T. Postek, "Critical issues in scanning electron microscope metrology," *Journal of Research-National Institute of Standards and Technology*, vol. 99, pp. 641–641, 1994.

[41] W. Nixon, "The general principles of scanning electron microscopy," *Philosophical Transactions of the Royal Society*, vol. 261, no. 837, pp. 45–50, 1971.

[42] P. F. Fewster, "X-ray analysis of thin films and multilayers," *Reports on Progress in Physics*, vol. 59, no. 11, pp. 1339–1407, 1996.

[43] M. Birkholz, *Thin film analysis by x-ray scattering*. John Wiley & Sons, New York, 2006.

[44] J. I. Langford and D. Louer, "Powder diffraction," *Reports on Progress in Physics*, vol. 59, no. 2, pp. 131–234, 1996.

[45] G. Holzer, M. Fritsch, M. Deutsch, J. Hartwig, and E. Forster, "K(α 1, 2) and K(β 1, 3) x-ray emission lines of the 3 d transition metals," *Physical Review A*, vol. 56, no. 6, pp. 45–54, 1997.

[46] H. P. Klug and L. E. Alexander, *X-ray diffraction procedures: For polycrystalline and amorphous materials*. John Wiley and Sons, New York, 1974.

[47] D. Naumann and R. Meyers, *Encyclopedia of analytical chemistry*. John Wiley & Sons, Chichester, UK, 2000, pp. 102–131.

[48] B. D. Cullity and S. R. Stock, *Elements of x-ray diffraction*. Addison-Wesley Publishing company Inc, Massachusetts, 1956.

[49] K. Venkateswarlu, A. C. Bose, and N. Rameshbabu, "X-ray peak broadening studies of nanocrystalline hydroxyapatite by Williamson–Hall analysis," *Physica B: Condensed Matter*, vol. 405, no. 20, pp. 4256–4261, 2010.

[50] B. Mallick, "X-ray diffraction analysis of polymeric solid using bragg-brentano geometry," *Int. J. Mater. Chem. Phys*, vol. 1, pp. 265–270, 2015.

[51] T. Ida and K. Kimura, "Flat-specimen effect as a convolution in powder diffractometry with bragg–brentano geometry," *Journal of applied crystallography*, vol. 32, no. 4, pp. 634–640, 1999.

[52] R. Tarey, R. Rastogi, and K. Chopra, "Characterization of thin films by glancing incidence x-ray diffraction," *The Rigaku Journal*, vol. 4, no. 1, pp. 11–15, 1987.

[53] G. Binnig, C. F. Quate, and C. Gerber, "Atomic force microscope," *Physical review letters*, vol. 56, no. 9, pp. 930–933, 1986.

[54] N. Martin, C. Rousselot, D. Rondot, F. Palmino, and R. Mercier, "Microstructure modification of amorphous titanium oxide thin films during annealing treatment," *Thin solid films*, vol. 300, no. 1-2, pp. 113–121, 1997.

[55] H. K. Wickramasinghe, "Scanned-probe microscopes," *Scientific American*, vol. 261, no. 4, pp. 98–105, 1989.

[56] R. Jagtap and A. Ambre, "Atomic force microscopy (AFM): Basics and its important applications for polymer characterization: An overview," *Journal of Polymer Materials*, vol. 22, no. 1, pp. 1–26, 2005.

CHAPTER

SEVEN

RESULTS AND DISCUSSION

7.1 Introduction

This chapter presents the results of the solid state interactions between glassy carbon and tungsten, which formed the diffusion couples. This study focuses on the interface interactions between glassy carbon and the tungsten films, under the influence of annealing temperatures. The main analytical technique in this study is Rutherford backscattering spectrometry (RBS). Results presentation and discussion begin with the results obtained from this technique. The compound phases formed in the reaction zone of the diffusion couples were predicted from the RUMP simulation of the RBS results. These phases were positively identified with the help of GIXRD technique.

The microstructure of glassy carbon, was also investigated with XRD and Raman techniques, in a bid to monitor its structural changes under the influences of heat treatment and highly charged ions (HCI) irradiation. The

suitability of XRD for structural analysis was harnessed, to particularly study the microstructure of glassy carbon in terms of its amorphous fraction content.

7.2 RBS energy calibration

The RBS measurements were done according to the procedure and experimental parameters outlined in subsection 6.5.5. The analysis of all the RBS results began with energy calibration. The parameters obtained from this exercise, are vital for accurate simulation of the RBS results with the RUMP code. The section that follows is devoted to the typical energy calibration procedure, carried out after every RBS measurement before the actual simulation is done. Fluctuation in the RBS measurements is a common phenomenon. It is largely associated with both systematic, statistical and human errors. One important contributor to the statistical error is the unstable nature of the beam current, especially when the Helium gas pressure is low.

Energy calibration shows the relationship between the energy of the backscattered of ions and the channel numbers. To estimate the energy per channel, the RBS results of all samples measured on the same day were used to ensure better results. Elements commonly present in such samples in addition to W in my samples are Si, Ru, and Zr, present in the samples of other colleagues. The process of calibration began with extraction of the surface channel position of these elements from their respective RBS spectra. With

the knowledge of the incident beam energy of 1.6 MeV, the kinematic factors of these elements were evaluated using Equation 6.7 in subsection 6.5.1. Thereafter, their respective surface energies were calculated. For a typical RBS result, the plot of energy of the detected backscattered ions versus channel number gives a linear graph shown in Figure 7.1. The slope of this graph and

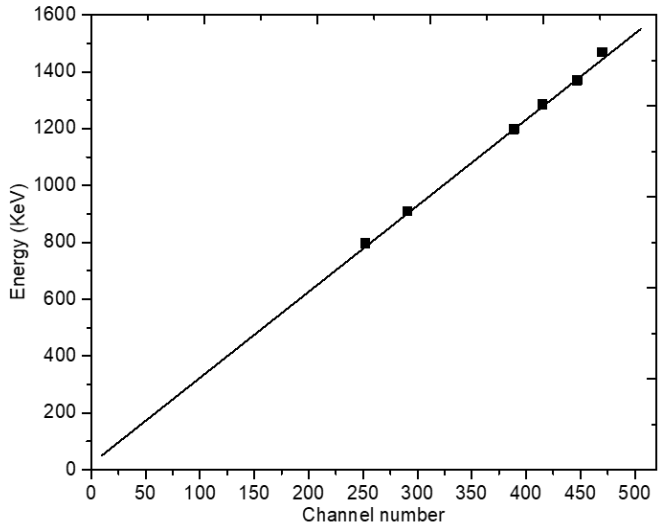

Figure 7.1: A typical energy calibration graph for the acquired RBS spectra

intercept on the vertical axis were estimated to be 3.03 keV/Ch. and 29.69 keV, respectively. These values from calibration are typical of RBS measurements for a particular day. There is always an inevitable error in the RBS measurements due to systematic, statistical and human errors. These sources of error in measurement introduce slight change to the values of these parameters each time RBS measurement is done. Thus, energy calibration is a necessary step for every RBS analysis before the actual simulation.

7.3 Thermal annealing of W films deposited on GC

7.3.1 RBS results of as-deposited samples

The RUMP simulations of all the RBS spectra were also carried out to monitor the intermixing between W and glassy carbon (C) atoms for all the samples annealed at temperatures of 400-1000 °C. The RBS/RUMP simulated spectrum of the as-deposited sample is shown in Figure 7.2. The red line denotes the simulated spectrum while the black one is the experimental RBS result.

The scattering events from W and glassy carbon are clearly separated in energy. The W signal appeared at 1.47 MeV while the glassy carbon signal appeared at a lower energy of 0.40 MeV. The latter was due to both scattering kinetics and the energy loss of the backscattered He^+ ions, during their inward and outward paths. The arrows at channel numbers 473 and 115 indicate the surface positions of W and C, respectively. If the glassy carbon were present at the surface with W film, its signal would have appeared at the higher energy edge, indicated by the arrow in Figure 7.2. This means that the surfaces of the glassy carbon substrates were completely covered by deposited W films. Furthermore, the signal yield between the W back edge and C front edge is approximately at zero level. This indicates absence of substantial amount of impurities within this energy range.

The simulated spectrum overlaps the RBS measured spectrum very well, especially in the region of the tungsten signal, where the simulated and measured spectra are difficult to distinguish from each other. But at the lower

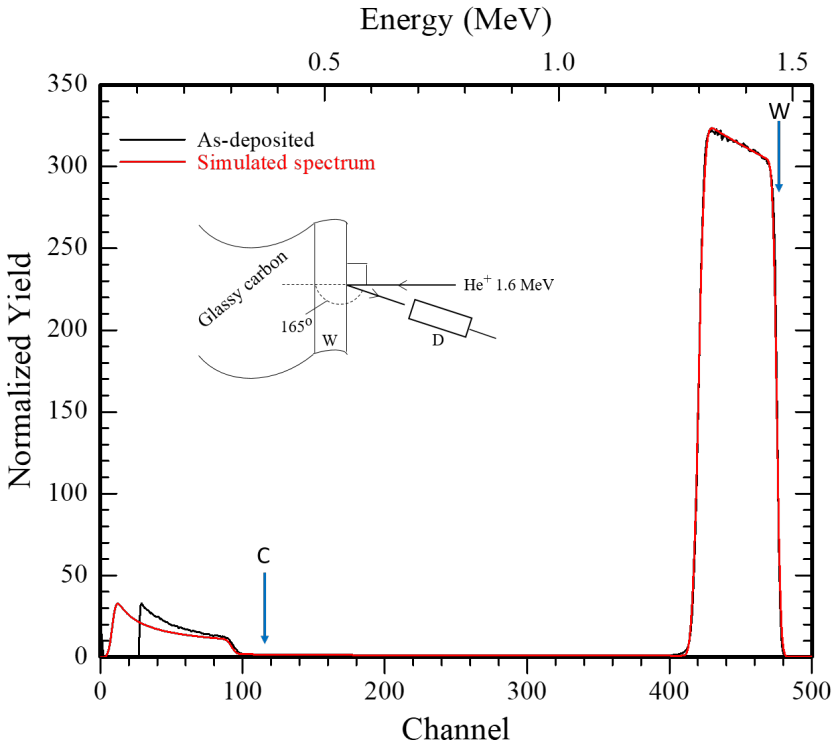

Figure 7.2: The RBS spectrum of as-deposited sample (black) and RUMP simulated spectrum (red). Included in the figure is the experimental geometry

energy channels of the carbon peak, it is difficult to achieve a good fit. This fitting problem at the low energy tail of the RBS plot is typical of this analytical method. Wang and Jacob [1], attributed this problem to the increasing background as a result of multiple scattering [2] from the overlaying W film which is not quantitatively reproduced in the RUMP simulation program. Multiple scattering caused the traversing ions to possess reduced energy. This in turn produced a high scattering cross section, which resulted in high yields at the low energy tail. The effect of multiple scattering is common with layers of heavy elements and increases with the layer thickness. The thickness of W film deposited on the glassy carbon substrate was estimated as 726.8×10^{15}

at./cm^2 (i.e. $\sim$115.2 nm), bulk density was assumed for the W thin films.

7.3.2 RBS results of the annealed samples

The fit obtained from the as-deposited sample was coherently maintained in the simulations of the annealed samples. The simulated results of samples annealed isothermally from 400-700 °C for duration up to 24 h showed that there was no sign of intermixing of atoms between the two materials in this temperature range. Their simulated spectra (not shown here) were similar to that of the as-deposited sample presented in Figure 7.2. For samples annealed at 800 °C, the RUMP simulated results showed that intermixing between the W and glassy carbon atoms started at this temperature, and it increased progressively with annealing duration as presented in Figure 7.3. The result from RUMP simulation for the sample annealed at 800 °C for 30 min, showed that there was an intermixed layer of thickness 6.32×10^{15} at./cm^2. In the sample annealed at 800 °C for 60 min, the thickness of intermixed layer was 8.64×10^{15} at./cm^2 (simulated spectra not shown here). At 800 °C for 120 min, the simulated result showed that the intermixed layer widened to 13.96×10^{15} at./cm^2. This was an indication that, the annealed temperature was not high enough to trigger a substantial interface mixing, which could lead to phase formation in the diffusion couples.

Figure 7.4 shows the spectra of the samples annealed at 900 °C for 60 min, 120 min and 180 min. Noticeable features on this figure include the presence of plateaus at the high energy edge of the C signal (region II in the inset), increase

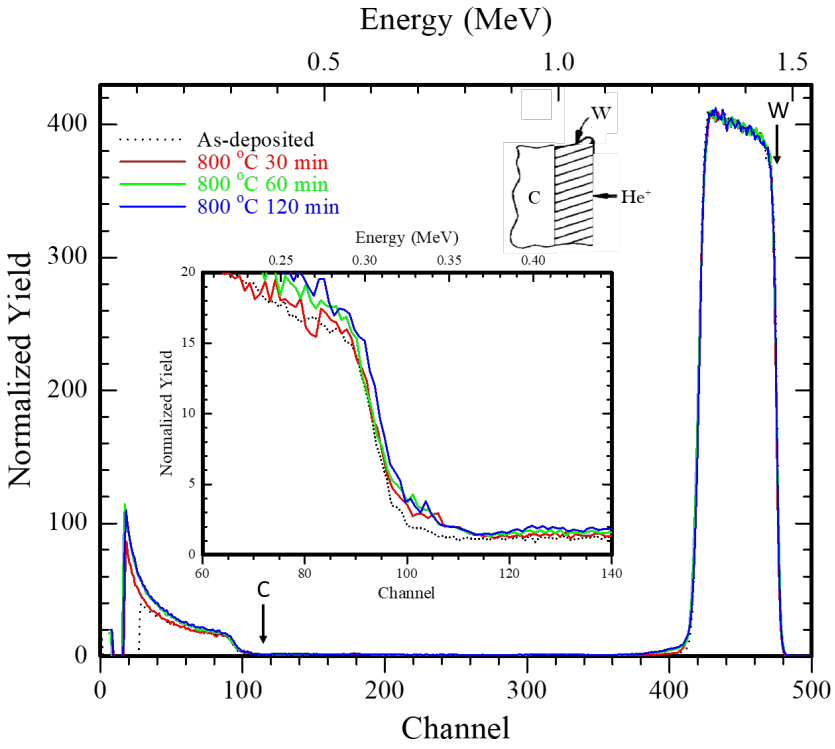

Figure 7.3: The superposition of RBS spectra of as-deposited and samples annealed at 800 °C, for different annealing duration as indicated on the figure

in reaction zone width with annealing duration and increase in carbon content in reaction zone with annealing duration. The appearance of these plateaus is an indication of carbide phase formation. In addition, the W signal experience a reduction in the peak height while there was corresponding increase in the plateau height. The regions indicated by II (C) and II (W) represent the reacted glassy carbon and the tungsten atoms in the carbide phase, respectively. On the other hand, the regions marked as I and III, correspond to unreacted glassy carbon and tungsten atoms, respectively. The simulated spectra of these samples showed an increase in the interaction between W and C atoms. This suggested carbide phase formation, however, it was difficult to predict the

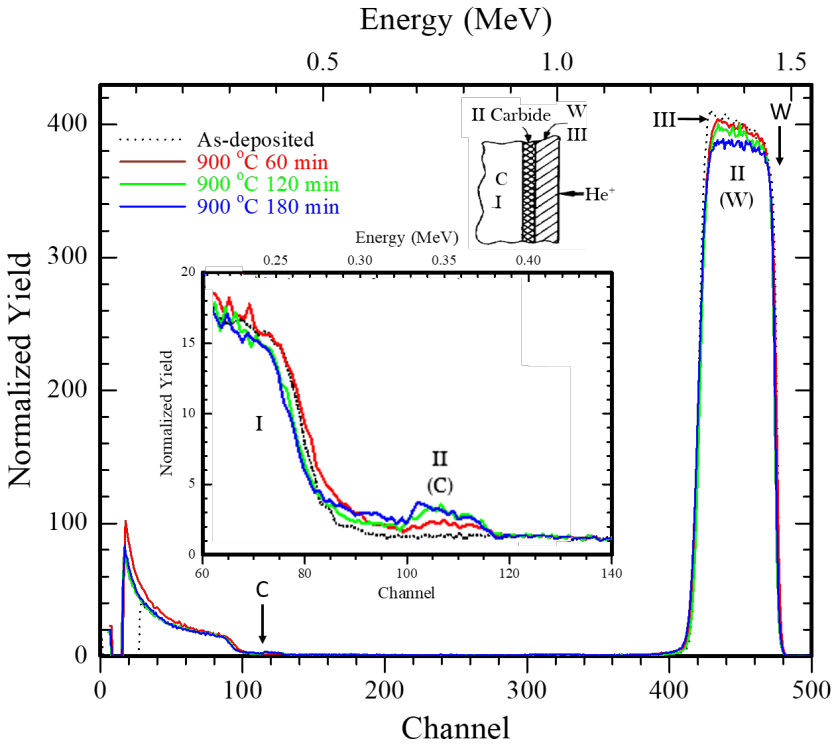

Figure 7.4: The superposition of RBS spectra of as-deposited and samples annealed at 900 °C, for different annealing duration as indicated on the figure. The decrease in the W signal (II-W) and increase in the plateaus on the C signal (II-C) of the annealed samples correspond to the formation of the carbide phase. Shown in the inset is the reacted C (II-C) in the carbide phase

.

type of carbide phase based on the stoichiometry of W and C atoms obtained. Positive identification of phase is possible only with XRD. The thickness of the intermixed layers obtained at this annealed temperature are presented in Table 7.1.

Shown in Figure 7.5, are the spectra of the samples annealed at 1000 °C. After annealing at 1000 °C for 30 min, a plateau developed on the high C edge [region II (C). The C signal of the carbide phase in this region extends to an energy corresponding to the presence of C at the sample surface. It can be

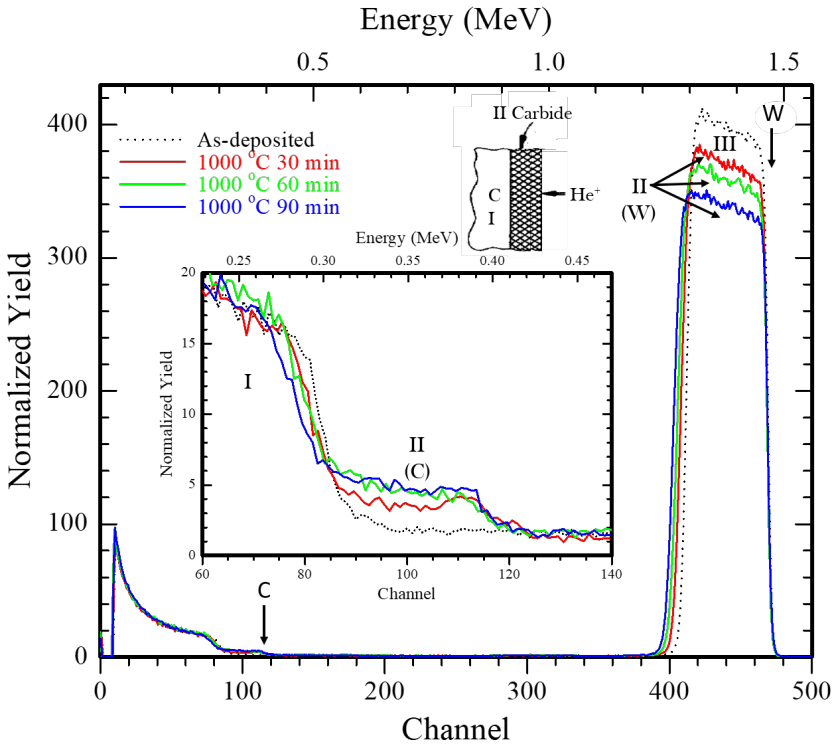

Figure 7.5: The superposition of RBS spectra of as-deposited and samples annealed at 1000 °C, for different annealing duration as indicated on the figure. The decrease in the W signal (II-W) and increase in the plateaus on the C signal (II-C) of the annealed samples correspond to the formation of the carbide phase. Shown in the inset is the reacted C (II-C) in the carbide phase

observed in Figure 7.5 that the plateaus in region II (C) increased in height with increase in the annealing temperature duration. The sample annealed at 1000 °C for 90 min has the highest plateau. As these plateaus grow in response to the high temperature annealing duration, the W signals increased in width and reduced in height [region II (W)]. The W signals widen in width because C atoms which diffused from the glassy carbon substrate into W layer made those layers thicker. The C atoms in the W layer also lowered the concentration of the W in these layers, which resulted in the decrease of the

W signal. As will be discussed below and will also be seen from the XRD results, the diffused C atoms also reacted with tungsten atoms to form carbide phase. The absence of a shoulder at the W back edges, suggested that C is the dominant diffusing species in this W/glassy carbon system. The plateaus in the intermixed region (II(C)) are flat shaped. This indicates the presence of constant composition of the carbide phase formed at these high temperatures.

The simulation results for the sample annealed at 1000 °C for 30 min showed that the elemental composition was 65 at.% W - 35 at.% C. The ratio of W to C composition is approximately 2 which indicated the presence of di-tungsten carbide (W_2C). Furthermore, the simulation results at 1000 °C for 60 min and 90 min are essentially the same in terms of the elemental composition. The samples annealed at 1000 °C for 60 min and 90 min have composition of 50 at.% W - 50 at.% C. The atomic composition for samples annealed at 1000 °C for 60 min and 90 min showed that the tungsten monocarbide (WC) phase was formed at these extended annealing durations. The resulting intermixed layer thicknesses for samples annealed at 800, 900 and 1000 °C are tabulated in Table 7.1. The intermixed layer of W and C associated with the high temperature annealing increased with both annealing temperature and duration. From Figures 7.4 and 7.5, the RBS results of the annealed samples at 900 °C and above, clearly showed that the C atoms diffused into tungsten layer.

There is a large difference in the atomic radii of these materials. Atomic radius of carbon is 0.071 nm while tungsten has atomic radius of 0.137 nm

Table 7.1: Intermixed layer growth with annealing temperature and duration

Annealing temperature (°C)	**Annealing duration (min)**	**Intermixed layer thickness (10^{15} at./cm^2)**
800.0	30.0	6.3
	60.0	8.6
	120.0	13.9
900.0	60.0	189.6
	120.0	216.8
	180.0	236.8
1000.0	30.0	282.3
	60.0	512.7
	90.0	567.7

[3]. This implies that atomic size of tungsten is almost twice that of carbon. The diffusion of carbon in tungsten and its carbides proceeds via interstitial mechanism in addition to grain boundaries diffusion [4]. Elements with small atomic sizes such as carbon, nitrogen and oxygen undergo interstitial diffusion in tungsten [4].

7.3.3 Evaluation of diffusion parameters

The growth of the intermixed layer thickness (x) with annealing time (t) is often governed by the relation [5], [6]:

$$x = kt^{1/2} \tag{7.1}$$

where, k denotes the rate constant. Using the data in Table 7.1, the plots of x versus $t^{1/2}$ for the temperatures 800, 900 and 1000 °C, gave straight line graphs shown in Figures 7.6 (a-c). Also shown in the plots are error bars estimated

from uncertainties in the simulations of the intermixed layer thicknesses. The linear graphs obtained in these figures suggested that the intermixed layer growth was parabolic and the growth kinetics of the intermixed layer was diffusion controlled. The slopes of these straight line graphs were the rate constants for their respective temperature and the values obtained were tabulated in Table 7.2.

To estimate the diffusion coefficient of the glassy carbon in tungsten, the following method was adopted. It is well known that the diffusion coefficient of the impurity atom (glassy carbon) can be obtained by the application of Arrhenius equation [7].

$$k = k_o \exp\left(-Q/k_B T\right) \tag{7.2}$$

where the k_o, Q, k_B and T are the pre-exponential factor, activation energy, the Boltzmann constant and the absolute temperature, respectively. Consequently, the values of 1/T and $\ln k$ were evaluated and plotted in accordance with the temperature dependent Arrhenius equation to obtain the graph shown in Figure 7.6 (d). The activation energy and the pre-exponential factor were evaluated from Figure 7.6(d) and the estimated values are presented in Table 7.2.

The value of activation energy 2.23 eV obtained in this work is comparable to the range of activation energies (1.72 - 4.86 eV) [8], quoted for the diffusion of amorphous carbon in W_2C. The possible reasons for the range of activation

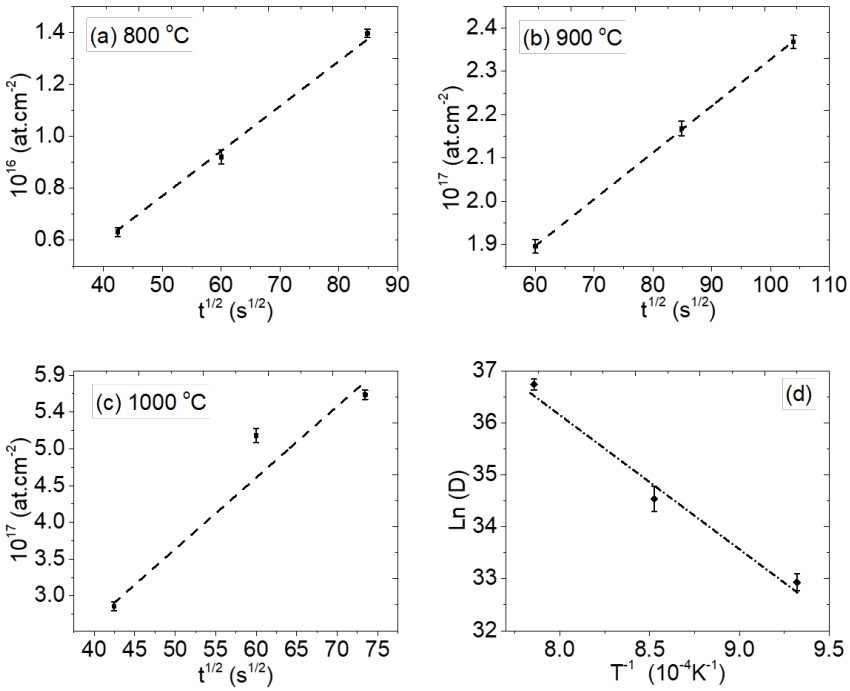

Figure 7.6: Plots of intermixed layer thickness vs. $t^{1/2}$ for temperature at (a) 800 (b) 900 and (c) 1000 °C. (d) Arrhenius plot for glassy carbon diffusion in tungsten.

energies reported by Kharatyan *et al.* [8] could be due to differences in microstructure and defect volume of the diffusion couples used. Those materials might have been sourced from different manufacturers. In addition to these, difference in the range of temperature adopted for diffusion study could also be a factor. A high activation energy has been attributed to difficulty in diffusion of carbon through the carbide phases [9], [10]. The activation energy for glassy carbon diffusion in W obtained in this study suggested the presence of carbide phase. But only the XRD technique can give a positive identification of the carbide phase formed.

Hence, the general diffusion expression governing the diffusion of glassy

Table 7.2: Temperature dependent diffusion parameters of the tungsten-glassy carbon couples

Temp (°C)	1/T ($10^{-4}K^{-1}$)	k (at./cm^2)·s$^{-1/2}$	ln k	k_o $(at./cm^2)\cdot s^{-1/2}$	Q (eV)
800.0	9.32	2.00×10^{14}	32.93	4.92×10^{24}	2.23
900.0	8.53	1.00×10^{15}	34.54		
1000.0	7.86	9.00×10^{15}	36.74		

carbon in tungsten is given by the expression:

$$k = 4.92 \times 10^{24}(at./cm^2)\cdot s^{-1/2} \exp\left(-\frac{2.23\ eV}{k_B T}\right) \tag{7.3}$$

where T is absolute temperature and k_B is Boltzmann constant.

7.3.4 Analysis of uncertainty in the RBS measurements

The goal of this subsection is to perform a quantitative analysis of the main sources of uncertainties associated with the RBS measurements. According to the Guide to the Expression of Uncertainty in Measurement [11], there are two types of uncertainty estimation: Type A and Type B. Uncertainties are type A when they can be calculated as a standard error from a set of measurements. They are type B when the statistical data needed for type A is not available, and the user has to make a more informal estimate of the probable measurement error. The common sources of uncertainty in the RBS measurement and analysis [12], [13] are listed in Table 7.3. The expanded uncertainty (U_E) covers a suitable confidence interval. It is obtained from the product of the combined standard uncertainty u_c and a coverage factor k.

$U_E = ku_c$. The combined uncertainty is obtained from the expression [11]:

$$u_c = (u_1^2 + u_2^2 + , ... + u_n^2)^{1/2} \tag{7.4}$$

To obtain the uncertainty in the counting statistics from the RBS data, the counts were plotted as a function of the detected energy. The energy loss of the He ion as it traversed in and out of the tungsten layer ΔE, is obtained from the FWHM of the tungsten signal. With the knowledge of the incident energy E_o=1.6 MeV for the He ions, the standard deviation of energy straggling Ω_{exp} is given by [14]:

$$\Omega_{exp} = \sqrt{(\frac{E_o}{\Delta E})} \times 10^{-2} \tag{7.5}$$

For a typical RBS result, with He ions undergoing an energy loss of 105.1 keV, the relative standard deviation of energy straggling was estimated as 3.91%.

Table 7.3: Budget of uncertainties in RBS analysis

S/N	Sources of Uncertainty	Type A or B	Standard uncertainty (%)
1	Counting statistics	A	3.90
2	Spectrum fitting	A	4.02
3	Energy calibration	A	1.98
4	Scattering angle	B	0.61
5	Electronic gain	B	0.50
6	Beam energy	B	0.30
7	Rutherford cross-section	B	0.16
8	RUMP uncertainty	B	0.80
9	He stopping cross-section	B	0.60
10	Beam current	B	0.40
	Combined uncertainty u_c	=	6.10

The uncertainty in the energy calibration is obtained from the evaluation

of energy per channel (See section 7.2). The estimated energy per channel was 3.03 keV/ch. Using the procedures outlined by Kirkup and Frenkel [15], the standard uncertainties in 3.03 keV/ch. was estimated as 0.06 keV/ch. This leads to a relative uncertainty of 1.98% in the energy calibration. Other uncertainties were obtained from [12], [13], [16]. An approximately Gaussian distribution is assumed. Given a coverage factor of 1.96, results in a level of confidence of approximately 95% with expanded uncertainty of 11.96%.

7.3.5 XRD results and discussion

To complement the RBS results, all the samples were characterised by grazing incidence X-ray diffraction (GIXRD). This was meant to identify the phase composition of the diffusion couples and monitor any new phase formation as a result of the heat treatment. The diffractograms for the as-deposited and annealed samples are shown in Figure 7.7. The phases were identified by comparing the peak position in the X-ray diffractograms with the peak position of the tungsten carbide standard tabulated in the ICDD-PDF-2 [17]. The comparison was supported by other papers [1], [4], [18]. The diffractogram of the as-deposited sample showed the presence of a strong diffraction peak at 2θ position of 39.73° and low intensity peaks at 74.86° and 87.23°, these peaks correspond to the (110), (211) and (220) orientations of W, respectively [17]. Also present was a strong broad peak at 25.18° and two other small broad peaks at 43.10° and 79.07°. These peaks correspond to the (002), (100) and (110) reflections of the graphitic domains in the glassy carbon [19]–[21]. The broad

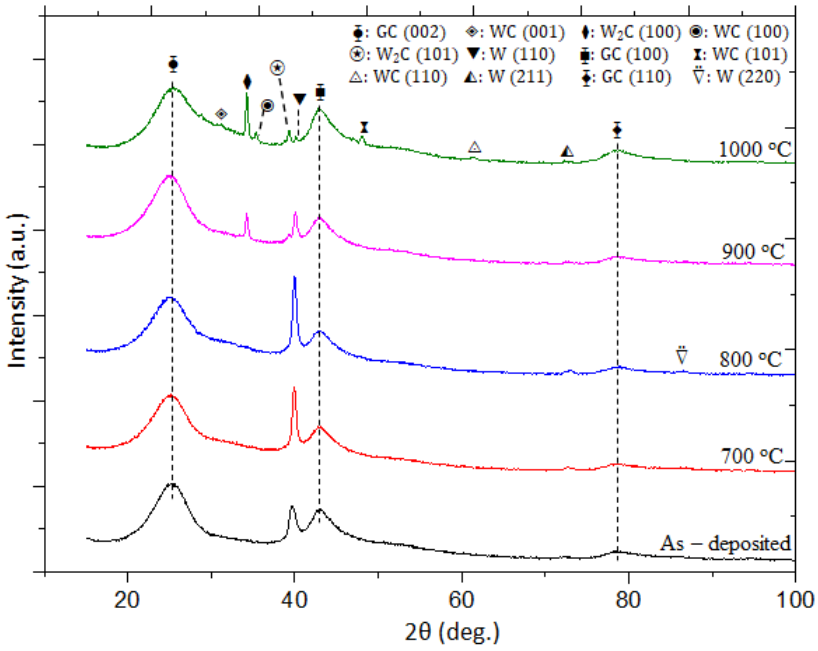

Figure 7.7: XRD diffractograms of as-deposited and the annealed tungsten film-glassy carbon samples. The glassy carbon (GC) peaks positions are 25.18, 43.10 and 79.07°; as-deposited tungsten (W) film peak positions are 39.73, 74.86 and 87.23°; W_2C peak positions are 34.19° and 39.29°; WC peak positions are 31.19, 35.32, 48.01 and 61.39°. All samples were vacuum annealed for 1 h at the anneal temperatures shown in the figure. All crystal planes are marked on the figure.

nature of these peaks is characteristic of disordered material due to scattered beams. This showed that glassy carbon, indeed, contains a certain amount of disordered material, often referred to in literature as nanocrystalline or paracrystalline material [22].

The absence of a carbide peak in the as-deposited sample showed that the XRD results were in good agreement with the RBS/RUMP simulated results, which showed no sign of atomic mixing or interaction at the interface. Similar

diffraction peaks were observed in the sample annealed at 700 °C, with the three additional features in the W (110) peak. This peak increased in intensity with reduced width, and a slight shift in the peak position to 2θ = 39.93°. The increase in the intensity of W peak upon annealing showed that the as-deposited W film was characterized by small grain size. The W film structure improved in its crystallinity upon annealing, hence the reduced width. The slight shift by 0.20° toward the higher 2θ angle can be attributed to residual stress relief due to annealing [23]. All the annealed samples experienced slight shifts in 2θ positions of the W (110) peak, with the sample annealed at 900 °C having the maximum shift of 0.33° from its initial peak position in the as-deposited sample (Table 7.4).

The sample annealed at 800 °C had the maximum intensity for W peak (110). This was due to the fact that at 800 °C, the W film had improved in its crystallinity and there was no carbide formed. The absence of a carbide phase in the diffraction pattern of this sample showed that the W/C couples was thermally stable at 800 °C. This was fairly in good agreement with the RBS results shown in Figure 7.3. At 800 °C, the annealed temperature was not high enough to cause phase formation.

The diffraction pattern for the sample annealed at 900 °C (Figure 7.7) showed the presence of two additional peaks at 34.19° and 39.29°. These peaks were indexed as ditungsten carbide (W_2C) with orientation (100) and (101) planes, respectively. A similar observation was made by Wand and Jacob

[1] who reported that the first phase which formed in tungsten-amorphous carbon multilayer films was W_2C at an annealing temperature of 877 °C. Another feature associated with the diffraction pattern of the sample annealed at 900 °C was the drastic reduction in W (110) peak intensity. This is obviously reasonable since W was consumed to form W_2C.

At the annealing temperature of 1000 °C, the diffraction pattern indicated that the intensity of W_2C peak increased, while four new phases appeared at 2θ position of 31.19, 35.32, 48.01 and 61.39°. These peaks were indexed to tungsten monocarbide (WC) with (001), (100), (101) and (110) [17] crystal orientations, respectively. The formation of this additional carbide phase caused an almost complete depletion of the pure W peak. The W film had reacted completely with glassy carbon to form carbides. Since more WC peaks appeared at 1000 °C compared to the two peaks of W_2C which existed from 900 °C, it showed that further formation of W_2C was not favourable at this higher temperature. Luthin *et al.* [24] in their study on carbon film deposited on tungsten observed that W_2C was the first carbide phase to form and this phase later transformed to WC at a temperature of 1270 K. The formation of W-rich phase (W_2C) at a temperature of 900 °C could be attributed to the fact that, at this temperature, there was a low concentration of glassy carbon in W after intermixing, hence favouring the formation of W_2C. At the higher temperature (1000 °C), there was more diffusion of glassy carbon into W. Consequently, there was large enough carbon concentration available for the formation of WC.

To quantify the crystalline nature of the W film deposited, the diffractograms for all the samples were fitted with pseudo-Voigt function using the OriginLab program. This function is a convolution of both Lorentzian and Gaussian functions. Figure 7.8 shows the fitted diffraction patterns for the as-deposited and annealed samples. From the fitted diffractograms, the full width at half maximum (FWHM) and peak positions of W were determined. The values obtained are tabulated in Table 7.4. The crystallite size (l_a) of the as-deposited W film and annealed samples were estimated with the aid of the Scherrer equation [25]:

$$l_a = \frac{k\lambda}{\beta cos\theta} \tag{7.6}$$

where $\beta = \sqrt{B^2 - b^2}$, with B being the FWHM of diffraction peak in radians and b is the instrumental broadening [25], λ = 1.5406 Å is the wavelength of Cu X-ray source used for XRD measurement, k is the Scherrer constant, taken as 0.94 and θ is obtained from the peak positions. The instrumental broadening b is expressed by the relation [26], [27]:

$$b = \tan^{-1}\left(\frac{W_R}{R_G}\right) + 2\left(\frac{\Delta\lambda}{\lambda}\right)\tan\theta \tag{7.7}$$

where W_R is the receiving slit width (0.2 mm), R_G is the radius of goniometer (190 mm) and $\Delta\lambda$ is resolution of the diffractometer 2×10^{-3}. Using Equations 7.6 and 7.7, the crystallite size l_a which is the average length of the graphitic lamellae within the glassy carbon [28], was estimated from the diffraction pattern of the as-deposited sample. The value of l_a was estimated as 2.57 nm,

using the crystal orientation (100) [29] for the glassy carbon. This value is comparable with l_a = 3.10 nm obtained by Njoroge, *et al.* [30], who worked on the same grade of glassy carbon, the Sigradur© G, using Raman spectroscopy analysis.

The value for the average crystallite size obtained in this study supports the assertion that glassy carbon is a nanocrystalline material. The estimated average crystallite size for as-deposited W film is 9.77 nm, using the (110) preferred crystal orientation. This showed that the W film deposited at room temperature was substantially composed of small grains. This finding is similar to results obtained by Hugon, *et al.* [31], where the deposited W film had grain sizes varying from 13-50 nm depending on the W film thickness. In this study, the estimated crystallite size for the annealed samples increased steadily with annealing temperature (Table 7.4) up to 18.05 nm for the sample annealed at 900 °C.

Table 7.4: Data extracted from the fitted diffraction patterns and the calculated crystallite size

Temperature (°C)	**Phase Identity**	**Peak Position** 2θ**(deg.)**	**FWHM (deg.)**	**Crystallite size** l_a**(nm)**
25.0	W(110)	39.7	0.91	9.8
700.0	W(110)	39.9	0.56	15.7
900.0	W(110)	40.0	0.55	16.1
1000.0	W(110)	40.1	0.49	18.1

The diffraction patterns show that there is no significant structural change to the glassy carbon at these annealing temperatures for the duration of 1 h. This is also supported by the fitting results, which showed no sign of change in

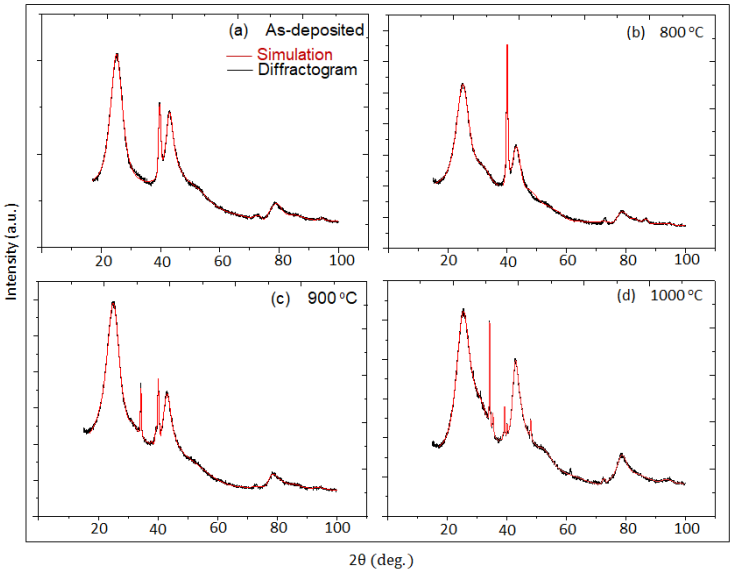

Figure 7.8: Fitted XRD diffraction pattern of (a) as-deposited and the annealed samples at (b) 800 °C (c) 900 °C and (d) 1000 °C. All samples annealed for 1 h duration

peak positions of the three prominent peaks indexed to graphitic domains in the glassy carbon. This suggests that glassy carbon is thermally stable at these annealing temperatures and duration. The two non-destructive analytical techniques used in this study complemented each other well. XRD appears to be more sensitive to carbide phase formation than RBS. Although, both techniques showed the presence of the first carbide formed in the sample annealed at 900 °C, only the XRD technique positively identified this carbide phase. It was difficult to achieve that with RBS/RUMP technique. Good prediction for carbide phase with RBS occurred in the samples annealed at 1000 °C.

7.3.6 Heat of reaction and carbide phase formation

Annealing treatment of thin W films in contact with glassy carbon substrates leads to atomic mixing and subsequently solid-state reactions. The phases formed depends on kinetic and thermodynamic factors at the growth interface. Using enthalpies of formation data, the heat of reaction can be evaluated for reaction between one element and another, elements and compound phase. It is equivalent to heat of formation when there is strong interaction between two elements to form a compound phase, since the standard enthalpy of formation of an element is zero by definition [32]. A procedure for calculating heat of reaction was described in details by Pretorius, *et al.* [32]. In Table 5.2, the enthalpies of formation of the tungsten carbides, WC and W_2C at 298 K are $\Delta H_f^o(WC) = -40.40$ kJ/mol. and $\Delta H_f^o(W_2C) = -13.41$ kJ/mol., respectively. The heats of reaction (ΔH_R) for the interaction between tungsten (W) and glassy carbon (C) and WC to form W_2C, were calculated. The possible reactions between W and C, W and WC to form W_2C are described by reactions 7.8 and 7.9:

$$2W + C \rightarrow W_2C \tag{7.8}$$

Substituting the enthalpies of formation in the reaction 7.8, the change in heat of reaction is calculated thus;

$$\begin{aligned} 2(0) \qquad & 1(0) && 1(-13.41 \quad kJ/mol.) \\ \Delta H_R \qquad & = -13.41 - 0 && = -13.41 \quad kJ/mol. \\ \Delta H_R \qquad & = -13.41/3 && = -4.47 \quad kJ/mol.at. \end{aligned}$$

Similarly for reaction 7.9

$$W + WC \rightarrow W_2C \tag{7.9}$$

the change in heat of reaction is calculated as follows;

$$\begin{aligned} 1(0) \qquad & 1(-40.4 \quad kJ/mol.) && 1(-13.41 \quad kJ/mol.) \\ \Delta H_R \qquad & = -13.41 + 40.40 && = +26.99 \quad kJ/mol. \\ \Delta H_R \qquad & = +26.99/3 && = +9.0 \quad kJ/mol.at. \end{aligned}$$

The heats of reaction (ΔH_R) for the interaction between glassy carbon (C) and tungsten (W) and W_2C to form WC, the possible reactions are as follows:

$$W + C \rightarrow WC \tag{7.10}$$

$$the change in heat of reaction is; \Delta H_R \quad = -40.4 - 0 \quad = -40.4 \quad kJ/mol.$$

$$\Delta H_R \quad = -40.4/2 \quad = -20.2 \quad kJ/mol.at.$$

In similar way, for the reaction

$$W_2C + C \rightarrow 2WC \tag{7.11}$$

this gives the change in heat of reaction as follows;

$$\Delta H_R \quad = -80.8 + 13.41 \quad = -67.39 \quad kJ/mol.$$

$$\Delta H_R \quad = -67.39/4 \quad = -16.85 \quad kJ/mol.at.$$

The values of ΔH_R obtained in reactions 7.8, 7.10 and 7.11 are thermodynamically favourable since these values are negative. In the case of reaction 7.9, the positive value of ΔH_R showed that the reaction is improbable. At all temperatures in Table 5.2, this trend observed for the values of ΔH_R is the same for all values of enthalpies of W_2C and WC, respectively.

At this juncture, to determine which of the carbide phases should formed first, the effective heat of formation model (EHF) discussed in section 5.6.2 is applied, to check if it correctly predicts the sequence of carbides formed from the interaction between glassy carbon and the W films. Using these values of ΔH_R obtained for reactions between the elemental C and W in reaction 7.8 and 7.10, the plot of $\Delta H^{'}$ as a function of effective concentration for the carbides in a binary W-C phase diagram resulted in triangularly shaped diagrams

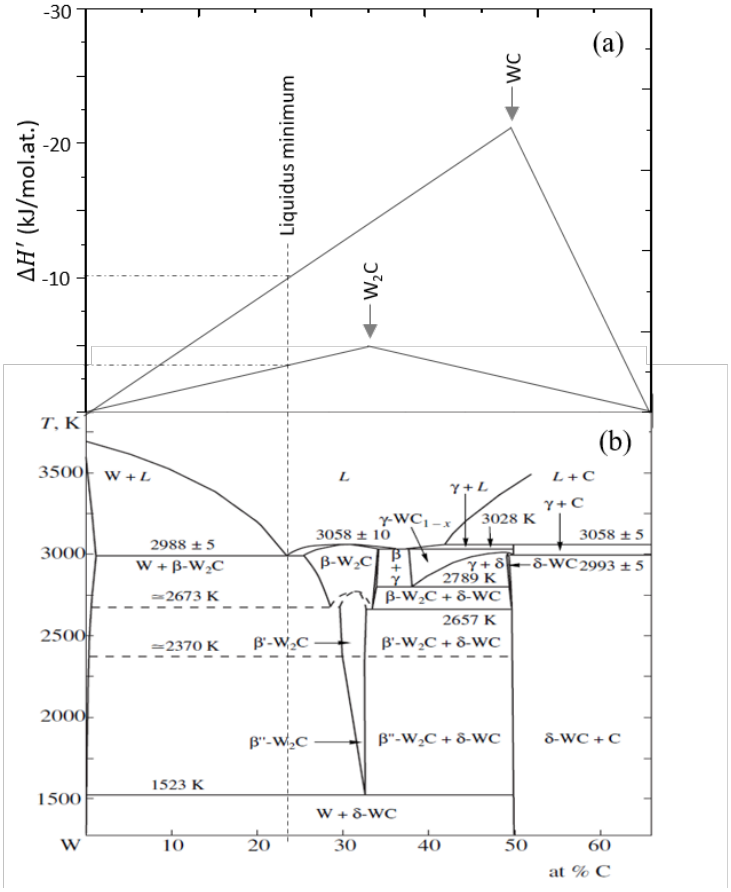

Figure 7.9: The EHF diagram for the W-C binary system, showing that at the concentration of the liquidus minimum the phase WC has the most negative effective heat of formation and its formation therefore would lead to the largest change free energy

(Figure 7.9). Each triangle in Figure 7.9 (a) represents the energy released as a function of concentration [32] during the formation of a particular phase of tungsten carbide. This W-C system has a lowest eutectic point of 2988±5 K at a composition of about 23.5 at.% C. Using the liquidus minimum, W_2C has effective heat of formation of -3.75 kJ/mol.at. while WC has the effective heat of formation of -10 kJ/mol.at. Therefore, the EHF model predicts WC as the

first phase to form since it has the most negative effective heat of formation, at the liquidus minimum. This shows from both the heat of reaction calculated and the EHF model that, WC should be the first carbide phase to form, since it has the most negative values in both cases. The tungsten carbide formation sequence observed in this study is similar to the results reported by Wang and Jacob [1], where the phase formation involving tungsten-amorphous carbon multilayer films showed that the first phase formed was W_2C at annealing temperature of 877 °C. It was confirmed from the RBS and XRD techniques that W_2C formed first. Similar to observation by Canali, *et al.* [33], the compound phase formation in this study, is driven towards the phases that are richer with the remaining element. Since it is suggested that C diffuses by interstitial mechanism into the W films, it implies that at the initial stage of the phase formation, more W atoms were available for W_2C formation. And at higher temperatures (1000 °C), at which point the W films were completely consumed (Figures 7.5 and 7.7), sufficient C had diffused into the W films such that formation of WC dominates. Reaction 7.11 supports this assumption that sufficient supply of C promotes the conversion of W_2C to WC.

The first phase observed is sometimes dependent on the measurement technique used, as phase formation can be more sensitive to impurities at the beginning stages of growth. The presence of impurities at the interface can affect the effective concentrations, thereby affecting which phase might start to form [34]. Surface energies might also play a dominant role during the early stages of phase formation. In addition, the glassy carbon has a

microstructure which differs from the form of carbon used to determine the W-C phase diagram (Figure 5.2). Hence, the difference in reaction chemistry of these carbons can also be a factor affecting phase formation sequence.

7.3.7 SEM results and discussion

The surface morphology of as-deposited and the annealed samples was investigated by scanning electron microscopy (SEM) analysis. Figure 7.10 presents the SEM micro-graphs of the as-deposited W films and annealed samples. It can be observed from Figure 7.10 (a) that the surface of as-deposited W films was smooth without any distinct feature. This indicates that the W films deposited were fairly uniform and fully covered the surface of the glassy carbon substrates.

In Figure 7.10 (b), the surface morphologies of samples annealed at 600 and 700 °C (not included here) are similar to that of as-deposited sample which is characterized by fairly smooth surface. Although the crystallinity of the W films annealed at 700 °C was observed to increase from XRD analysis, no visible changes were observed in the surface morphology as a result of heat treatment at these temperatures. Shown in Figure 7.10 (c) is the SEM image of the sample annealed at 800 °C. Here, the W films were no longer smooth but had small granular features on the surface after heat treatment at this temperature. This is due to the increase in the crystallite size as annealing temperature and duration increased. This finding correlates with the XRD results in Section 7.3.5 (Table 7.4), where it was shown that the crystallite sizes

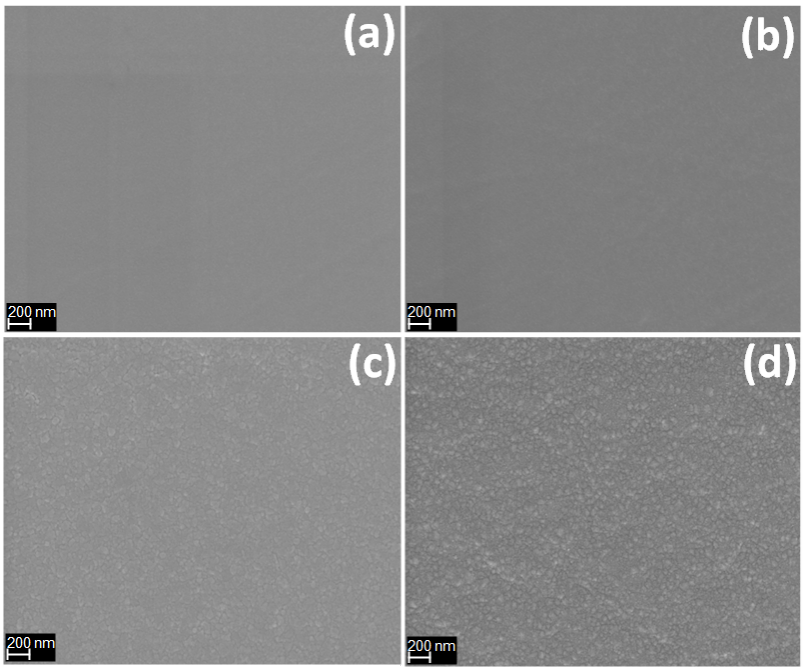

Figure 7.10: SEM micro-graphs of W-GC samples (a) as-deposited, (b) annealed at 600 °C, (c) 800 °C and (d) 1000 °C

of the W films increase with the annealing temperatures.

Furthermore, the sample annealed at 900 °C (not shown here) had nearly similar surface morphology with the one annealed at 800 °C. Figure 7.10 (d) indicates that the surface morphology of the W-GC sample changed substantially after annealing at 1000 °C. It can be seen that the surface roughness increased at this temperature compared to the preceding temperatures. This suggests the presence of larger crystallite sizes which could be attributed to the presence of poly-crystalline W carbides at this temperature. It can be noticed that the highest crystallinity/grain size of W film was observed at this temperature as shown in Table 7.4.

Generally, the SEM images of the annealed sample showed complete absence of delamination even at 1000 °C. This showed that the W films were firmly adhered to the glassy carbon substrate, indicating that appropriate sputtering parameters were used.

7.4 Analysis of structural changes in glassy carbon under heat treatment by Raman spectroscopy

Following the results obtained in the preceding section where the glassy carbon appeared to be thermally stable, even at annealing temperature up to 1000 °C for 1 h (Figure 7.7), it became pertinent to anneal the glassy carbon without the W films and at much longer duration of 3 h at the same temperature range to properly understand its structural changes under heat treatment. Decay heat of stored nuclear waste might have thermal degradation effect on the casks materials. Hence, the need to study the structural change in glassy carbon due to heat. The samples in the preceding section were not Raman active due to W films on the surface of the glassy carbon.

The Raman spectra of the as-received and this batch of annealed glassy carbon were collected with a Jobin Yvon Horiba TX64000 triple grating Raman spectrometer. An excitation laser source with a 514.5 nm (green) laser was used in this study. In order to avoid sample heating, the laser power was maintained at 1 mW on the sample surface during analysis.

Figure 7.11 presents the Raman spectrum of pristine glassy carbon. The

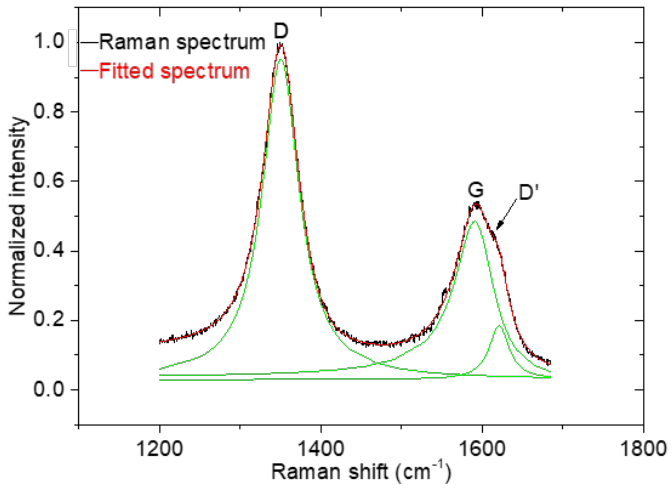

Figure 7.11: Raman spectrum of pristine glassy carbon (black line) fitted (red line) with combination of two Lorentzian function and a Breit-Wigner-Fano (BWF) function

peak at 1350 cm^{-1} is the breathing mode of A_{1g} symmetry called the disordered (D) peak [35], [36]. Its intensity is strictly connected to the presence of sixfold aromatic rings [36] and it occurs in graphitic materials with small crystallite sizes. The peak at 1590 cm^{-1} (G peak) is associated with E_{2g} symmetry and originates from lattice vibrations in the plane of the graphite-like ribbons [35], [37]. In addition to G peak, there is a presence of almost an invisible small peak (D' peak) at 1621 cm^{-1} which appears as a shoulder on the G peak. It is attributed to small sp^2 crystallite content in glassy carbon [35], [38]. A good fit on this spectrum was achieved by using two Lorentzian and a Breit-Wigner-Fano (BWF) functions. The D peak was fitted with one Lorentzian function while a Lorentzian + BWF functions were sufficient to fit the G and D' peaks.

To fully understand the structural changes of the glassy carbon due to heat-treatment, the Raman spectra of as-received highly oriented pyrolytic graphite (HOPG) and compressed polycrystalline graphite were also obtained. Figure 7.12 presents the overlaid spectra of the as-received HOPG, polycrystalline graphite and the glassy carbon. The Raman spectra of the HOPG and the polycrystalline graphite served as reference for interpretation of structural changes in glassy carbon due to annealing. The Raman result of the HOPG

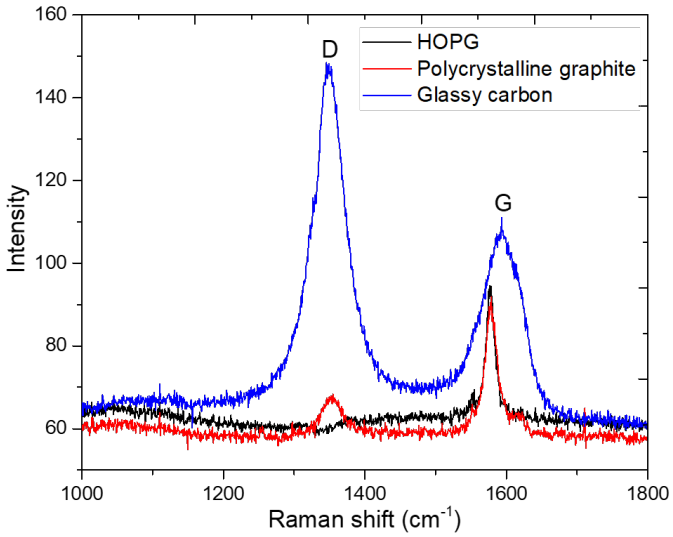

Figure 7.12: The Raman spectra of as-received HOPG, polycrystalline graphite and glassy carbon

showed that only one peak centered at 1577 cm^{-1} was observed in the spectrum. This peak is called the graphitic peak or (the *G* peak), as observed in pristine glassy carbon. In the as-received polycrystalline graphite, the *G* peak also appeared at 1577 cm^{-1} but this peak is accompanied by another weak

band centered at about 1350 cm^{-1}. This peak is called the disordered peak (D) peak.

Figure 7.13 presents the spectra of glassy carbon as a function of annealing temperatures. As shown in this Figure, the shape of both D and G bands changed with increasing annealing temperatures. Two noticeable features of these annealed spectra are the narrowing of both D and G peaks and reduction in the peaks intensities. In addition, there is slight shift in the G peaks towards the lower frequencies. Both the D and G peaks' FWHM reduced due to reduction in bond-angle disorder and local crystallization of the glassy carbon. These spectra were fitted in the same manner as was

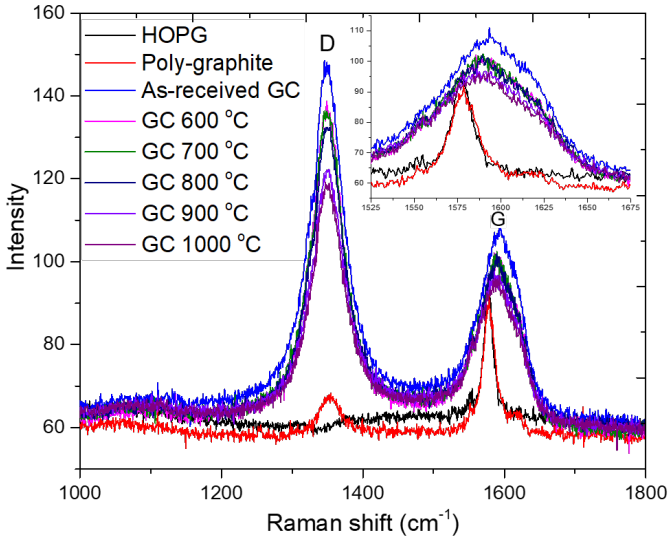

Figure 7.13: The overlay of Raman spectra of annealed glassy carbon (GC) on the as-received HOPG, polycrystalline graphite and glassy carbon. Samples were vacuum annealed for 3 h at temperatures shown in the figure. Shown in the inset is the magnified G peak region.

done with the pristine glassy carbon. The peak positions, full width at half maximum (FWHM) and integrated areas of the peaks were obtained. From the fits, the maximum frequency of the *G* peak decreased from 1590 cm^{-1} (for un-annealed sample) to around 1588.5 cm^{-1} in the sample annealed at 1000 °C. This shifts in the *G* peak position indicate the tendency of the glassy carbon to experience a decrease in its amorphous content upon heat treatment. The shift in the *G* peak to lower frequency at higher annealing temperature is similar to shifts in different carbon materials, such as coal, carbon fiber and carbon blacks reported by other researchers [39]–[41]. This shift in *G* peak position is attributed to temperature induced changes in the in-plane inter-atomic force constants in the graphitic layer [40], [41]. The *D* peaks positions of the annealed glassy carbon are relatively the same, irrespective of annealing temperature. This is expected since the *D* peaks of both the as-received polycrystalline graphite and glassy carbon were originally at the same position (1350 cm^{-1}). The tendency for graphitization of the glassy carbon structure due to heat treatment cannot make its *D* peak position shift away from that of the polycrystalline graphite.

On the other hand, both the *D* and *G* peaks experienced bandwidth narrowing and peak intensity reduction. This effect is more pronounced in the *D* peaks. Since the *D* is completely absent in HOPG, but appeared as very weak band in the polycrystalline graphite (Figure 7.13), it suggests that the reduction in *D* peak of the annealed glassy carbon is an indication of increasing order and growing size of the graphitic domains [42]. That is, an indication

of reduction in disorder. The same explanation applies as well, to the G peak reduction and the shift in its position towards the lower frequency. It all points towards reordering of the graphitic content in the glassy carbon. The G peak intensities for both HOPG and the polycrystalline graphite, are lower with narrow widths compared to that of as-received glassy carbon. The broad width of the G peak of the glassy carbon also suggests that it is composed of disordered carbon. This results in its higher frequency peak position compared to those of HOPG and the polycrystalline graphite. These results showed that the general effect of annealing on the glassy carbon is thus, reordering and growing size of its graphitic domains.

The relative intensity of the D to G peaks ratio (I_D/I_G) for disordered polycrystalline graphite was found to be inversely proportional to the crystalline size (L_a) [43]. With laser wavelength dependent constant denoted by (C_λ), this statement is mathematically expressed as [43]:

$$\frac{I_D}{I_G} = \frac{C_\lambda}{L_a} \tag{7.12}$$

It has been established that Equation 7.12 is valid for a wide range of sp^2 bonded carbon materials over the range $2.5 < L_a < 300$ nm for laser wavelengths of 488 and 514.5 nm. Using the peak intensities of the D and G peaks extracted from the fittings, the I_D/I_G for pristine glassy carbon was found to be 1.51, as tabulated in Table 7.5. Substituting the intensity ratio in Equation 7.12 and C_λ = 44 Å for the laser wavelength dependent constant, L_a was evaluated as 2.91 nm for the pristine glassy carbon.

Table 7.5: Data extracted from the fitted Raman spectra of pristine glassy carbon and the annealed samples

Sample ID Temp (°C)	I_D / I_G	FWHM (cm^{-1})		L_a (nm)
		D	G	
RT	1.51	55.6	59.8	2.91
600.0	1.49	54.6	59.0	2.95
700.0	1.42	54.2	59.1	3.10
800.0	1.39	53.7	58.8	3.17
900.0	1.30	53.5	58.5	3.38
1000.0	1.28	52.8	57.7	3.44

It can be seen in Table 7.5 that the crystallite size L_a increased with the annealing temperatures. This suggests a growth in size of the graphitic domains in the microstructure of the glassy carbon. An increase in the L_a value with annealing temperatures indicates that the tangled graphitic ribbons in glassy carbon are gradually stretching out.

7.5 Effects of highly charged ion bombardment on glassy carbon

7.5.1 Raman analysis

A material such as glassy carbon which is envisaged to form an important component in dry casks that provide shielding against radiation is expected to offer some forms of resistant against ion bombardment. Energetic ion bombardment in the nuclear waste might largely come from the neutrons as a result of an ongoing small scale radioactivity in the waste. This motivated this aspect of the study which is the study of structural changes of glassy carbon under ion bombardment.

In this study, the glassy carbon samples were taken to the Veksler and Baldin Laboratory of High Energy Physics at the Joint Institute for Nuclear Research (JINR) Dubna, Russia. The samples were irradiated with pure isotope ^{124}Xe (99,99%), produced by the electron string ion sources (ESIS) instrument. The total ion fluence and kinetic energy used are given in the Figure 7.14 caption. The Raman technique was used to investigate the structural changes in the carbon samples due to HCI irradiation.

In order to quantitatively analyze the Raman results, the Raman spectra for all the irradiated samples were fitted in the same manner described for pristine glassy carbon in section 7.4. The Raman spectra of the pristine glassy carbon and the samples irradiated with HCI are shown in Figure 7.14. The effect of irradiation can be seen in the irradiated spectra, compared with Raman spectrum of pristine glassy carbon.

The *D* and *G* peak positions of the irradiated samples remained fairly the same relative to those of pristine glassy carbon, with *D* and *G* peak positions 1350 and 1590 cm^{-1}, respectively. This suggests that the damage induced by the HCI irradiation appears to be at low level. The only exception in terms of peak position stability, is the slight shift in the *G* peak position towards the higher frequency ($\approx$1591 cm^{-1}) for the sample irradiated at highest kinetic energy of 460 keV (Figure 7.14(d)).

Both the *D* and *G* profiles broadened in response to irradiation fluence and the kinetic energy. The fittings results showed that the FWHM of the *D*

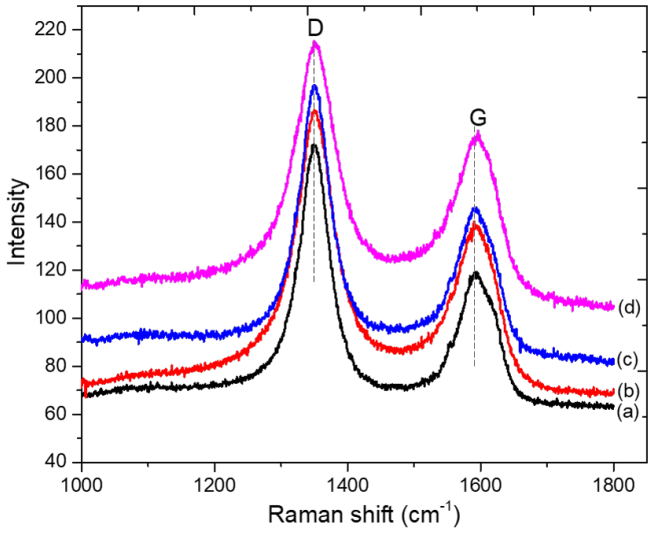

Figure 7.14: The Raman spectra of (a) pristine glassy carbon and glassy carbon samples irradiated with HCI (Xe^{40+}) with potential energy of 39 keV but with varying fluence and kinetic energy (b) fluence: 1.0×10^{11} ions/cm^2; kinetic energy 60 keV (c) fluence: 6.2 $\times10^{11}$ ions/cm^2; kinetic energy 60 keV and (d) fluence: 5.0 $\times10^{11}$ ions/cm^2; kinetic energy 460 keV

peak increase from 55.6 cm^{-1} for the pristine glassy carbon to 75.5 cm^{-1} in the sample irradiated at a fluence and kinetic energy of 5.0×10^{11} ion/cm^2 and 460 keV, respectively. The FWHM of *G* peak also showed similar trend (Table 7.6). The structural change in the irradiated samples is more pronounced in the one with higher kinetic energy of 460 keV, even though, it was exposed to intermediate fluence of 5.0×10^{11} ion/cm^2.

In Figures 7.14 (b) and (c), those samples were bombarded with the same kinetic energies of 60 keV but differed in fluence to the tune of 5.2×10^{11} ion/cm^2, yet the difference in their profile was not well pronounced. These results suggest that the structural change of glassy carbon due to effect of

HCI is largely influenced by the ion kinetic energy rather than ion fluence. This is evident in the shift to a higher frequency of G peak position in this sample marked (d) in Figure 7.14. This shift represents a disorder away from the graphitic form.

In general, the stability in both D and G peaks positions is an indication that the damage introduced in the microstructure of glassy carbon due to HCI irradiation are concentrated only at the near surface region. This damage is at minimal level compared to the results of ion implantation investigated by Njoroge, *et al.* [30] on the same grade of glassy carbon, where it was observed that the D and G peaks merged together, indicating a complete amorphization of the microstructure of glassy carbon.

Using the procedure described in section 7.4, the peak intensities of the D and G peaks extracted from the fittings were used to determine the crystallite size L_a. Equation 7.12 no longer holds for crystallite dimension less than 2 nm [36], and hence the reduced crystalline sizes were estimated from Equation 7.13 [36]:

$$\frac{I_D}{I_G} = L_a^2 C'(\lambda) \tag{7.13}$$

where $C'(\lambda) = 0.0055$ Å^{-2}. Using Equation 7.13, the crystallite size of the irradiated glassy carbon samples were evaluated. These values tabulated in Table 7.6 are smaller than the crystallite size of 2.91 nm, estimated for pristine glassy carbon. This reduction in crystallite sizes in the irradiated samples suggests an increase in disorder of microstructure of the glassy carbon upon

Table 7.6: Data extracted from the fitted Raman spectra of pristine glassy carbon and the irradiated samples

Sample ID (K.E.; fluence)	FWHM (cm^{-1})		L_a (nm)
	D	G	
as-received GC	55.6	59.8	2.91
60 keV; 1.0×10^{11} ions/cm^2	56.6	62.7	1.61
60 keV; 6.2×10^{11} ions/cm^2	67.6	71.7	1.56
460 keV; 5.0×10^{11} ions/cm^2	75.5	75.5	1.54

irradiation with HCI. But since the D and G peaks positions are relatively stable, it means the effect on the bond angles appears to be minimal.

7.5.2 AFM analysis

An atomic force microscopy study was performed on the irradiated samples so as to visualize the defects induced on the microstructure of glassy carbon by the HCI irradiation. The AFM images obtained for the pristine glassy carbon and irradiated samples are presented in Figure 7.15. It can be seen in Figure 7.15 (a) that the surface morphology of the pristine glassy carbon is fairly uniform, except for a line which passes across it. This line is probably due to accidental scratch on the surface of the sample. In Figure 7.15 (b), the surface morphology of the sample irradiated with HCI at fluence of 1.0×10^{11} Xe^{40+}/cm^2 and at kinetic energy of 60 keV appeared rough due to effect of potential energy deposition. This suggests that when the HCI impact on the surface of the glassy carbon, it captured the surface electrons and become a neutral atoms[44], this process leads to creation of rough surfaces.

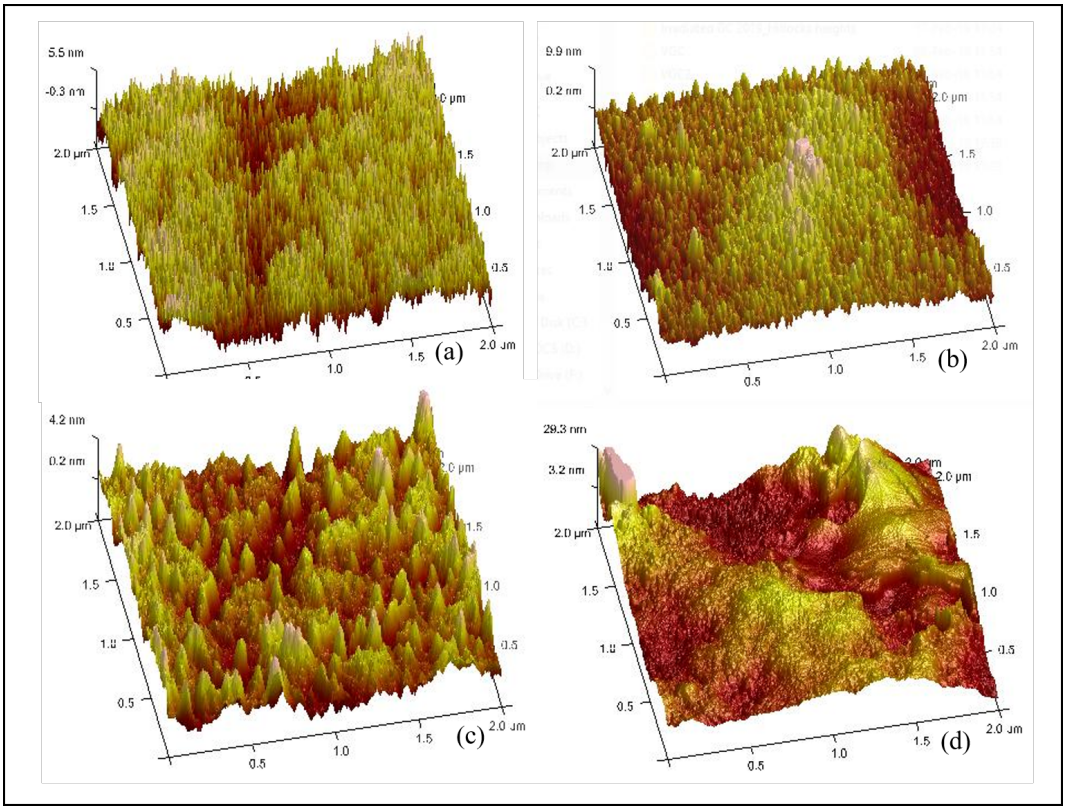

Figure 7.15: The AFM topography of (a) pristine glassy carbon and glassy carbon samples irradiated with HCI (Xe^{40+}) with potential energy of 39 keV but with varying fluence and kinetic energy (b) fluence: 1.0×10^{11} ions/cm^2; kinetic energy 60 keV (c) fluence: 6.2 $\times10^{11}$ ions/cm^2; kinetic energy 60 keV and (d) fluence: 5.0 $\times10^{11}$ ions/cm^2; kinetic energy 460 keV

It is believed that effect of this energy deposition resulted in surface sputtering of the sample, which eroded the surface. The nanostructures formed as results of HCI is observed to have increased in size with increase in fluence. This is evident in Figures 7.15 (c) and 7.15 (d) where the irradiated samples have the kinetic energy of 60 keV and 460 keV and fluence of 6.2 $\times10^{11}$ Xe^{40+}/cm^2 and 5.0 $\times10^{11}$ Xe^{40+}/cm^2, respectively. Again, it can be seen that even though, the sample marked (d) in Figure 7.15 was irradiated

with the intermediate fluence, it has the roughest surface due to high kinetic energy of 460 keV. The small different in fluence cannot account for this large difference in surface roughness. Such large surface roughness in this case has been attributed to large kinetic energy dissipation of the incident ions similar to that observed by Schneider and Briere [45].

The increase in surface roughness with fluence and kinetic energy is shown in Figure 7.16, with the hillock heights are shown in 2D images. The cross-

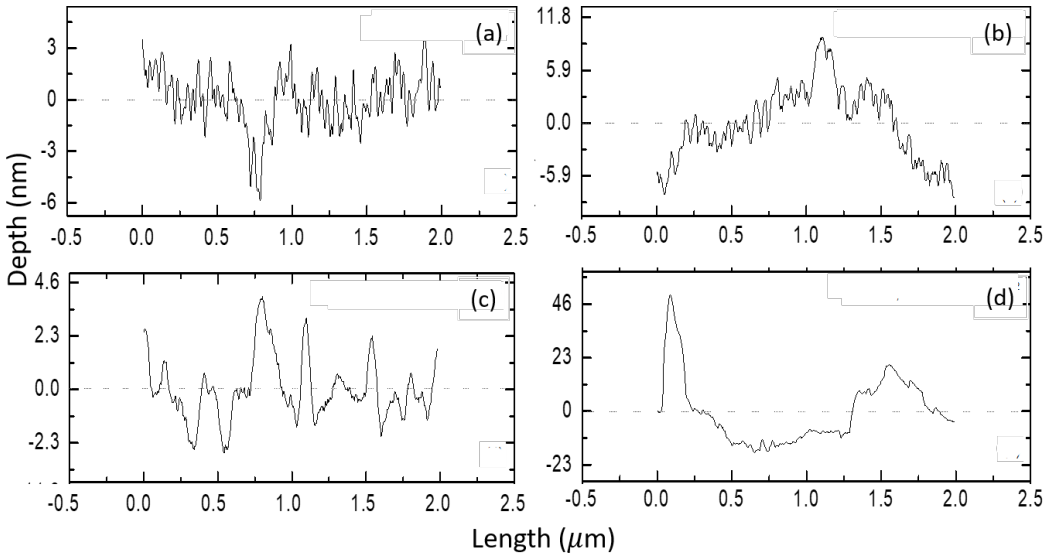

Figure 7.16: The cross-sectional of AFM topography of (a) pristine glassy carbon and glassy carbon samples irradiated with HCI (Xe^{40+}) with potential energy of 39 keV but with varying fluence and kinetic energy (b) fluence: 1.0×10^{11} ions/cm^2; kinetic energy 60 keV (c) fluence: 6.2×10^{11} ions/cm^2; kinetic energy 60 keV and (d) fluence: 5.0×10^{11} ions/cm^2; kinetic energy 460 keV

sectional view in Figure 7.16 shows that surface roughness is highest in the sample irradiated at kinetic energy of 460 keV (Figure 7.16 (d)) while it is least for the pristine glassy carbon sample. This remarkable difference in the feature associated with Figure 7.16 (d) compared to Figures 7.16 (b) and 7.16

(c) also was clearly shown in the Raman results. This shows that, there is substantial contributory effect of the high kinetic energy of the HCI to the surface roughness. Analysis of the irradiated samples with the NanoScope showed that the average surface roughness, the root-mean-square roughness (Rq) values are 1.10 nm, 2.60 nm and 7.44 nm for the samples marked (b) fluence: 1.0×10^{11} ions/cm^2; kinetic energy 60 keV (c) fluence: 6.2×10^{11} ions/cm^2; kinetic energy 60 keV and (d) fluence: 5.0×10^{11} ions/cm^2; kinetic energy 460 keV, respectively in Figure 7.16.

7.6 Amorphous fraction of glassy carbon

The structure of glassy carbon has been a subject of scientific debate among many researchers. The term paracrystalline is often used to describe glassy carbon as a material having a structure intermediate between amorphous and crystalline. The actual percentage of amorphous and crystalline contents are not well known. This knowledge is important especially as the glassy carbon is being considered as a structural component in the dry casks and nuclear technology in general.

The general form of the X-ray diffraction patterns given by nongraphitic carbons is well known. Diffuse bands have been observed in XRD results which correspond to positions of the (002), (100) and (110) reflections [21]. The degree of sharpening of these bands is frequently considered as a measure of tendency towards graphitic structure.

The diffuse bands produced by glassy carbon under XRD analysis is an indication that this material is composed of both amorphous and crystalline materials. Raman analysis of glassy carbon reveals that it contains both crystalline graphite sp^2 (G peak) and disordered carbon sp^3 (D peak). This section is devoted to studying the microstructure of glassy carbon in terms of quantifying its amorphous fraction. Figure 7.17 shows an XRD diffraction pattern for a virgin glassy carbon, the Sigradur© G grade. This diffraction

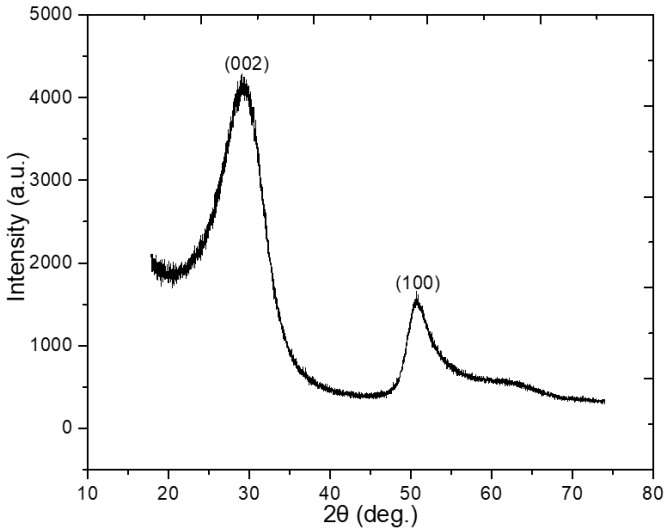

Figure 7.17: The XRD diffraction of as-received glassy carbon

pattern was acquired with XPERT-PRO diffractometer system equipped with Co (kα) X-ray source, with wavelength $\lambda = 1.789$ Å. The broad feature of the diffraction peaks show that the microstructure of glassy carbon is partly disordered [46]. The first peak in Figure 7.17 was indexed to the (002) peak of graphitic structure. The second peak corresponds to (100) crystal orientation.

In order to ensure the accuracy of this analysis, the diffraction pattern was corrected for polarization and absorption using the method described in detail by Klug and Alexander [46], before carrying out further analysis on it. Unpolarized radiation from the x-ray source undergoes partial polarization when scattered by sample [47]. For a monochromatic radiation, the ray scattered by the sample is diminished in intensity due to polarization factor P, given by [46], [47]:

$$P = 1 + \frac{\cos^2 2\theta}{2} \tag{7.14}$$

where θ is the diffraction angle. For the absorption correction A, the appropriate expression is given by [46]:

$$A = \frac{\mu x(1 - \sec 2\theta}{exp[\mu x(1 - \sec 2\theta] - 1} \tag{7.15}$$

where μ is the linear absorption coefficient and x is the thickness of the sample. The absorption exponent μx in Equation 7.15 can be expressed in terms of the density ρ (g/cm^3), through the expression [46]:

$$\mu x = \frac{m}{A}\frac{\mu}{\rho} \tag{7.16}$$

where $\frac{\mu}{\rho}$ is the mass absorption coefficient, m and A are the mass and surface area of the specimen, respectively. The glassy carbon specimen used has a mass of $\sim$77.12 mg and surface area of 100 mm^2. Substituting these values in $\frac{m}{A}$ yields 0.077 g/cm^2. For a Co (kα) radiation source, $\frac{\mu}{\rho}$ has a value of 7.07 in [46]. The diffraction data obtained in this study were corrected for both

polarization and absorption using Equations 7.14 to 7.16. Few of the data points between $2\theta = 5^\circ$ and 60° using the interval of 5 points are tabulated in Table 7.7. There are 10626 data points for each intensity curve. The data

Table 7.7: XRD diffraction intensities corrected for polarization and absorption

	Measured	Correction factors		Corrected
2θ (°)	Intensity	Absorption	Polarization	Intensity
05.0	27739.9	1.001	1.496	41547.7
10.0	5576.2	1.004	1.484	8315.1
15.0	2548.4	1.010	1.467	3773.2
20.0	1937.9	1.018	1.442	2842.9
25.0	2466.9	1.028	1.411	3578.8
30.0	3796.4	1.043	1.375	5442.8
35.0	888.2	1.061	1.336	1258.8
40.0	448.4	1.085	1.293	629.5
45.0	389.5	1.117	1.250	543.9
50.0	1361.5	1.159	1.207	1903.6
55.0	718.9	1.216	1.164	1017.8
60.0	583.6	1.297	1.125	851.2

in Table 7.7 show clearly how the acquired XRD intensity was reduced due to effects of polarization and absorption. After the experimental intensity curve had been corrected as in Table 7.7, it has to be corrected for incoherent scattering also. This is done by fitting it to the theoretical total independent scattering curve at $s = 2\sin\theta/\lambda$ values [46]. The total intensity, I_t (coherent and incoherent), scattered by an atom of material with atomic number Z is given by [46]:

$$I_t = I_e[f^2 + R(Z - \sum f_n^2)] \tag{7.17}$$

where I_e is the scattering factor for a single electron ($I_e \approx 1$), f is the atomic scattering factor and f_n is the incoherent scattering factor of the nth electron

in the atom. R is the Breit-Dirac recoil factor defined by [46]:

$$R = \left(1 + \frac{2h}{mc}\frac{\sin^2\theta}{\lambda}\right)^2 \tag{7.18}$$

where h, m and c are the Planck constant (6.626×10^{-34} m^{2}kg/s), mass of the electron (9.109×10^{-31} kg) and speed of light (3×10^{8} m/s), respectively. Upon substitution of these parameters, Equation 7.18 becomes:

$$R = \left(1 + 0.0486\frac{\sin^2\theta}{\lambda}\right)^2 \tag{7.19}$$

In Equation 7.17, the terms $I_e f^2$ and $RI_e(Z - \sum f_n^2)$ represent, respectively, the coherent and incoherent scattering by atom [46]. The numerical values of the coherent and incoherent scattering used were those tabulated in [48].

Figure 7.18 presents the plot of the normalized corrected XRD intensity I_{eu} along with the coherent scattering [I_{Coh}], the incoherent scattering [I_{Incoh}] and the total independent scattering i.e. the sum of curves I_{Coh} and I_{Incoh} against s.

The reduced intensity $i(s)$ given by Equation 7.20 [46], were then calculated from the normalized corrected intensity using the expression:

$$i(s) = \frac{I_{eu} - (I_{Coh} + I_{Incoh})}{I_{Coh}} \tag{7.20}$$

Figure 7.19 is a plot of the reduced intensity against s. Subsequent analysis is based on this reduced intensity profile.

Estimation of the amorphous fraction: In Figure 7.17, the position of (002)

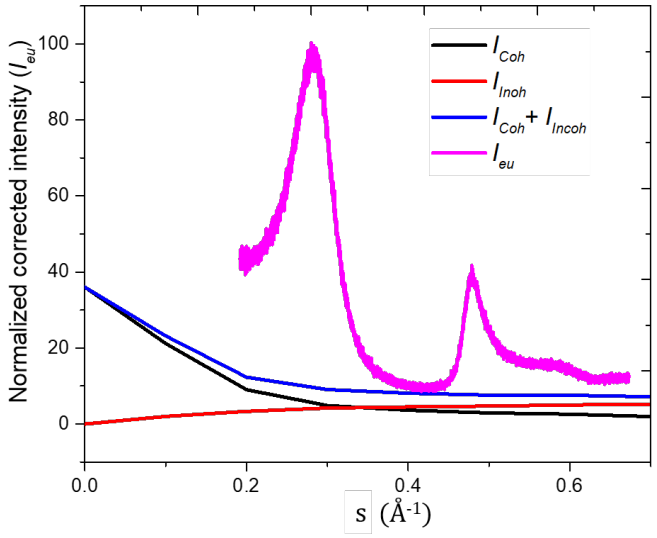

Figure 7.18: The normalized corrected intensity curve [I_{eu}] for glassy carbon plotted with the coherent scattering curve [I_{Coh}], incoherent scattering curve [I_{Incoh}] and total independent scattering curve [I_{Coh} + I_{Incoh}] against $s = 2\sin\theta/\lambda$

peak of the glassy carbon and that of the polycrystalline graphite are almost the same. However, unlike the relatively sharp graphitic peak for (002) orientation, this peak for glassy carbon is broadened. This indicates that glassy carbon is partly amorphous and partly crystalline [46]. Hence, the diffraction pattern of such a material consists of two types of reflections; the crystalline type with sharp peak and the diffuse reflections (amorphous contribution). Therefore, the reduced intensity $i(s)$ can be expressed as the sum of two separate contributions from the crystalline carbon (I_c) and the amorphous carbon (I_a). Thus, the reduced intensity $i(s)$ is given by [21], [49]:

$$i(s) = I_c + I_a \tag{7.21}$$

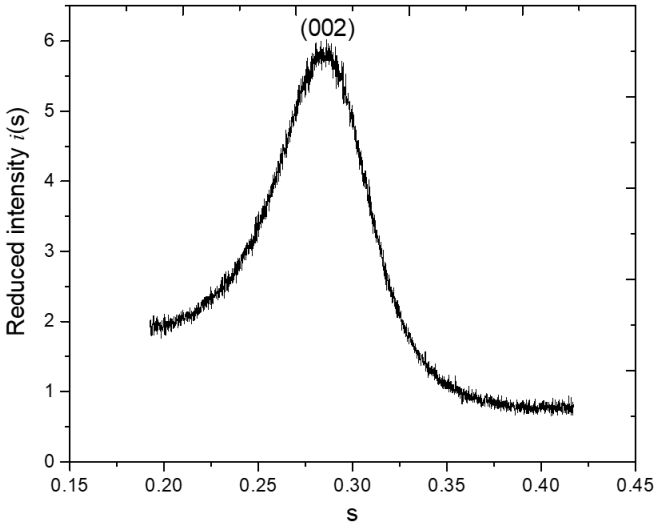

Figure 7.19: Graph of the reduced intensity curve $i(s)$ against s for the (002) peak

According to Franklin [21], the fraction of amorphous carbon present in the sample does not contribute to the peak intensity, as it is reflected only in the background of the diffraction pattern. The contribution from the amorphous carbon to the peak intensity is constant over the whole scattering range and is equal to the fraction of the amorphous carbon (x_a). Thus, the reduced intensity $i(s)$ from Equation 7.21 becomes;

$$i(s) = I_c + x_a \tag{7.22}$$

For the (002) reflection, Equation 7.22 becomes;

$$i(s) = I_{002} + x_a \tag{7.23}$$

Theoretically, Warren [50] had calculated the intensity equations for random layer lattices in terms of the layer dimension and the position of the related crystalline reflection. Franklin [21] subsequently applied Warren results in the case of carbon, and established the expression for reduced intensity $i(s)$ for the (002) reflection. Thus, the intensity of the (002) band is given by [21]:

$$I_{002} = 0.0606 s^{-2} \sum_{N} \frac{P_N \sin^2(\pi N d_N s)}{N \sin^2(\pi d_N s)} \tag{7.24}$$

where d_N is the inter-layer spacing in groups of N parallel layers, and P_N is the fraction of the total carbon contained in such groups [21]. In the intensity equation, the fraction of the carbon (i.e the amorphous carbon) which does not take part in the layer structure, does not contribute to the (002) band [21]. This follows that the fraction of crystalline carbon (the layered structure) present in the glassy carbon is equivalent to (1-x_a). Hence, from Equation 7.24, the actual reduced intensity due to the (002) reflection is given by Equation 7.25 [21], [49]:

$$I_{002} = 0.0606(1 - x_a) s^{-2} \sum_{N} \frac{P_N \sin^2(\pi N d_N s)}{N \sin^2(\pi d_N s)} \tag{7.25}$$

Substituting Equation 7.25 for I_{002} in 7.23 and rearranging, yields:

$$\frac{i(s) - x_a}{1 - x_a} \times \frac{s^2}{0.0606} = \sum_{N} \frac{P_N \sin^2(\pi N d_N s)}{N \sin^2(\pi d_N s)} \tag{7.26}$$

The right-hand side of Equation 7.26 is a periodic polynomial expression with the maximum occurring at $d_N s^i_{max} = i$ (any integer). Its first maximum occurs at $d_N s^i_{max} = 1$. This peak corresponds to the (002) band in the reduced intensity

curve [49]. Since each item in this polynomial expression, and consequently the summation, is symmetrical around the maximum s^i_{max}, the left-hand side of Equation 7.26 should have the same symmetrical profile. This fact has been harnessed to determine the fraction of amorphous carbon (x_a) in carbon materials [21], [49].

To determine the fraction of amorphous carbon in the glassy carbon, the term in the left-hand side of Equation 7.26 is calculated from the reduced intensity $i(s)$ and plotted as a function of s. Then, the term x_a was varied to obtain the best symmetrical plot of $\frac{i(s)-x_a}{1-x_a} \times \frac{s^2}{0.0606}$ versus s by fitting it with pseudo-Voigt function. The term $\frac{i(s)-x_a}{1-x_a} \times \frac{s^2}{0.0606}$ is very sensitive to the values assigned to x_a. Several values between 0 and 1 were assigned to x_a and subsequently fitted with pseudo-Voigt function in an attempt to obtain the best fit. It was found that the best fit (Figure 7.20) was obtained with the value of x_a=0.25.

The x_a value of 25% corresponds to the fraction of amorphous carbon [21], [49] in the glassy carbon. This shows that glassy carbon, the Sigradur© G grade is made up 25% amorphous carbon and 75% crystalline carbon (graphite). This result showed that glassy carbon is quite different from other carbon materials in terms of amorphous fraction. With this method of XRD intensity calculation, Franklin [21] determined the amorphous fraction in carbon black to be 35%. In the same vein, Sarkar, *et al.* [49] obtained the amorphous phase in amorphous carbon to be 58%. These results show that there are more sp^2

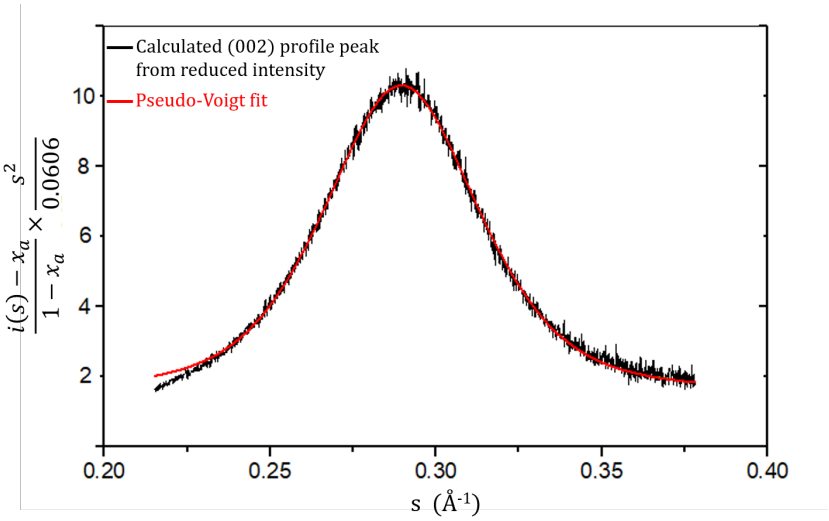

Figure 7.20: Determination of fraction of amorphous carbon (x_a=25%) in glassy carbon

bonds in the glassy carbon compared to the carbon black and amorphous carbon studied.

REFERENCES

[1] P. Wang and W. Jacob, "Deuterium diffusion and retention in a tungsten–carbon multilayer system," *Nuclear Instruments and Methods in Physics Research Section B: Beam Interactions with Materials and Atoms*, vol. 329, pp. 6–13, 2014.

[2] N. Barradas, "Double scattering in grazing angle Rutherford backscattering spectra," *Nuclear Instruments and Methods in Physics Research Section B: Beam Interactions with Materials and Atoms*, vol. 225, no. 3, pp. 318–330, 2004.

[3] W. D. Callister and D. G. Rethwisch, *Materials science and engineering: An introduction*. John wiley & sons New York, 2007, vol. 7.

[4] E. Lassner and W. D. Schubert, *Tungsten: Properties, chemistry, technology of the element, alloys, and chemical compounds*. Kluwer Academic / Plenum Publishers, New York, 1999.

[5] K. Bhanumurthy and R. Schmid-Fetzer, "Interface reactions between silicon carbide and metals (Ni, Cr, Pd, Zr)," *Composites Part A: Applied Science and Manufacturing*, vol. 32, no. 3-4, pp. 569–574, 2001.

[6] F. Goesmann and R. Schmid-Fetzer, "Metals on 6H-SiC: Contact formation from the materials science point of view," *Materials Science and Engineering: B*, vol. 46, no. 1-3, pp. 357–362, 1997.

[7] K. J. Laidler, "The development of the Arrhenius equation," *Journal of Chemical Education*, vol. 61, no. 6, p. 494, 1984.

[8] S. Kharatyan, H. Chatilyan, and L. Arakelyan, "Kinetics of tungsten carbidization under non-isothermal conditions," *Materials Research Bulletin*, vol. 43, no. 4, pp. 897–906, 2008.

[9] M. R. Andrews, "Diffusion of carbon through tungsten and tungsten carbide," *The Journal of Physical Chemistry*, vol. 29, no. 4, pp. 462–472, 1925.

[10] K. Schmid and J. Roth, "Concentration dependent diffusion of carbon in tungsten," *Journal of nuclear materials*, vol. 302, no. 2-3, pp. 96–103, 2002.

[11] International Organization for Standardization, "Guide to the expression of uncertainty in measurement," Geneva, 1995.

[12] C Jeynes, N. Barradas, and E Szilágyi, "Accurate determination of quantity of material in thin films by Rutherford backscattering spectrometry," *Analytical chemistry*, vol. 84, no. 14, pp. 6061–6069, 2012.

[13] K. Sjöland, F Munnik, and U Wätjen, "Uncertainty budget for ion beam analysis," *Nuclear Instruments and Methods in Physics Research Section B: Beam Interactions with Materials and Atoms*, vol. 161, pp. 275–280, 2000.

[14] C. Wei-Kan, J. Mayer, and M. Nicolet, *Backscattering spectrometry*. Academic Press, New York, 1978.

[15] L. Kirkup and R. B. Frenkel, *An introduction to uncertainty in measurement: Using the gum (guide to the expression of uncertainty in measurement)*. Cambridge University Press, 2006.

[16] S Ourabah, A Amokrane, and M Abdesselam, "Experimental determination of layers films thicknesses," *International Journal of Physical Sciences*, vol. 8, no. 30, pp. 1537–1545, 2013.

[17] H. F. McMurdie, M. C. Morris, E. H. Evans, B. Paretzkin, W. Wong-Ng, L. Ettlinger, and C. R. Hubbard, *Standard X-ray diffraction powder patterns from the JCPDS research associateship*. Cambridge University Press, 1986.

[18] M. B. Zellner and J. G. Chen, "Synthesis, characterization and surface reactivity of tungsten carbide (WC) PVD films," *Surface science*, vol. 569, no. 1-3, pp. 89–98, 2004.

[19] T. Shiell, C. de Tomas, D. McCulloch, D. McKenzie, A. Basu, I. Suarez-Martinez, N. Marks, R. Boehler, B. Haberl, and J. Bradby, "In situ analysis of the structural transformation of glassy carbon under compression at room temperature," *Physical Review B*, vol. 99, no. 2, p. 024 114, 2019.

[20] S. Bukalov, L. Leites, A. Sorokin, and A. Kotosonov, "Structural changes in industrial glassy carbon as a function of heat treatment temperature according to Raman spectroscopy and X-ray diffraction data," *Nanosystems: Physics, Chemistry, Mathematics*, vol. 5, no. 1, pp. 186–191, 2014.

[21] R. E. Franklin, "The interpretation of diffuse X-ray diagrams of carbon," *Acta crystallographica*, vol. 3, no. 2, pp. 107–121, 1950.

[22] K. Jurkiewicz, S. Duber, and A. Burian, "Paracrystalline structure of glass-like carbons," *International Journal of Applied Glass Science*, vol. 7, no. 3, pp. 355–363, 2016.

[23] Y. Yang, S. Zhao, J. Gong, X. Jiang, and C. Sun, "Effect of heat treatment on the microstructure and residual stresses in (Ti, Al) N films," *Journal of Materials Science & Technology*, vol. 27, no. 5, pp. 385–392, 2011.

[24] J. Luthin and C. Linsmeier, "Influence of oxygen on the carbide formation on tungsten," *Journal of nuclear materials*, vol. 290, pp. 121–125, 2001.

[25] B. D. Cullity and S. R. Stock, *Elements of x-ray diffraction*. Addison-Wesley Publishing company Inc, Massachusetts, 1956.

[26] B. Mallick, "X-ray diffraction analysis of polymeric solid using bragg-brentano geometry," *Int. J. Mater. Chem. Phys*, vol. 1, pp. 265–270, 2015.

[27] T. Ida and K. Kimura, "Flat-specimen effect as a convolution in powder diffractometry with bragg–brentano geometry," *Journal of applied crystallography*, vol. 32, no. 4, pp. 634–640, 1999.

[28] P. J. Harris, "Structure of non-graphitising carbons," *International Materials Reviews*, vol. 42, no. 5, pp. 206–218, 1997.

[29] Y. J. Lee, "The second order Raman spectroscopy in carbon crystallinity," *Journal of nuclear materials*, vol. 325, no. 2-3, pp. 174–179, 2004.

[30] E. G. Njoroge, L. Sebitla, C. Theron, M. Mlambo, T. T. Hlatshwayo, O. S. Odutemowo, V. Skuratov, E Wendler, and J. B. Malherbe, "Structural modification of indium implanted glassy carbon by thermal annealing and SHI irradiation," *Vacuum*, vol. 144, pp. 63–71, 2017.

[31] M. C. Hugon, C. Arena, B. Agius, M. Froment, F. Varniere, and C. Vignaud, "Structure and properties of rf magnetron sputtered W films," *Microscopy Microanalysis Microstructures*, vol. 1, no. 3, pp. 175–187, 1990.

[32] R. Pretorius, C. C. Theron, A. Vantomme, and J. W. Mayer, "Compound phase formation in thin film structures," *Critical reviews in solid state and materials sciences*, vol. 24, no. 1, pp. 1–62, 1999.

[33] C. Canali, G. Majni, G. Ottaviani, and G. Celotti, "Phase diagrams and metal-rich silicide formation," *Journal of Applied Physics*, vol. 50, no. 1, pp. 255–258, 1979.

[34] C. Theron, O. Ndwandwe, J. Lombaard, and R. Pretorius, "First phase formation at interfaces: Comparison between walser-bené and effective heat of formation model," *Materials chemistry and physics*, vol. 46, no. 2-3, pp. 238–247, 1996.

[35] D. McCulloch, S. Prawer, and A Hoffman, "Structural investigation of xenon-ion-beam-irradiated glassy carbon," *Physical Review B*, vol. 50, no. 9, pp. 5905–5910, 1994.

[36] A. C. Ferrari and J. Robertson, "Interpretation of Raman spectra of disordered and amorphous carbon," *Physical review B*, vol. 61, no. 20, pp. 14 095–14 107, 2000.

[37] B. Elman, M. Dresselhaus, G. Dresselhaus, E. Maby, and H. Mazurek, "Raman scattering from ion-implanted graphite," *Physical Review B*, vol. 24, no. 2, pp. 10–27, 1981.

[38] R. Al-Jishi and G. Dresselhaus, "Lattice-dynamical model for graphite," *Physical Review B*, vol. 26, no. 8, pp. 4514–4520, 1982.

[39] N. Everall, J. Lumsdon, and D. Christopher, "The effect of laser-induced heating upon the vibrational Raman spectra of graphites and carbon fibres," *Carbon*, vol. 29, no. 2, pp. 133–137, 1991.

[40] D. Fischbach and M. Couzi, "Temperature dependence of Raman scattering by disordered carbon materials," *Carbon*, vol. 24, no. 3, pp. 365–369, 1986.

[41] T. Gruber, T. W. Zerda, and M. Gerspacher, "Raman studies of heat-treated carbon blacks," *Carbon*, vol. 32, no. 7, pp. 1377–1382, 1994.

[42] L. Soukup, I. Gregora, L. Jastrabik, and A. Koňáková, "Raman spectra and electrical conductivity of glassy carbon," *Materials Science and Engineering: B*, vol. 11, no. 1-4, pp. 355–357, 1992.

[43] F. Tuinstra and J. L. Koenig, "Raman spectrum of graphite," *The Journal of Chemical Physics*, vol. 53, no. 3, pp. 1126–1130, 1970.

[44] J. Burgdörfer, C. Lemell, K. Schiessl, B. Solleder, C. Reinhold, K. TŐKÉSI, and L. Wirtz, "Collisions of slow highly charged ions with surfaces," in *Photonic, Electronic and Atomic Collisions*, World Scientific, 2006, pp. 16–45.

[45] D. Schneider and M. Briere, "Investigations of the interactions of highest charge state ions with surfaces," *Physica Scripta*, vol. 53, no. 2, pp. 228–238, 1996.

[46] H. P. Klug and L. E. Alexander, *X-ray diffraction procedures: For polycrystalline and amorphous materials*. John wiley & sons, New York, 1974.

[47] N. S. Gingrich, "The diffraction of x-rays by liquid elements," *Reviews of Modern Physics*, vol. 15, no. 1, pp. 90–110, 1943.

[48] E. Prince, *International Tables for Crystallography, Volume C. 3rd*, 2004.

[49] A. Sarkar, K. Dasgupta, P. Barat, P. Mukherjee, and D. Sathiyamoorthy, "Studies on neon irradiated amorphous carbon using X-ray diffraction technique," *International Journal of Modern Physics B*, vol. 22, no. 07, pp. 865–875, 2008.

[50] B. Warren, "X-ray diffraction in random layer lattices," *Physical Review*, vol. 59, no. 9, p. 693, 1941.

CHAPTER

EIGHT

SUMMARY AND FUTURE WORK

8.1 Summary

The focus of this study is on the solid state interaction between the W films and glassy carbon substrates. The stability of the diffusion couples under the heat treatment, the interface interaction and carbide phases formed have been studied. To gain more insight on the interface mixing regions due to annealing, quantitative measurements of the solid state reactions between deposited W films and glassy carbon substrates were carried out. In addition, the structural changes of glassy carbon under the influence heat treatment and HCI irradiation were monitored by Raman technique. XRD analysis was performed on glassy carbon and its microstructure in terms of amorphous content was studied. Some conclusions were drawn up and summarised based on results obtained in this study.

The thermal stability of the W films-glassy carbon interface was confirmed

up to annealing temperatures of 800 °C, where atomic intermix of the two substances set in, and increase with annealing duration. There was no carbide phase formation at this temperature regime.

However, carbide phase formation was observed in the samples annealed at 900 °C. This first phase was confirmed by XRD technique to be W_2C. The reaction interface was observed to widen with annealing duration. The RBS spectra showed and the RUMP simulation results showed that carbon diffused into the W films. Longer annealing duration at this temperature showed the presence of carbon substantially mixed with the W films and the glassy carbon appeared at its surface channel position, indicating that carbon diffused into the W films. At annealing temperature of 1000 °C, the features observed in the samples annealed at 900 °C were also evident in those of 1000 °C samples, with well pronounced effects. The W films were completely consumed at this temperature to form WC.

The kinetic study of the annealed diffusion couples at temperatures of 800 - 1000 °C, revealed that the intermixed layers increased with annealing temperature and duration. The growth kinetic of the layers is found to be diffusion controlled. The activation energy of 2.23 eV was obtained for diffusion of glassy carbon in W films. XRD results showed that the as-deposited W films was polycrystalline film characterized with small crystallite size, which increased with annealing temperatures. Carbide phases formed upon annealing were positively identified. The surface morphology of the deposited W films

was characterized SEM. The SEM micro-graphs showed that the as-deposited films were smooth and homogeneous. SEM images of the annealed sample showed complete absence of delamination even at 1000 °C. This showed that the W films were firmly adhered to the glassy carbon substrate, indicating that appropriate sputtering parameters were used.

The structural changes of glassy carbon under the influence of heat treatment and HCI irradiation were also studied with Raman technique. Results showed that the graphitic domains in the glassy carbon experienced a growth in size upon annealing. On the other hand, it suffered disorder in its microstructure which was assumed to be mild. The disorder effect introduced by the HCI bombardment was concentrated at the near surface region. The AFM analysis showed that induced surface roughness increased with both fluence and kinetic energy of the HCI.

The XRD study of microstructure glassy carbon by method intensity calculation showed that it is composed of both amorphous and crystalline carbon material. The percentage amorphous and crystalline contents are 25% and 75%, respectively.

8.1.1 Implications of the key findings

(i) The C-W interaction began at 800 °C. This indicates that these two materials are thermally stable in the context of temperature regimes of the dry casks. Hence, the probability that the C-W system will degrade as a result of nuclear waste decay heat should be low.

(ii) The tungsten carbides formed contribute to the properties of the C-W system. Although, tungsten carbide is hard and tough against corrosion with good radiation shield, but hard materials are known to be brittle. This might bring about cracks development without warning. Except with appropriate alloying, the role of tungsten carbide is questionable in a system where crack is a serious concern.

(iii) The stability exhibited by the glassy carbon under the influence of HCI bombardment shows that it has a property required of a radiation-tolerant material.

(iv) The 75% crystalline content of the glassy carbon is an indication that it has a promising applications as structural material in dry casks and many other aggressive environments in the nuclear technology.

8.1.2 Future work

In the future, with the hope of access to modern state-of-the-art facilities, the scope of this study will be expanded to cover the following areas:

- High resolution transmission electron microscopy (TEM) will be used to monitor the growth of the reaction interface and characterize the micro-structure evolution.

- Electron-energy-loss spectroscopy (EELS) will be applied to study the amorphous fraction of glassy carbon.

- The effects of neutron irradiation on glassy carbon will be investigated

8.2 Research output

8.2.1 Publications

- **Innocent A.J.**, T.T. Hlatshwayo, E.G. Njoroge and J.B. Malherbe. Interface interaction of tungsten film deposited on glassy carbon under vacuum annealing. Vacuum 148 (2018) 113-116.

- **Innocent A.J.**, T.T. Hlatshwayo, E.G. Njoroge, T. P. Ntsoane, M.Madhuku, E.O. Ejeh, M. Mlambo, M.Y.A. Ismail, C.C. Theron and J.B.Malherbe. Evaluation of diffusion parameters and phase formation between tungsten films and glassy carbon. Vacuum 175 (2020) 1-8.

- Malherbe J.B., O.S. Odutemowo, D. Langa, **A.J. Innocent**, E.G. Njoroge, T.T. Hlatshwayo. Microstructure of virgin and ion bombarded glassy carbon. Vacuum (under-review).

8.2.2 Conferences

- The 23rd International Conference on Ion-Surface Interactions (ISI-2017), Moscow, Russia. 21-25 August, 2017

- The 62nd annual conference of the South African Institute of Physics. Stellenbosch University, South Africa. 3 -7 July, 2017

8.2.3 Award

- Best poster presented at the 23rd International Conference on Ion-Surface Interactions (ISI-2017), Moscow, Russia. 21-25 August, 2017